Centrifuge modelling of the behaviour of buried pipelines subjected to submarine landslides

Zhang, W.

DOI
10.4233/uuid:2411b615-c28b-459a-8ddf-1c13c670a0f7

Publication date
2020

Document Version
Final published version

Citation (APA)
Zhang, W. (2020). *Centrifuge modelling of the behaviour of buried pipelines subjected to submarine landslides*. [Dissertation (TU Delft), Delft University of Technology]. https://doi.org/10.4233/uuid:2411b615-c28b-459a-8ddf-1c13c670a0f7

Centrifuge modelling of the behaviour of buried pipelines subjected to submarine landslides

Centrifuge modelling of the behaviour of buried pipelines subjected to submarine landslides

Proefschrift

ter verkrijging van de graad van doctor
aan de Technische Universiteit Delft,
op gezag van de Rector Magnificus Prof. dr. ir. T.H.J.J. van der Hagen,
voorzitter van het College voor Promoties,
in het openbaar te verdedigen op donderdag 8 oktober 2020 om 10:00 uur

door

Weiyuan ZHANG

Master of Science in Geotechnical Engineering,
Harbin Institute of Technology, China
geboren te Jilin, China.

Dit proefschrift is goedgekeurd door de promotoren.

Samenstelling promotiecommissie bestaat uit:

Rector Magnificus	voorzitter
Prof. dr. ir. C. Jommi	Technische Universiteit Delft, promotor
Dr. A. Askarinejad	Technische Universiteit Delft, copromotor

Onafhankelijke leden:

Prof. dr. M.A. Hicks	Technische Universiteit Delft
Prof. dr. K.G. Gavin	Technische Universiteit Delft
Dr. L. Thorel	Université Gustave Eiffel, France
Dr. S.A. Stanier	University of Cambridge, England
Dr. ir. A. Tsouvalas	Technische Universiteit Delft

Research described in this thesis was supported by the China Scholarship Council (CSC), and the Geo-Engineering section, Department of Civil Engineering and Geoscience, TU Delft.

Keywords: Landslides, Static liquefaction, Soil-pipeline interaction, Centrifuge modelling, Image analysis, Scaling laws

Printed by: Ipskamp Drukker

Front & Back: Designed by Yanchun Wei, www.springwei.eu.com

Email: w.zhang-3@tudelft.nl; zhangweiyuanhitsz@gmail.com

ISBN 978-94-6421-049-1

An electronic version of this dissertation is available at
http://repository.tudelft.nl/.

Underground pipelines are the arteries of our nation, the lifeblood of our society. They work silently and continuously, 24 hour a day, 365 days a year, to deliver the energy to enable our country to thrive.

Opening Address by I. Itzkovitch
to Managing Pipeline Integrity-An Issues Workshop
on Pipeline Life cycle in 1994

Contents

Summary

The assessment of the potentially destructive impacts of subaqueous landslides on offshore pipelines is required when the pipeline route passes through zones with a risk of mass movements. Therefore, quantifying and evaluating the ultimate load/pressure acting on the pipeline is one of the key factors in geotechnical safety design of the pipeline. One of the triggers of subaqueous soil mass movements is the monotonic loads, which induce the trigger relative displacement between a soil layer and a pipe under both drained and (partially) undrained conditions. Two approaches based on geotechnical and fluid dynamics perspectives have been proposed for estimating the ultimate load/pressure for different stages of a submarine landslide. Traditionally, the former method focuses on the analysis of pipelines installed under flat seabed experiencing relative movements to the surrounding soil, whereas, the latter method focuses on the behaviour of pipelines laid on the surface of the seabed and subjected to debris flows. However, offshore pipelines are often buried under the seabed, which is not always flat and has a modest inclination in some cases. This engineering condition normally differs from that of the simplifying assumptions and boundary conditions (such as seabed inclination, and soil strength) commonly imposed to the geotechnical and fluid dynamics approaches. Accordingly, a better understanding of the soil-pipeline interaction when the pipelines are buried in subaqueous slopes is essential for evaluating the ultimate load/pressure that would be caused by the slope failures.

This thesis presents a research effort on investigating the soil-pipeline interaction during subaqueous slope failures using advanced physical modelling. In this research, the experiments can be divided into two main groups according to the soil drainage conditions. The first group of tests were carried out in the drained condition by using dry sand as the soil material for the slopes. The pipe was buried at 5 different locations inside the slopes to study the pipe burial position and pipe embedment ratio effects on the ultimate pressure during slope instability. Particle image velocimetry analysis was conducted to study the pipe movement and slope failure mechanisms. The results of these tests reveal that the slope angle and the pipe distance to slope crest play significant roles on the ultimate loads acting on the pipe.

The second group of tests were carried out in the (partially) undrained condition which consists of three steps, the first of which was designed with the main aim of simulating monotonic-load-induced liquefaction in a centrifuge. An actuator was designed which comprised of a tilting system, a fluidization system and high speed, high resolution image capturing system. An X-ray CT scan was also performed to monitor the uniformity of the samples. The outcome of this step of the research was the development of a novel test set-up for controlled and repeatable triggering of landslides in submarine slopes using geotechnical centrifuge.

The second step of this research examined the scaling laws for pore fluid viscosity to simulate the onset of monotonic-load-induced liquefaction in the centrifuge. A hypothesis of a static liquefaction triggering mechanism was proposed, which is followed by the determination of the scaling factor of pore fluid viscosity based on the grain scale analysis. A "modelling-of-models" study was carried out on saturated sandy samples using both *N*-fluid and $\sqrt{N}$-fluid as the pore fluids. (*N*-fluid represents a fluid has a viscosity of *N*-times higher than water; $\sqrt{N}$-fluid represents a fluid has a viscosity of $\sqrt{N}$-times higher than water.) Based on the experimental results in terms of slope failure angle and excess pore pressure ratio, it was confirmed that the scaling factor of pore fluid viscosity for simulating the onset of static liquefaction (i.e. for slope stability analysis) is different from that for simulating slope post-liquefaction behaviour. The former case requires a fluid $\sqrt{N}$-times more viscous than water, while the latter case requires fluid *N*-times more viscous than water.

In the last step of this group of tests, the pressures acting on the buried pipes during slope liquefaction were measured and the influence of including pipe embedment ratio, pipeline structural stiffness, slope angle and shear strain rate on the measurements were investigated. The Particle Image Velocimetry technique was applied, which enables the analysis and visualization of the development of static liquefaction. The ultimate pressures exerted on the pipes were compared with the estimations from both the geotechnical and fluid dynamics approaches. The results indicated that, unlike the geotechnical approach, the ultimate pressures were not affected by the different pipe embedment ratios; however, there was a power law relationship between the ultimate pressures and the soil shear strain rates. Furthermore, it was observed that a higher value in either the pipeline structural stiffness or slope angle would result in a higher soil shear strain rate and a larger ultimate pressure on the pipe.

Samenvatting

Wanneer een offshore pijpleiding zich in een zone bevindt waarin onderzeese aardverschuivingen kunnen optreden, dienen de mogelijke gevolgen van een dergelijke aardverschuiving in kaart te worden gebracht. Om bij het ontwerp het vereiste veiligheidsniveau te bereiken dient de (geotechnisch) ingenieur de grootte en de aard van de belasting, die op de pijpleiding aangrijpt, te kennen. Een onderzeese aardverschuiving kan onder andere door een monotone belasting worden getriggerd en als gevolg hiervan kunnen er relatieve verplaatsingen tussen de grond en de pijpleiding optreden. De grond kan zich hierbij zowel gedraineerd of (gedeeltelijk) ongedraineerd gedragen, afhankelijk van de snelheid van het proces. Twee verschillende benaderingen, gebaseerd op respectievelijk grond- en vloeistofdynamica, zijn voorgesteld om de belasting tijdens de verschillende stadia van een onderzeese aardverschuiving te schatten. Traditioneel richt de eerstgenoemde benadering zich op pijpleidingen die zijn aangelegd onder een vlakke zeebodem en relatieve bewegingen ondergaan ten opzichte van de omringende grond, terwijl de laatstgenoemde benadering zich richt op pijpleidingen die op de zeebodem zijn gelegd en blootstaan aan puinstromen. Offshore pijpleidingen liggen echter in werkelijkheid veelal begraven onder de zeebodem, die niet overal even vlak is en ook een bescheiden helling kan aannemen. Deze conditie verschilt daarmee van de vereenvoudigende aannamen en condities, zoals zeebodemhelling en bodemsterkte, die gewoonlijk worden opgelegd aan de twee genoemde benaderingen. Dienovereenkomstig is, wanneer pijpleidingen worden begraven in onder water gelegen hellingen, een beter begrip van de interactie tussen de grond en de pijpleiding essentieel voor het evalueren van de uiteindelijke belasting die worden veroorzaakt door de afschuivingen.

Dit proefschrift behelst onderzoek naar de interactie tussen de pijpleiding en de bodem tijdens een afschuiving van een onderwatertalud met behulp van geavanceerde fysieke modellering. In het licht van de drainagecondities kunnen de experimenten die zijn uitgevoerd in dit onderzoek worden onderverdeeld in twee hoofdgroepen. De eerste hoofdgroep behelst experimenten waarin volledig gedraineerd gedrag is gewaarborgd door droog zand toe te passen als materiaal voor de taluds. De modelbuis is op vijf verschillende locaties onder het talud gepositioneerd om de invloed van de aanlegpositie en van de inbedding op de uiteindelijke belasting tijdens een taludinstabiliteit te bestuderen. De gemaakte opnamen zijn door middel van de Particle image velocimetry-methode geanalyseerd om de beweging van de pijpleiding en het faalmechanisme van het talud te bepalen. De tetsresultaten laten zien dat de helling van het talud en de afstand tussen de pijpleiding en de kruin een belangrijke rol spelen als het gaat om de belasting op de pijpleiding.

De tweede hoofdgroep bevat experimenten waarin (gedeeltelijk) ongedraineerd gedrag is opgelegd. Hierin kunnen drie stappen worden onderscheiden. De eer-

ste stap was het mogelijk maken van het simuleren van een statische liquefactie in een geotechnische centrifuge. Voor dit doeleinde is een opstelling ontworpen en ontwikkeld die bestaat uit een kantelsysteem, een fluïdisatie-systeem en een camerasysteem, dat hoog frequent beelden met hoge resolutie kan vastleggen. Er is gebruikt gemaakt van de röntgen-CT-scan-techniek om de uniformiteit van het grondmodel te evalueren. Het resultaat van deze eerste stap was de ontwikkeling van een nieuwe testopstelling voor een geotechnische centrifuge waarmee gecontroleerd en herhaalbaar afschuivingen in een onderwatertalud kunnen worden geactiveerd.

Bij de tweede stap binnen dit onderzoek zijn de schaalwetten voor de viscositeit van de porievloeistof onderzocht om de aanvang van een statische liquefactie te simuleren tijdens een experiment in een centrifuge. Hiervoor is eerst een hypothese opgesteld over het mechanisme dat een statische liquefactie activeert. Dit werd gevolgd door het bepalen van de schaalfactor op basis van een analyse van de korrelgrootte. Het ''modelleren-van-modellen-principe'' is toegepast op verzadigde zandmonsters door twee typen porievloeistof toe te passen: een vloeistof met een viscositeit N keer groter dan water en een vloeistof met een viscositeit $\sqrt{N}$ keer groter dan water. In termen van hellingshoek en relatieve wateroverspanning bevestigen de testresultaten dat de vereiste schaalfactor voor het simuleren van de aanvang van een statische liquefactie (d.w.z. voor de analyse van de taludstabiliteit) verschilt van die voor het simuleren van het taludgedrag na verweking. Het eerste fenomeen vraagt om een vloeistof met een viscositeit $\sqrt{N}$ keer groter dan water, terwijl het tweede fenomeen om een vloeistof vraagt met een viscositeit N keer groter dan water.

De laatste stap binnen de tweede hoofdgroep experimenten bestond uit het meten van de drukken op de leiding tijdens het verweken van het talud. Daarbij is de invloed van de inbeddingsdiepte en de stijfheid van de pijpleiding, van de helling van het talud en van de schuifreksnelheid op de gemeten drukken onderzocht. Om de ontwikkeling van de statische verweking te analyseren en te visualiseren is ook hier de Particle image velocimetry-methode toegepast. De gemeten drukken die werden uitgeoefend op de modelpijpleiding zijn vergeleken met de schattingen op basis van zowel de geotechnische en de vloeistofdynamica-benadering. In tegenstelling tot de geotechnische benadering suggereert, werden de gemeten drukken niet beïnvloed door de inbeddingsdiepte van de leiding. Er werd echter wel een machtsverband gevonden tussen de uiteindelijke druk op de leiding en de schuifreksnelheid in het grondmodel. Verder werd waargenomen dat een hogere waarde van de stijfheid van de pijpleiding en/of van de hellingshoek van het talud resulteert in een hogere (relatieve) schuifreksnelheid en daarmee in een hogere druk die wordt uitgeoefend op de leiding.

1

Introduction

The fear of the Lord is the beginning of wisdom.

Psalm 111:10, New International Version.

1

1.1. Background

During the period from 1970s to 1990s, around 90 000 km of offshore pipelines have been installed. It is reported that 6436 km of offshore pipeline are planned to be built in the years from 2016 to 2020 . Due to the long transportation distance, offshore pipelines may span over a variety of geotechnical/geological environments and pass across areas with a high potential for geo-hazards. The failure of submarine slopes is one of the frequently reported geo-hazards that may have catastrophic effects on offshore infrastructure (Randolph and Gourvenec, 2011).

Reifel (1979) reported seven significant buried/unburied pipeline damages which were caused by mudslides during the period from 1961 to 1977. Woodson (1991) reported that 12% of pipeline failures in the Gulf of Mexico (U.S. outer continental shelf region) were caused by natural forces, such as storms and mudslides. The transported crude oil flows into the ocean as a consequence of the pipelines' leakage contributed to marine landslides. This will cause pollution, death of sea creatures and shortage in energy supply, and require huge reparation fees (Randolph and Gourvenec, 2011). During the private communication with some experts from the petroleum industry, the author has learned that many cases of offshore pipeline failure damaged by geo-hazards have not been published to the public to avoid the potential negative effects on global petroleum price and hence also on the global economy.

Compared to onshore landslides, offshore landslides feature long run-out distance, huge released soil mass and mild slope failure angle, as seawater significantly influences the sliding process. It is reported that the run-out distance of subaqueous landslides varies from less than one kilometre to tens of kilometres with released material ranging from less than 10 km^3 to more than 100 km^3 (Gue, 2012). Submarine slope failure angles are generally smaller than $25°$, with most failure angles ranging from less than $1°$ to $10°$. The characteristics of subaqueous landslides are influenced by many factors such as geophysical and geological conditions, triggering mechanism, and environment conditions.

The development of a submarine landslide can be generally divided into five stages as explained by Boylan et al. (2009), which are schematically illustrated in Figure 1.1. At the different stages, the soil velocity and properties vary significantly. The sliding material can be regarded as intact soil moving slowly and holding geotechnical properties in the initiation stage. The failed soil mass then becomes agitated and transits into debris flow, turbidity current and heavy fluid, with a high moving rate as the gravitational potential energy converts to internal kinetic energy. The strength of the sliding material is weakened accordingly during the evolution of a submarine landslide attributed to the presence of excess pore pressure (EPP). When the EPP is zero, the soil mass has a drained shear strength; when the EPP equals the soil principle effective stress, the soil mass liquefies and loses its shear strength; and when the EPP is less than the soil principle effective stress, the soil has an undrained shear strength. Clearly, the magnitude of the generated EPP plays an important role in affecting soil properties and soil-pipeline interaction mechanisms.

Sandy soil is widely distributed in the delta areas and inner continental shelf.

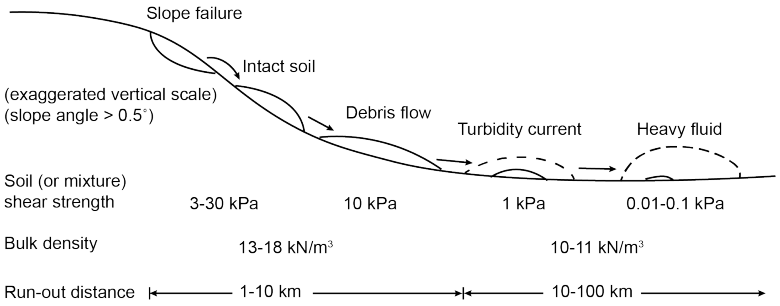

Figure 1.1: Schematic illustration of the evolution of a marine landslide (Modified after Boukpeti et al., 2012, Boylan et al., 2009, Fan et al., 2018)

This type of soil is normally characterised as fine, loose and saturated sand which is prone to liquefaction under either cyclic or monotonic loading conditions. Monotonic loads due to rapid deposition, toe erosion, scour, slope steepening and human construction activities have been reported as one of the major factors affecting seabed slope stability (Kvalstad et al., 2001, Ye et al., 2017). Slope angles increase with the process of sedimentation deposition, erosion or tectonic motion, and liquefaction may happen as a result of the changing of soil stress conditions and the accumulation of pore pressure during this process.

In engineering practice, some offshore pipelines are designed to be fully embedded into seabed with a certain depth for protection from hydrodynamic loads due to strong currents/waves above seabed, or impact loads from ship anchors or icebergs. In the geotechnical design of a buried pipeline, the prediction of pipeline external loads is indispensable. A buried pipeline subjected to a marine landslide will deform, as schematically illustrated in Figure 1.2, due to the combination of various loads such as drag force along the soil moving direction, uplift and self-weight in the out-of-plane direction, as well as soil passive and frictional resistance outside of the soil failure zone. Zakeri et al. (2008) proposed that the ultimate external load in the direction perpendicular to the pipeline axis (horizontal direction) is larger than the uplift force and soil resistance along pipeline axis. Thus, it is important to evaluate the ultimate horizontal pressure acting on the pipeline during a marine landslide.

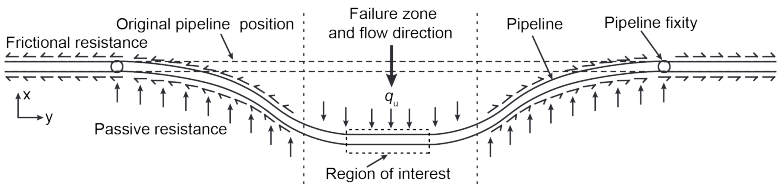

Figure 1.2: Schematic illustration of pipeline deformation due to seabed movement (top view)

1.2. Motivation and objectives

The current study is motivated by the desire of providing a method to evaluate the ultimate horizontal forces impacting on embedded pipelines with the consideration of seabed movement effects in order to reduce the chance of pipeline damage that could be caused by subaqueous monotonic-load-induced landslides. The attempts to investigate the ultimate horizontal pressure acting on the pipeline generally fall into two main categories: geotechnical approach and fluid dynamics approach, as summarised by Zakeri et al. (2008). Literature study of both methods is presented in Chapter 2 and Chapter 6. Herein, in short, the geotechnical approach is traditionally developed based on the condition that the pipe is buried under flat ground, the soil resistance is caused by the active movement of the pipe, and the pipe moving velocity could be controlled in such a way that the soil can be mobilised under either drained or undrained conditions. While the fluid dynamics approach considers the condition that a non-buried pipeline is being hit by a debris flow with the assumption that the sliding material is a dense fluid composed of a mixture of soil with water.

A reasonable assessment of the ultimate pressure/load acting on an embedded pipeline as a result of seabed soil movement is crucial for offshore pipeline safety design. However, both geotechnical and fluid dynamics approaches are not able to be directly applied to the case when a pipeline is buried in an unstable slope. Thus, this study aims at investigating soil-pipeline interaction mechanisms with the pipe embedded in an unstable subaqueous sloping ground under monotonic loads.

1.3. Methodology, novelty and outline of the thesis

Physical modelling techniques have been widely adopted to investigate complex soil-structure interaction engineering problems, especially for subaqueous landslide-related issues (Boylan et al., 2010, Phillips and Byrne, 1995, Rui and Yin, 2019). Considering the scale and subaqueous environment, field and large-scale tests are impractical. Physical modelling has the advantage of studying prototype soil-structure behaviour in small-scale models. As soil behaviour is highly dependent on stress conditions, the centrifuge modelling technique has been developed to provide prototype stress conditions in small-scale models by performing tests under enhanced centrifugal acceleration conditions.

Based on the literature study presented in Chapter 2 and Chapter 6, several centrifuge tests have been conducted to investigate soil-pipeline interaction mechanisms based on geotechnical method (Hodder and Cassidy, 2010, Sahdi et al., 2014, Zhang et al., 2002) and fluid dynamics method (Zakeri et al., 2012). However, the research related to monotonic-load-induced seabed slope instabilities and the behaviour of buried pipeline in inclined seabed is limited. Hence, in the current research, centrifuge modelling is adopted as the main methodology to simulate monotonic-load-induced subaqueous landslides with the purpose of evaluating the ultimate pressure impacting on a buried pipeline.

In this research, the soil-pipeline interaction mechanism has been studied according to the two extreme drainage conditions, i.e. fully drained condition and

undrained conditions. For loose sandy seabed, soil drainage is related to soil permeability, loading rate and relative pipe-soil moving rate. In prototype, sandy soil deformation under monotonic loads can happen slowly under drained conditions or rapidly under undrained conditions. Furthermore, the geometric factors, such as pipe embedment ratio, slope angle and pipeline burial location according to slope crest and slope toe, and soil shear strain rate, can influence the ultimate pressure acting on the pipe as well.

Accordingly, centrifuge models with the variation of the above-mentioned factors have been conducted to explore their effects on the ultimate pressure exerted on the pipe. This dissertation is composed of four main chapters (i.e. Chapters 3 to 6). The outline of these main chapters is presented in Figure 1.3. Each of these chapters are organised with the purpose of being self-consistent research work. Among them, Chapters 3, 4 and 5 are journal papers which have already been published, and Chapter 6 has been received positive feedback from the reviewers of *Landslides* at the moment of submitting this dissertation. It should be noted that two types of monotonic load triggering mechanisms (i.e. slope crest loads and slope steepening) were assigned to the tests with different soil drainage conditions as shown in Figure 1.3. The structure, purpose and methodology of these main chapters and the selection of triggering mechanisms are explained in the following sub-sections.

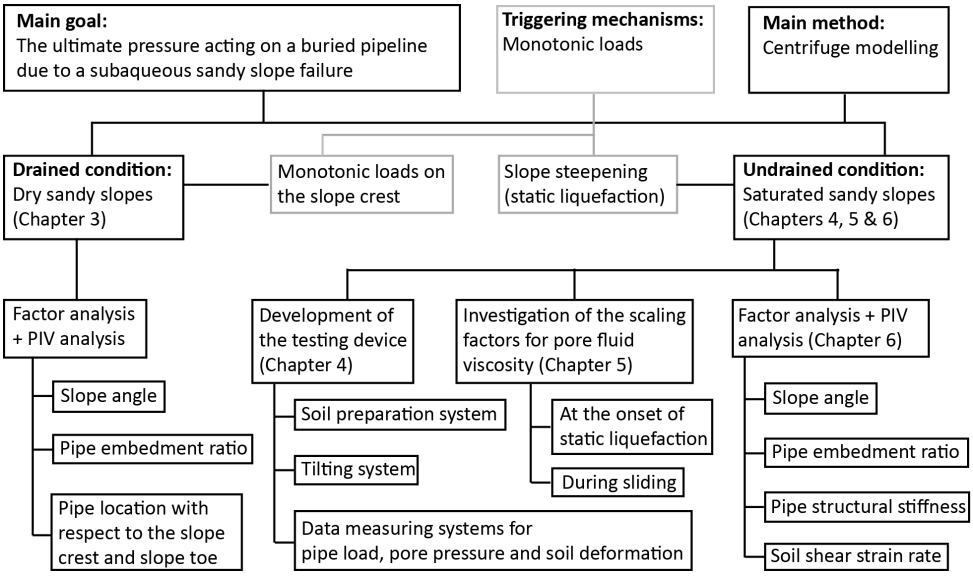

Figure 1.3: Schematic illustration of the main structure of this dissertation

Furthermore, this dissertation consists of the three other chapters, which are explained below:

- Chapter 1 introduces the background, motivation and objectives of this study as well as the main adopted methodology.

- Chapter 2 reports the literature review of previous research on soil-pipeline interaction and on centrifuge modelling of marine landslides. Two traditional analytical models for predicting the ultimate pressure are introduced first. Secondly, the experimental techniques that have been developed in the previous research are briefly reviewed. Lastly, the limitations of these two analytical methods are discussed.

- In Chapter 7, a summary of the thesis, some main research conclusions and recommendations for future research are provided.

1.3.1. Simulation under drained condition (Chapter 3)

Many researchers have conducted tests under dry condition to simulate soil behaviour under fully drained condition (Cox et al., 2014, Yamada et al., 2010). In the case when excess pore pressure can dissipate freely, the behaviour of dry sandy samples is similar to that of saturated sandy samples provided that all other conditions are the same. However, the buoyancy effect on soil stress levels should be accounted for when air is used as the pore fluid.

Chapter 3 presents some centrifuge slope failure tests triggered by monotonic loads on slope crest by using a displacement-controlled load actuator. This triggering mechanism is analogous to that of construction loads on seabed slopes or deposition of sedimentation. For exploring pipe burial position and pipe embedment ratio effects on the ultimate horizontal pressure, the pipe was buried at five different locations in the slopes. Strain gauges were installed on the pipe to measure the external forces on the pipe induced by the surrounding soil movements. To investigate soil-pipeline interaction mechanism, slope failure mechanisms were visualised by using the Particle Image Velocimetry (PIV) technique. Moreover, a new prediction method is introduced as a modification of the traditional geotechnical method for estimating the soil resistance acting on a pipe buried under flat ground. The new method is able to consider the effects of slope angle and pipe-to-slope crest distance on the ultimate pressure.

1.3.2. Simulation of static liquefaction (undrained condition) –a) development of the test set-up (Chapter 4)

As the first step to investigate the ultimate pressure on a buried pipeline due to the static liquefaction of a subaqueous slope, a novel testing system was designed to simulate subaqueous slope static liquefaction. The sample preparation system, the triggering mechanism of static liquefaction, the pipeline burial and external pressure measuring system and the image capturing system were integrated into the test set-up design. Chapter 4 presents the details of this newly developed set-up.

The fluidization method was adopted to prepare loose and saturated sandy samples with the purpose of resembling seabed soil structures and conditions. The relative density, uniformity and saturation of a sandy sample play important roles in simulating seabed static liquefaction. Therefore, the examination of these properties of the sample are introduced in Chapter 4.

Slope steepening (i.e. gradual increase of shear stress level) was selected as the

triggering mechanism of static liquefaction, hence, a tilting mechanism was added into the test set-up. Gradual increase of local seabed inclination can be induced by the deposition of sedimentation or sand erosion and scour around hydraulic structures and offshore foundations. During this process, shear stresses in the soil body increase monotonically which may eventually lead to static liquefaction. Such processes have been identified as a potential threat to the safety of the Eastern Scheldt storm surge barrier, in which a scouring hole has been developing near the seabed protection layer of the barrier (De Jager, 2018, Silvis and Groot, 1995). Furthermore, the slope steepening rate effects and Coriolis effects on sample stability are discussed in Chapter 4.

1.3.3. Simulation of static liquefaction –b) investigation of scaling laws for pore fluid viscosity (Chapter 5)

As the second step to investigate the ultimate pressure on a buried pipeline due to the static liquefaction of subaqueous slope, the scaling factor for pore fluid viscosity was investigated to simulate subaqueous slope static liquefaction by using the test set-up developed in Chapter 4. The onset of static liquefaction in loose sand is related to the change of the soil drainage regime, from drained to temporarily undrained conditions, which is directly linked to the pore fluid viscosity. In order to simulate prototype behaviour properly in a 1/*N*-times-scaled model at a centrifugal acceleration field of *Ng*, an understanding of the scaling effects of the testing materials is necessary. For example, in an *Ng* test, time for dynamic processes has a scaling factor (prototype/model) of 1/*N*, whereas time for pore fluid pressure dissipation has a scaling factor of $1/N^2$, hence a fluid with a viscosity *N*-times higher than that of water is required to study dynamic processes.

For a monotonic-load-induced slope liquefaction, the failure process can be divided into two processes, i) static phase: the onset of static liquefaction, before which the stress condition changes monotonically; ii) dynamic phase: once a seabed liquefaction develops, i.e. the soil-fluid behaviour is dynamic. The scaling factor for pore fluid viscosity has been well studied for the dynamic phase, however, for the static phase, relevant studies are limited.

Hence, in Chapter 5, firstly a postulation about static liquefaction trigger mechanism based on the grain scale analysis is presented; then results of centrifuge tests conducted under three different centrifugal accelerations with two types of fluid viscosity are discussed. The first type of fluid has a viscosity of $\sqrt{N}$ times that of water, which is determined from the grain scale analysis; the second type of fluid has a viscosity of *N* times that of water, which is traditionally used for the simulation of fluid dynamic behaviour. Slope failure angles which indicate the onset of static liquefaction and excess pore pressure ratio at various locations are compared to examine and verify the scaling factors of pore fluid viscosity in simulating the onset and post-liquefaction behaviour of monotonic-load-induced liquefaction of subaqueous landslides.

1

1.3.4. Simulation of static liquefaction –c) behaviour of buried pipelines in statically-liquefied slopes (Chapter 6)

The last step to investigate the ultimate pressure on a buried pipeline due to static liquefaction of subaqueous slope is to introduce the pipeline burial and external pressure measuring system in the test set-up explained in Chapter 4. In Chapter 6, soil and buried pipe behaviour during the initiation of subaqueous slope static liquefaction is discussed. The ultimate pressures exerting on the pipes are compared to the two traditional approaches, namely geotechnical approach and fluid dynamics approach, as well as to the modified geotechnical approach proposed in Chapter 3. Furthermore, the influence of pipe embedment ratio, pipeline structural stiffness, slope angle and soil shear strain rate are investigated. Besides, a high speed, high resolution imaging system is introduced which enables the application of the PIV technique in analysing soil flow behaviour during slope liquefaction. The evolution of liquefaction zone is presented.

References

Boukpeti, N., White, D., Randolph, M., and Low, H. (2012). Strength of fine-grained soils at the solid–fluid transition. *Géotechnique*, 62(3):213–226.

Boylan, N., Gaudin, C., White, D., and Randolph, M. (2010). *Modelling of submarine slides in the geotechnical centrifuge*, volume 2, pages 1095–1100. CRC Press.

Boylan, N., Gaudin, C., White, D., Randolph, M., and Schneider, J. (2009). Geotechnical centrifuge modelling techniques for submarine slides. In *ASME 2009 28th International Conference on Ocean, Offshore and Arctic Engineering*, pages 65–72. American Society of Mechanical Engineers Digital Collection.

Cox, J. A., O'Loughlin, C. D., Cassidy, M., Bhattacharya, S., Gaudin, C., and Bienen, B. (2014). Centrifuge study on the cyclic performance of caissons in sand. *International Journal of Physical Modelling in Geotechnics*, 14(4):99–115.

De Jager, R. R. (2018). *Assessing Liquefaction Flow Slides: Beyond Empiricism*. Ph.d. thesis.

Fan, N., Nian, T.-k., Jiao, H.-b., and Jia, Y.-g. (2018). Interaction between submarine landslides and suspended pipelines with a streamlined contour. *Marine Georesources & Geotechnology*, 36(6):652–662.

Gue, C. S. (2012). *Submarine landslide flows simulation through centrifuge modelling*. PhD thesis, University of Cambridge.

Hodder, M. and Cassidy, M. (2010). A plasticity model for predicting the vertical and lateral behaviour of pipelines in clay soils. *Géotechnique*, 60(4):247.

Kvalstad, T., Nadim, F., and Arbitz, C. (2001). Deepwater geohazards: geotechnical concerns and solutions.

Phillips, R. and Byrne, P. (1995). Modeling flowslides caused by static loading. *Transportation Research Record*, pages 12–21.

Randolph, M. and Gourvenec, S. (2011). *Offshore geotechnical engineering*. CRC Press.

Reifel, M. D. (1979). Storm related damage to pipelines, gulf of mexico. In *Pipelines in Adverse Environments: A State of the Art*, pages 169–186. ASCE.

Rui, Y. and Yin, M. (2019). Centrifuge study on the submarine mudflows. *Marine Geodesy*, 42(1):85–102.

Sahdi, F., Gaudin, C., White, D., Boylan, N., and Randolph, M. (2014). Centrifuge modelling of active slide-pipeline loading in soft clay. *Géotechnique*, 64(1):16–27.

Silvis, F. and Groot, M. d. (1995). Flow slides in the netherlands: experience and engineering practice. *Canadian geotechnical journal*, 32(6):1086–1092.

Woodson, R. (1991). A critical review of offshore pipeline failures. *prepared for the Marine Board, National Research Council*.

Yamada, Y., Yamashita, Y., and Yamamoto, Y. (2010). Submarine landslides at subduction margins: insights from physical models. *Tectonophysics*, 484(1-4):156–167.

Ye, Y., Lai, X., Pan, G., Li, Q., Zhuang, Z., Liu, D., Chen, X., Wei, Y., Chen, J., Hu, T., Chen, X., Zhan, W., Li, Q., Tian, S., Li, D., and He, X. (2017). *Marine Geo-hazards in China*. Elsevier, Amsterdam.

Zakeri, A., Hawlader, B., and Chi, K. (2012). Drag forces caused by submarine glide block or out-runner block impact on suspended (free-span) pipelines. *Ocean Engineering*, 47:50–57.

Zakeri, A., Høeg, K., and Nadim, F. (2008). Submarine debris flow impact on pipelines—part i: Experimental investigation. *Coastal engineering*, 55(12):1209–1218.

Zhang, J., Stewart, D. P., and Randolph, M. F. (2002). Modeling of shallowly embedded offshore pipelines in calcareous sand. *Journal of geotechnical and geoenvironmental engineering*, 128(5):363–371.

2

Literature review

One's destination is never a place, but a new way of seeing things.

Henry Miller

2

This chapter aims at presenting an overview on the previous experimental research on soil-pipeline interaction. Note that a detailed literature review on each specific topic can be found in Chapters 3 to 6 according to their corresponding objectives. Hence, some of the equations reported in these chapters are also presented and discussed in this chapter for the sake of clarity.

During the development of a subaqueous slope failure, the sliding soil material may experience a transition from intact soil, holding shear strength, in the initial stages to soil-fluid mixture behaving like debris flow or heavy fluid in the later stages, as demonstrated in Figure 1.1. In practice, offshore pipelines might be located either within the initial zone or on the run-out path of a slope failure. Accordingly, geotechnical and fluid dynamics approaches have been proposed as summarised by Zakeri et al. (2008). The geotechnical approach focuses on the soil-pipe interaction when a pipe is buried and moves in a soil layer which has kept the original shear strength properties to a large extent; the fluid dynamics approach focuses on the impact of a fluid like flow on a pipe that is placed on the seabed. This chapter firstly describes these two approaches. Thereafter, details of the previous centrifuge modelling techniques applied to investigate soil-pipeline interaction are discussed. This is followed by a brief introduction to the centrifuge modelling of marine landslides.

2.1. Soil reaction due to pipe movement

2.1.1. Geotechnical approach

Various formulae in the form of Equations 2.1 and 2.2 have been developed to evaluate the ultimate soil pressure (q_{u}) acting on a buried pipe due to the horizontal motion of the pipe, as recommended in the pipeline design guidelines (e.g. Alliance, 2001, ASCE, 1984, C-CORE et al., 2009). Here, γ'_{soil} is effective soil unit weight; H_c is pipe buried depth defined as the distance between the soil surface and the pipe centre; $N_{\mathrm{q\text{-}sand}}$ is a bearing capacity factor for sand which has a relationship with pipe embedment ratio (H_{c}/D, where D is pipe diameter) and soil friction angle (Hansen, 1961, Ovesen, 1964); s_{u} is undrained shear strength; and $N_{\mathrm{q\text{-}clay}}$ is a bearing capacity factor for clay (it is either a constant or shear strain rate dependent).

$$\text{sand: } q_{\mathrm{u}} = \gamma'_{\mathrm{soil}} H_c N_{\mathrm{q\text{-}sand}} \tag{2.1}$$

$$\text{clay: } q_{\mathrm{u}} = s_{\mathrm{u}} N_{\mathrm{q\text{-}clay}} \tag{2.2}$$

Audibert and Nyman (1977) is considered as one of the pioneering experimental research works conducted to investigate the interaction between a buried pipe and soil with relative soil-pipe displacement. They developed a testing set-up (see Figure 2.1) in which the pipe was buried inside a soil layer with a flat surface and was pulled horizontally to generate relative soil-pipe movement. This testing method is referred as the ”pulling-pipe” method hereafter. The ”pulling-pipe” method has been extensively adopted by successive researchers to estimate the

soil reaction due to pipe movement (e.g. Almahakeri et al., 2013, Audibert and Nyman, 1977, Calvetti et al., 2004, Liu et al., 2015, Ono et al., 2017, Paulin, 1998, Roy and Hawlader, 2012, Sahdi et al., 2014, Tian and Cassidy, 2011, Trautmann et al., 1985, Zhang et al., 2002).

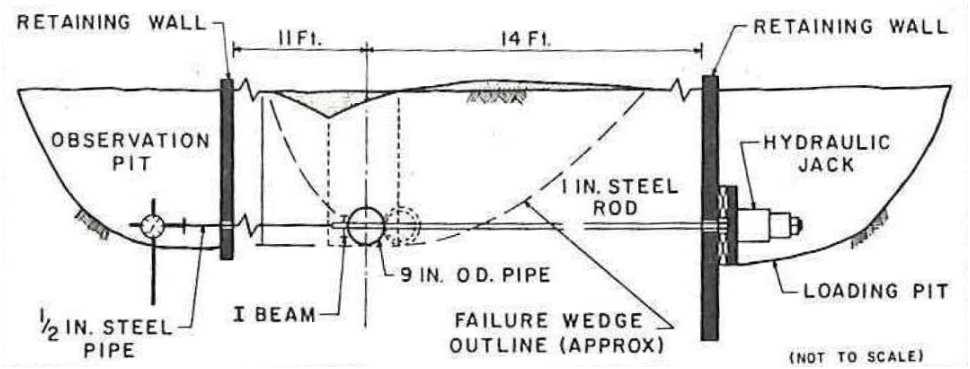

Figure 2.1: Illustration of the test set-up (side view) developed by Audibert and Nyman (1977) which is integrated with the "pulling-pipe" method

Audibert and Nyman (1977) measured the soil resistance while the pipe was dragged horizontally in loose and dense dry sand material. They concluded that $N_{\text{q-sand}}$ derived from the Hansen method (Hansen, 1961) in Figure 2.2a can be used in Equation 2.1. The experimental results (see Figure 2.3) showed that, for shallow and intermediate burial pipes with $H_c/D \leq 6$, a passive wedge and a vertical active zone were formed in front of and behind the pipe, respectively; for the deep burial pipe with $H_c/D = 24$, a confined soil flow zone was generated instead. The failure mechanism in Figure 2.3a was observed in the laboratory tests conducted by Ansari et al. (2019) as well.

Trautmann et al. (1985) tested model pipes in soil with three different densities and two types of pipe diameters. The measured loads in medium and dense sand layers agreed closely with the estimation by using the Ovesen method proposed by Ovesen (1964) (see Figure 2.2b), and were overpredicted by a factor of up to two when the Hansen method (Hansen, 1961) was used. They argued that the effect of pipe diameter on the resultant loads was insignificant in both loose and dense sand layers.

Calvetti et al. (2004) designed a test set-up with a hydraulic system to study the soil-pipeline interaction for buried pipes in a fully saturated sand layer with various excess pore pressures, as shown in Figure 2.4. The sand material had a D_{50} of 0.35 mm, a relative density of 20% and an internal friction φ' of 32° determined by triaxial compression tests. The pipe was buried with different H_c/D ranging from 1.35 to 5.24. The hydraulic gradients (i, water head difference/sand layer height) varied from 0 to 0.87.

It was found that the force required to drag the pipe in the sand layer decreased linearly with an increase of the magnitude of i. Calvetti et al. (2004) proposed

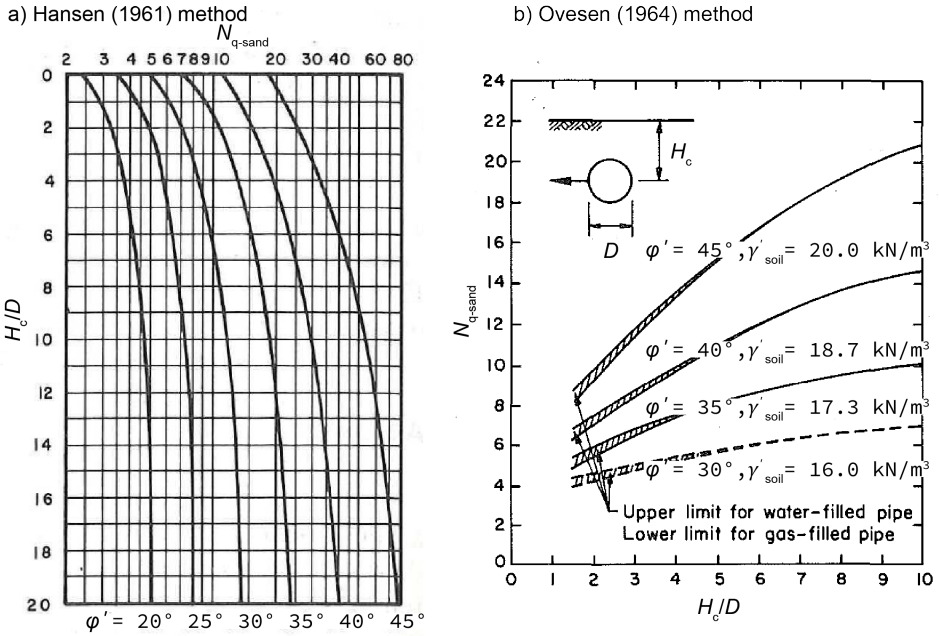

Figure 2.2: Bearing capacity factor ($N_{\text{q-sand}}$) as a function of pipe embedment ratio (H_c/D) and soil internal friction angle (φ'): a) Hansen method modified after Audibert and Nyman (1977); b) Ovesen method modified after Trautmann and O'Rourke (1985)

Equation 2.3 to extrapolate Equation 2.1 into the condition when there is seepage flow or excess pore pressure in the sand layer, where γ_w is the unit weight of water.

$$\text{sand: } q_u = (\gamma'_{soil} - i\gamma_w) H_c N_{\text{q-sand}} \tag{2.3}$$

Calvetti et al. (2004) suggested to use the Hansen method for the $N_{\text{q-sand}}$ factor, as both the experimental and numerical (distinct element method) simulation results showed a good agreement with the Hansen method (when $\varphi' = 35°$). It was explained that the inconsistent in the values of φ' can be attributed to the low confining stress during the laboratory tests.

Trautmann et al. (1985) and Guo and Stolle (2005) reported that the existing methods provide a considerable variation in the prediction of the ultimate soil restraint associated with the relative soil-pipeline displacement. They pointed out that, the difference in $N_{\text{q-sand}}$ provided by the methods developed by Hansen (1961) and Ovesen (1964) can differ about two times in medium or dense sand when the value of H_c/D is between 3 and 4. This is attributed not only to the difference in soil density, pipe diameter and burial depth, but also the difference in testing conditions including boundary conditions and the relative soil-pipeline movement rate.

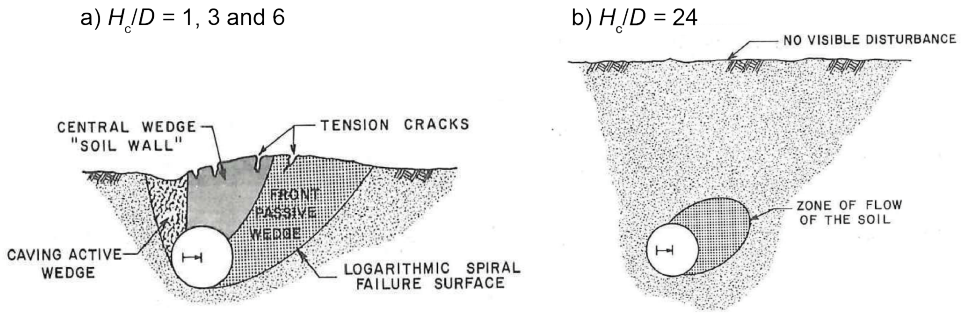

Figure 2.3: Failure mechanisms of pipe buried at various embedment ratios, modified after Audibert and Nyman (1977)

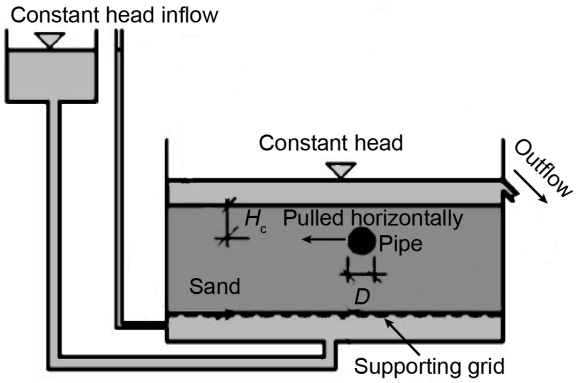

Figure 2.4: Test set-up developed by Calvetti et al. (2004)

2.1.2. Fluid dynamics approach

In the later stages of marine landslides, the sliding soil is regarded as low strength debris flow or turbidity current as illustrated in Figure 1.1. The soil/fluid mass is assumed to be liquefied and behaves as a non-Newtonian fluid, such as Bingham fluid or Herschel–Bulkley fluid (Boukpeti et al., 2012b, Locat and Lee, 2002, O'Brien and Julien, 1988, Pazwash and Robertson, 1975). Therefore, the fluid dynamics approach has been applied to study the impact loads/pressures on offshore pipelines subjected to debris flows (Boukpeti et al., 2012a, Zakeri, 2009). Equation 2.4 has been used to evaluate the pressure acting on a pipeline:

$$q_{\mathrm{u}} = \frac{1}{2} C_{\mathrm{D}} \rho_{\mathrm{slide}} V_{\mathrm{slide}}^2 \tag{2.4}$$

where, C_{D} is a drag coefficient, ρ_{slide} and V_{slide} are the density and velocity of the sliding soil, respectively. (Note that V_{slide} represents the relative pipe-soil velocity as the pipe was kept in position during the corresponding tests.) Zakeri et al. (2008) studied the impact loads on pipe induced by subaqueous gravity flow by conducting

experiments in a 9.5-m long flume as shown in Figure 2.5. In these tests, the pipe was either suspended above or laid on the flume bed, and the slurry made of clay and water was released from a distance of 6.2 m to the pipe location. Zakeri et al. (2008) defined C_D as a function of the non-Newtonian Reynolds number, $Re_{\text{non-Newtonian}}$, as shown in Equation 2.5. The definition of Reynolds number for a Newtonian fluid is presented Equation 2.6, where μ_{slide} is the dynamic viscosity of the sliding material and $\dot{\gamma}$ (in Equation 2.7) is the shear rate. Zakeri et al. (2008) took the sliding material as a shear-thinning non-Newtonian fluid material and defined the non-Newtonian Reynolds number (in Equation 2.8) in line with the definition of $Re_{\text{Newtonian}}$ for a Newtonian fluid, where μ_{app} is the apparent dynamic viscosity. Based on the power law model, they assumed that the mobilised shear stress of the sliding soil τ_{slide} has a power low relationship with $\dot{\gamma}$ and μ_{app} is defined as the ratio of τ_{slide} to $\dot{\gamma}$ (see Equation 2.9) , where a and n are constant factors. Note that the value of τ_{slide} is identical to the soil undrained shear strength, s_u, however, the terms of τ_{slide} and s_u are used for fluid dynamics approach and geotechnical approach, respectively, to emphasize the difference between the two approaches.

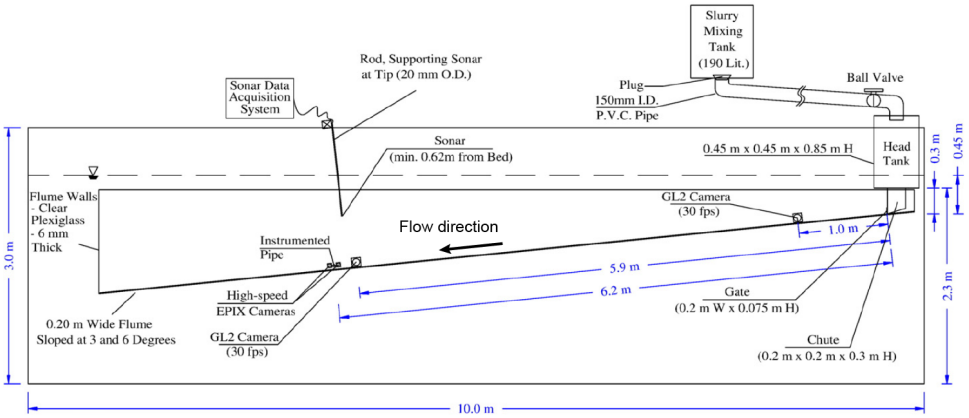

Figure 2.5: Experiment set-up developed by Zakeri et al. (2008)

$$\begin{cases} C_D = 1.4 + \dfrac{17.5}{Re_{\text{non-Newtonian}}^{1.25}} \\ C_D = 1.25 + \dfrac{11.0}{Re_{\text{non-Newtonian}}^{1.15}} \end{cases} \tag{2.5}$$

$$Re_{\text{Newtonian}} = \frac{\rho_{\text{slide}} V_{\text{slide}} D}{\mu_{\text{slide}}} = \frac{\rho_{\text{slide}} V_{\text{slide}}^2}{\mu_{\text{slide}} \dot{\gamma}} \tag{2.6}$$

$$\dot{\gamma} = V_{\text{slide}} / D \tag{2.7}$$

$$Re_{\text{non-Newtonian}} = \frac{\rho_{\text{slide}} V_{\text{slide}}^2}{\mu_{\text{app}} \dot{\gamma}} = \frac{\rho_{\text{slide}} V_{\text{slide}}^2}{\tau_{\text{slide}}} \tag{2.8}$$

$$\tau_{\text{slide}} = a\dot{\gamma}^n \text{ and } \mu_{\text{app}} = \frac{\tau_{\text{slide}}}{\dot{\gamma}} \tag{2.9}$$

With the set-up shown in Figure 2.5, Zakeri (2009) carried out a series of flume tests and analysed the impact forces exerted on the model pipe. Various slurry materials were made of water (35% by mass), kaolin clay (10% to 35% by mass) and silica sand. The slurry velocities before hitting the pipe varied from 0.5 m/sec to 1.35 m/sec. Pipes with outer diameters (D) of 22.2 mm and 28.6 mm were selected and placed either on the floor (laid-on-seafloor pipe) or 1 D above the floor (suspended pipe). Computational fluid dynamics simulations were conducted to simulate the flume tests as well. Results of the laboratory tests and numerical simulations are presented in Figure 2.6 which presents the relationship between C_{D} and $Re_{\text{non-Newtonian}}$ in line with Equation 2.5.

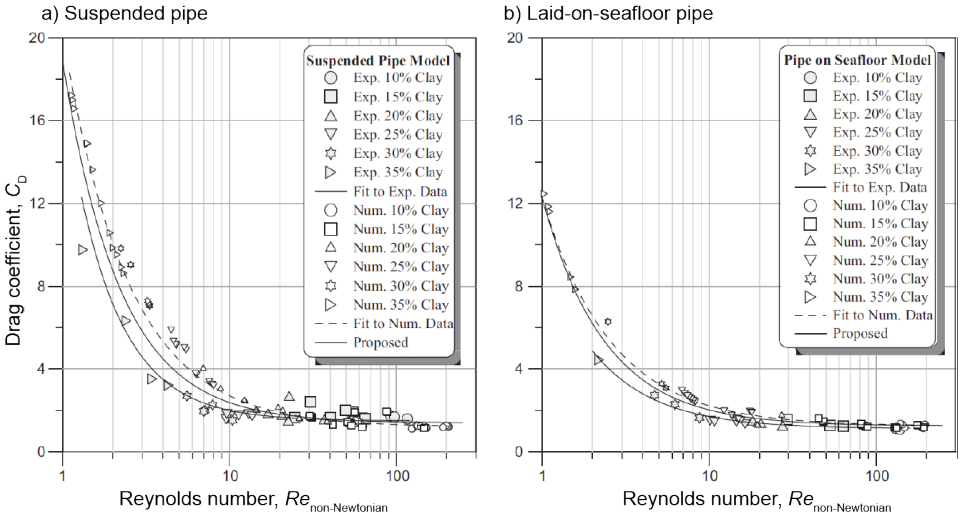

Figure 2.6: Drag coefficient (for the case when the debris flow direction is normal to pipe axis) as a function of non-Newtonian Reynolds number (modified after Zakeri (2009))

2.1.3. Hybrid approach

Randolph and White (2012) evaluated the flume tests results conducted by Zakeri (2009) and proposed a hybrid approach (as expressed in Equation 2.10) to evaluate the debris flow effects on offshore pipelines. This approach is a combination of the fluid dynamics approach (the first term in Equation 2.10) and geotechnical approach (the second term in Equation 2.10).

$$q_{\text{u}} = \frac{1}{2} C_{\text{D}} \rho_{\text{slide}} V_{\text{slide}}^2 + s_{\text{u}} N_{\text{q}} \tag{2.10}$$

$$s_{\mathrm{u}} = s_{\mathrm{u,ref}} \left(\frac{\dot{\gamma}}{\dot{\gamma}_{\mathrm{ref}}} \right)^{\eta} \tag{2.11}$$

2

Here, the undrained shear strength s_{u} is shear strain rate ($\dot{\gamma}$) dependent and $s_{\mathrm{u,ref}}$ is the undrained shear strength tested at a reference shear strain rate ($\dot{\gamma}_{\mathrm{ref}}$); η is the power law coefficient and is typically less than 0.2 for most of the natural soil (Jeong et al., 2009); N_{q} is a constant bearing capacity factor which is estimated to be 9.1 for a fully smooth pipe and 11.9 for a fully rough pipe (Martin and Randolph, 2006, Randolph and Houlsby, 1984).

Sahdi et al. (2014) performed a series of drum centrifuge tests to assess the soil restraint on buried pipes. The pipe was dragged horizontal in clay material with H_{c}/D = 2.5 and velocities ranging from 0.004 m/sec to 4.2 m/sec. The effects of soil strength, density and relative soil-pipeline velocity on the soil resistance were studied. Sahdi et al. (2014) followed the hybrid approach (Equation 2.10) and further argued that when the $Re_{\text{non-Newtonian}}$ is smaller than 3, then the geotechnical component dominates the overall resistance. They found that C_{D}=1.06 and N_{q}=7.35 fit their centrifuge tests results well. Sahdi et al. (2014) believed that a full-flow failure mechanism was not established with the tested embedment ratio (H_{c}/D = 2.5) which was the reason that the value of N_{q} is lower than the range of 9.1 –11.9 predicted by Randolph and Houlsby (1984).

2.2. Centrifuge modelling of offshore soil-pipeline interaction

2.2.1. Testing under drained conditions

Pipeline-soil behaviour under drained conditions has been studied by conducting model tests either in saturated sand with low pipe moving rate, or in dry sand. With the aim of extrapolating the knowledge in soil-anchor plate interaction mechanisms to soil-pipeline interaction mechanisms, Dickin (1988) performed centrifuge tests at $40g$. In these tests, the anchor plate and pipeline were buried in both loose and dense dry sand samples with embedment ratios ranging from 1 to 11 and enforced to move laterally. Dickin (1988) found a great similarity in the force-displacement behaviour of the two structures.

Krstelj (1997) compared the geotechnical loads on pipelines buried in a dry sand layer obtained from centrifuge model tests with the theoretical results from both Ovesen (1964) and Hansen (1961) methods. He observed that the test results agreed well with the expectation from the Ovesen (1964) method, while the results were around 50% of the expectation from the Hansen (1961) method.

With the purpose of calibrating a constitutive model for describing soil-pipe interaction in calcareous sand, Tian et al. (2010) studied the pipe behaviour by conducting centrifuge tests at $50g$. The drained condition was achieved by using water as the pore fluid and using a normalized pipe velocity ($V_{\mathrm{pipe}}D/c_{\mathrm{v}}$) of 0.002, where V_{pipe} is pipe velocity (V_{pipe} represents the relative pipe-soil velocity as the sandy layer was kept in place during the tests) and c_{v} is the soil consolidation coefficient. (Note

that V_{pipe} is used to emphasize the pipe moved actively during the tests, although it is identical to V_{slide} which is used to describe the moving soil velocity.) Chung et al. (2006) argued that a normalized pipe velocity larger than 0.01 is considered to be a fully undrained condition.

2.2.2. Testing under undrained conditions

Paulin (1998) has conducted several centrifuge tests with the pipes laterally pulled in clay material as illustrated in Figure 2.7. The pipe had a prototype diameter of 0.95 m and were loaded with a variety of pipeline displacement rates ranging from 0.3 m/year to 315 m/year in prototype scale in order to simulate both drained and undrained pipeline-soil interaction. A rate effect was discovered, i.e. the loads experienced by the pipeline under an undrained loading condition was smaller than that under a drained loading condition. Furthermore, it was observed that the embedment ratio can significantly influence the lateral load when $H_c/D < 1.84$, but the influence was insignificant when the pipe was buried deeper.

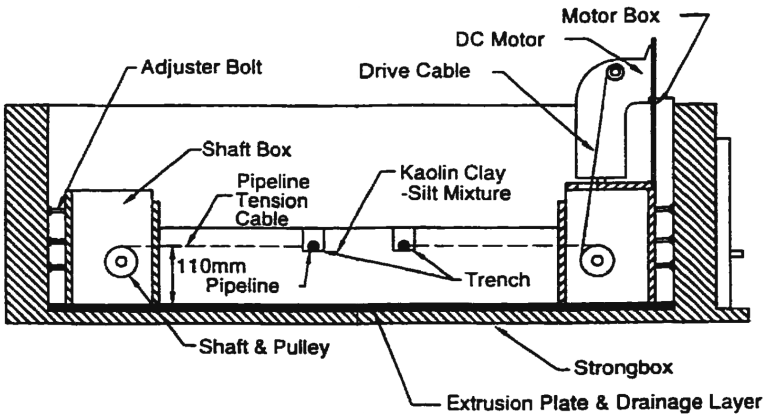

Figure 2.7: Illustration of centrifuge test set-up (side view) designed by Paulin (1998)

Zakeri et al. (2012) designed a test set-up with a releasable gate, as shown in Figure 2.8, to study the drag force impacted on an offshore pipeline induced by sliding clay blocks. A series of tests were carried out at 30g with two pipe prototype diameters: 0.19 m and 0.29 m. The clay blocks were made of kaolin clay with shear strengths in the range of 4 kPa to 8 kPa. The impact shear strain rates of the clay blocks were between 4 sec^{-1} and 137 sec^{-1}. By fitting the experimental results, Zakeri et al. (2012) found that the factor $N_{\text{q-clay}}$ in Equation 2 was shear strain rate ($\dot{\gamma}$) dependent, which can be expressed as $N_{\text{q-clay}} = 7.5\dot{\gamma}^{0.12}$.

Oliveira et al. (2017) designed a centrifuge testing system integrated with a moving plate which can move actively to push the clay type soil towards a buried pipe as shown in Figure 2.9a. The pipe was placed in the clay layer with two end fixity conditions: i) fixed ends (Figure 2.9b), i.e. the pipe was fixed to the side walls of the centrifuge box with rotational joints; ii) free ends (Figure 2.9c), i.e. there was gaps between the ends and the walls of the model box. The loads acting on

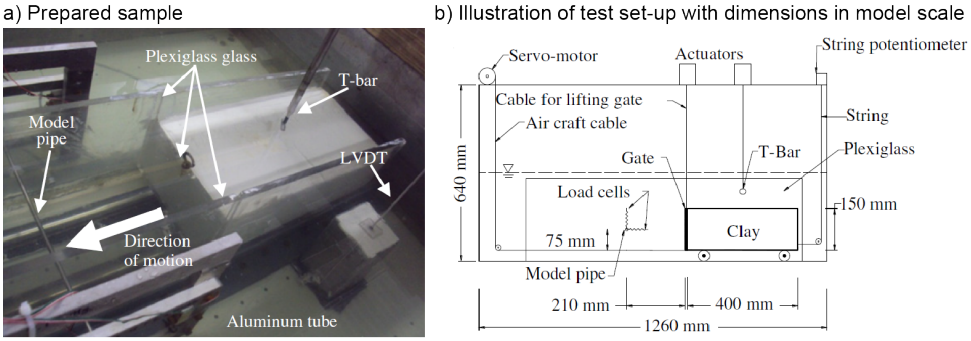

Figure 2.8: Centrifuge test set-up developed by Zakeri et al. (2012)

the pipes with different end resistance conditions were compared. It was found that the pipe movement flexibility (or pipe restraints) determines the load acting on the pipe due to the soil movement. Oliveira et al. (2017) observed that the pipe with free ends experienced bigger displacement and less soil resistance than the pipe with fixed ends.

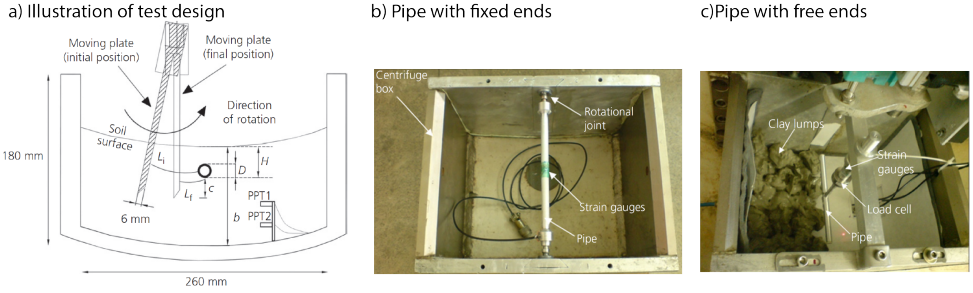

Figure 2.9: Illustration of the centrifuge test set-up developed by Oliveira et al. (2017) with dimensions in model scale (PPT: pore pressure transducer)

2.3. Centrifuge modelling on the initiation of offshore slope liquefaction

Marine landslide induced by liquefaction has been recognised as one of the major offshore geo-hazards. Considering the loading conditions of the triggering mechanisms of offshore slope liquefaction, these failures can be categorised into monotonic-load-induced slope liquefaction and dynamic-load-induced slope liquefaction. The monotonic load examples include rapid accumulation of sediments, seabed erosion, dredging, displacing of soil due to movement of icebergs and some human construction activities; the dynamic load examples include earthquakes, tsunamis, currents and waves. Abundant research has been done with a focus on the triggering and failure mechanisms of subaqueous slope failure. These research

works cover constitutive modelling, laboratory element testing, physical modelling (both at $1g$ and Ng) and numerical modelling. Among them, only some relevant research works adopting centrifuge modelling approach are discussed below.

2.3.1. Dynamic-loads-induced slope liquefaction

Centrifuge modelling has been used to study the behaviour of subaqueous slope/seabed under dynamic loads, among which cyclic loading conditions related to earthquakes (e.g. Coulter and Phillips, 2003, Elgamal et al., 2005, Huang et al., 2014, Ling et al., 2003, Sharp et al., 2003, Takahashi et al., 2019) and waves (e.g. Miyamoto et al., 2020, Sassa and Sekiguchi, 1999, Sekiguchi et al., 1998) have been investigated. Sassa and Sekiguchi (1999) have conducted centrifuge tests with a focus on wave-induced liquefaction of loosely packed sandy seabed under two types of wave modes, namely progressive waves and standing waves. The developed test set-up is presented in Figure 2.10. They proposed a criteria for evaluating the liquefaction of a sandy seabed under wave loads, which is expressed in terms of the cyclic stress ratio. The cyclic stress ratio is defined as the ratio of the wave-induced maximum shear stress to the initial vertical effective stress. Sassa and Sekiguchi (1999) argued that liquefaction can happen when the cyclic stress ratio exceeds 0.14 and 0.20 under progressive-wave loading condition and standing-wave loading condition, respectively.

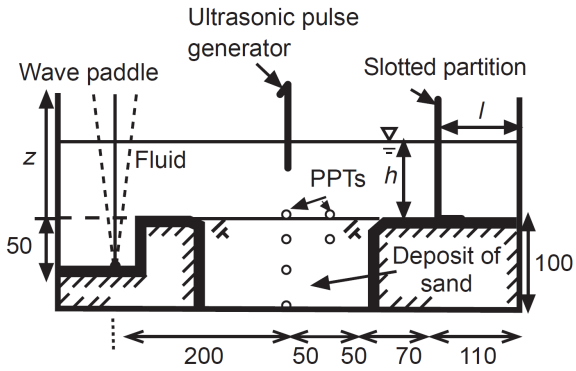

Figure 2.10: Illustration of the centrifuge test set-up developed by Sassa and Sekiguchi (1999) with dimensions in mm in model scale

Sharp et al. (2003) simulated earthquake-induced liquefaction using an inclined laminar box at $50g$. The effects of relative density (Dr), input peak acceleration (a_{max}) and sample permeability (k) on the liquefied soil thickness ($H_{\text{liquefaction}}$) were investigated. They found that $H_{\text{liquefaction}}$ decreases as Dr increases, $a_{\max}$ drops or k increases. In all the centrifuge tests, the soil lateral movement ceased as the shaking ended.

2.3.2. Monotonic-loads-induced slope liquefaction

There are less centrifuge experiments that have been conducted focusing on seabed liquefaction triggered by monotonic loads than that induced by dynamic loads. The Canadian Liquefaction Experiment (CANLEX) project involved a centrifuge model test to study the failure behaviour of a subaqueous slope under undrained monotonic loading (Phillips and Byrne, 1995). As shown in Figure 2.11, the submerged slope was made of oil sand tailings with a relative density of around 30%, a slope angle of 16° and a prototype height of 8.8 m. Both undrained triaxial compression and extension tests were conducted on the sand material. Based on the triaxial tests results, static liquefaction could be expected when the soil is under extension condition rather than under compression condition, since strain softening behaviour was noticed in the triaxial extension tests, whereas strain hardening behaviour was observed in the triaxial compression tests.

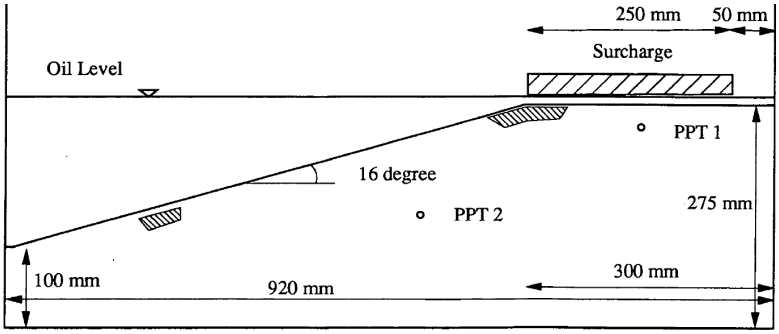

Figure 2.11: Illustration of the test model designed to simulate static liquefaction of a subaqueous slope in centrifuge with dimensions in model scale (Phillips and Byrne, 1995)

In the centrifuge test of CANLEX project, a steel surcharge was dropped on the slope crest firstly at $50g$, which applied a static pressure of 43 kPa. An increase in pore pressure and redistribution of pore pressure were observed, however no significant movements of the slope occurred due to the dissipation of pore pressure. Then, a new surcharge load offering a static pressure of 87 kPa was applied on the same slope sample after the previous surcharge was removed. The slope liquefaction was observed 0.25 seconds after the surcharge dropped on the slope crest indicated by the vertical sink of the surcharge and soil flow. A large deep-seated lateral soil flow was noticed and the slope rested at a the slope angle of $7°$. This slope failure initiated at the slope toe due to the strain softening behaviour of sand which increased the pore pressure.

Zhang et al. (2015) explored liquefaction of offshore sloping sediments initiated by elevated pore pressures as a result of gas hydrate dissociation. Samples consisted of two layers - a layer of kaolin clay on the top and a thin sand layer at the bottom (see Figure 2.12a). The elevated pore pressures were simulated by introducing pressurized water into the sand layer from base as shown in Figure 2.12b. It was found that excess pore pressure ratios of 1.27 and 0.54 were necessary to trigger the failure of the slopes with slope angles of $15°$ and $25°$, respectively.

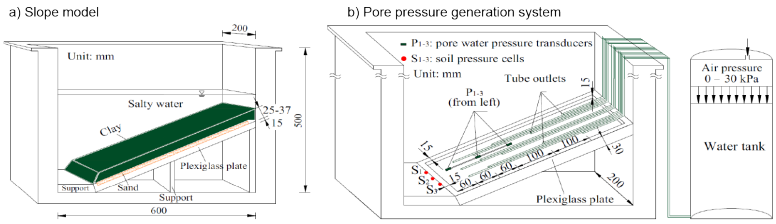

Figure 2.12: Illustration of the centrifuge model of a subaqueous slope (after Zhang et al. (2015))

2.4. Summary

A brief literature review on the topics including the experimental study on the soil-pipeline interaction and centrifuge modelling on the initiation of subaqueous slope failure has been presented in this chapter. Based on the literature study, the following conclusions can be drawn:

- Offshore pipeline-soil interaction has been widely investigated under the frameworks of geotechnical approach and fluid dynamics approach. However, it should be noted that either approach is suitable for certain specific engineering conditions. It is found that the initiation of an offshore sloping ground liquefaction in the vicinity of a buried pipeline is a case that has not been investigated yet;
- Centrifuge modelling techniques have been extensively used to study pipeline-soil behaviour with more focus on clay type materials and much less focus on sandy materials;
- The available methods provide a wide range of prediction on the landslide-induced loads on pipelines;
- The majority of centrifuge experiments triggered soil-pipeline displacement following the ”pulling-pipe” method which is not necessarily resembling reality.

References

Alliance, A. L. (2001). Guidelines for the design of buried steel pipe. *FEMA*, page 75.

Almahakeri, M., Fam, A., and Moore, I. D. (2013). Experimental investigation of longitudinal bending of buried steel pipes pulled through dense sand. *Journal of Pipeline Systems Engineering and Practice*, 5(2):04013014.

Ansari, Y., Kouretzis, G., and Sloan, S. W. (2019). Physical modelling of lateral sand-pipe interaction. *Géotechnique*, pages 1–16.

ASCE (1984). Guidelines for the seismic design of oil and gas pipeline systems. Report.

Audibert, J. M. and Nyman, K. J. (1977). Soil restraint against horizontal motion of pipes. *Journal of the Geotechnical Engineering Division*, 103(10):1119–1142.

Boukpeti, N., White, D., and Randolph, M. (2012a). Analytical modelling of the steady flow of a submarine slide and consequent loading on a pipeline. *Géotechnique*, 62(2):137–146.

Boukpeti, N., White, D., Randolph, M., and Low, H. (2012b). Strength of fine-grained soils at the solid–fluid transition. *Géotechnique*, 62(3):213–226.

C-CORE, Consulting, D. H., and SSD, I. (2009). Guidelines for constructing natural gas and liquid hydrocarbon pipelines through areas prone to landslide and subsidence hazards. Report.

Calvetti, F., Di Prisco, C., and Nova, R. (2004). Experimental and numerical analysis of soil–pipe interaction. *Journal of geotechnical and geoenvironmental engineering*, 130(12):1292–1299.

Chung, S. F., Randolph, M. F., and Schneider, J. A. (2006). Effect of penetration rate on penetrometer resistance in clay. *Journal of geotechnical and geoenvironmental engineering*, 132(9):1188–1196.

Coulter, S. and Phillips, R. (2003). *Simulating submarine slope instability initiation using centrifuge model testing*, volume 19, pages 29–36. Springer, Dordrecht.

Dickin, E. (1988). Stress-displacement of buried plates and pipes. In *Proceedings of the International Conference on Geotechnical Centrifuge Modeling (Centrifuge 88), Paris, France*, pages 25–27.

Elgamal, A., Yang, Z., Lai, T., Kutter, B. L., and Wilson, D. W. (2005). Dynamic response of saturated dense sand in laminated centrifuge container. *Journal of Geotechnical and Geoenvironmental Engineering*, 131(5):598–609.

Guo, P. and Stolle, D. (2005). Lateral pipe–soil interaction in sand with reference to scale effect. *Journal of geotechnical and geoenvironmental engineering*, 131(3):338–349.

Hansen, J. B. (1961). The ultimate resistance of rigid piles against transversal forces. *Bulletin 12, Danish Geotech. Institute*, pages 1–9.

Huang, B., Liu, J., Lin, P., and Ling, D. (2014). Uplifting behavior of shallow buried pipe in liquefiable soil by dynamic centrifuge test. *The Scientific World Journal*, 2014.

Jeong, S. W., Leroueil, S., and Locat, J. (2009). Applicability of power law for describing the rheology of soils of different origins and characteristics. *Canadian Geotechnical Journal*, 46(9):1011–1023.

Krstelj, I. (1997). *Behavior of laterally loaded pipes in dry and saturated sand (centrifuge testing)*. Doctoral dissertation.

Ling, H. I., Mohri, Y., Kawabata, T., Liu, H., Burke, C., and Sun, L. (2003). Centrifugal modeling of seismic behavior of large-diameter pipe in liquefiable soil. *Journal of geotechnical and geoenvironmental engineering*, 129(12):1092–1101.

Liu, R., Guo, S., and Yan, S. (2015). Study on the lateral soil resistance acting on the buried pipeline. *Journal of Coastal Research*, 73(sp1):391–398.

Locat, J. and Lee, H. J. (2002). Submarine landslides: advances and challenges. *Canadian Geotechnical Journal*, 39(1):193–212.

Martin, C. and Randolph, M. (2006). Upper-bound analysis of lateral pile capacity in cohesive soil. *Géotechnique*, 56(2):141–145.

Miyamoto, J., Sassa, S., Tsurugasaki, K., and Sumida, H. (2020). Wave-induced liquefaction and floatation of a pipeline in a drum centrifuge. *Journal of Waterway, Port, Coastal, and Ocean Engineering*, 146(2):04019039.

O'Brien, J. S. and Julien, P. Y. (1988). Laboratory analysis of mudflow properties. *Journal of hydraulic engineering*, 114(8):877–887.

Oliveira, J. R. M., Rammah, K. I., Trejo, P. C., Almeida, M. S., and Almeida, M. C. (2017). Modelling of a pipeline subjected to soil mass movements. *International Journal of Physical Modelling in Geotechnics*, 17(4):246–256.

Ono, K., Yokota, Y., Sawada, Y., and Kawabata, T. (2017). Lateral force–displacement prediction for buried pipe under different effective stress condition. *International Journal of Geotechnical Engineering*, pages 1–9.

Ovesen, N. K. (1964). Anchor slabs, calculation methods and model tests. *Bulletin*, 16:39.

Paulin, M. J. (1998). *An investigation into pipelines subjected to lateral soil loading*. Doctoral dissertation.

Pazwash, H. and Robertson, J. (1975). Forces on bodies in bingham fluids. *Journal of Hydraulic Research*, 13(1):35–55.

Phillips, R. and Byrne, P. (1995). Modeling flowslides caused by static loading. *Transportation Research Record*, pages 12–21.

Randolph, M. F. and Houlsby, G. (1984). The limiting pressure on a circular pile loaded laterally in cohesive soil. *Geotechnique*, 34(4):613–623.

Randolph, M. F. and White, D. J. (2012). Interaction forces between pipelines and submarine slides—a geotechnical viewpoint. *Ocean Engineering*, 48:32–37.

Roy, K. S. and Hawlader, B. (2012). Soil restraint against lateral and oblique motion of pipes buried in dense sand. In *International Pipeline Conference*, volume 45158, pages 7–12. American Society of Mechanical Engineers.

Sahdi, F., Gaudin, C., White, D., Boylan, N., and Randolph, M. (2014). Centrifuge modelling of active slide-pipeline loading in soft clay. *Géotechnique*, 64(1):16–27.

Sassa, S. and Sekiguchi, H. (1999). Wave-induced liquefaction of beds of sand in a centrifuge. *Geotechnique*, 49(5):621–638.

Sekiguchi, H., Kita, K., Sassa, S., and Shimamura, T. (1998). Generation of progressive fluid waves in a geo-centrifuge. *Geotechnical Testing Journal*, 21(2):95–101.

Sharp, M. K., Dobry, R., and Abdoun, T. (2003). Liquefaction centrifuge modeling of sands of different permeability. *Journal of geotechnical and geoenvironmental engineering*, 129(12):1083–1091.

Takahashi, H., Fujii, N., and Sassa, S. (2019). Centrifuge model tests of earthquake-induced submarine landslide. *International Journal of Physical Modelling in Geotechnics*, pages 1–13.

Tian, Y. and Cassidy, M. J. (2011). Pipe-soil interaction model incorporating large lateral displacements in calcareous sand. *Journal of Geotechnical and Geoenvironmental Engineering*, 137(3):279–287.

Tian, Y., Cassidy, M. J., and Gaudin, C. (2010). Advancing pipe–soil interaction models in calcareous sand. *Applied Ocean Research*, 32(3):284–297.

Trautmann, C. H., O'Rourfce, T. D., and Kulhawy, F. H. (1985). Uplift force-displacement response of buried pipe. *Journal of Geotechnical Engineering*, 111(9):1061–1076.

Zakeri, A. (2009). Submarine debris flow impact on suspended (free-span) pipelines: Normal and longitudinal drag forces. *Ocean Engineering*, 36(6-7):489–499.

Zakeri, A., Hawlader, B., and Chi, K. (2012). Drag forces caused by submarine glide block or out-runner block impact on suspended (free-span) pipelines. *Ocean Engineering*, 47:50–57.

Zakeri, A., Høeg, K., and Nadim, F. (2008). Submarine debris flow impact on pipelines—part i: Experimental investigation. *Coastal engineering*, 55(12):1209–1218.

Zhang, J., Lin, H., and Wang, K. (2015). Centrifuge modeling and analysis of submarine landslides triggered by elevated pore pressure. *Ocean Engineering*, 109:419–429.

Zhang, J., Stewart, D. P., and Randolph, M. F. (2002). Modeling of shallowly embedded offshore pipelines in calcareous sand. *Journal of geotechnical and geoenvironmental engineering*, 128(5):363–371.

3

Behaviour of Buried Pipes in Unstable Sandy Slopes

子曰：“温故而知新，可以为师矣。”

《论语. 为政篇》

Confucius said, “If a man keeps cherishing his old knowledge, so as continually to be acquiring new, he may be a teacher of others.”

Analects of Confucius

The content of this chapter has been accepted as research paper in Landslides, Zhang and Askarinejad (2019).

3.1. Abstract

Significant forces can be applied to embedded pipelines in sloping grounds due to soil instabilities, which potentially might lead to leakage of hazardous fluids into the environment. The soil-pipeline interaction in sandy slopes has been investigated experimentally using small scale physical models tested in a geotechnical centrifuge. A novel method is developed in this paper to estimate the ultimate external forces, induced by slope failures, acting on buried pipes at various locations inside the slope. Instabilities were triggered by surcharge loading on the slope crest in the centrifuge tests. Six dense coarse sandy slopes were tested with different pipe locations with respect to the slope crest. Moreover, two medium dense fine sand slopes were tested in the same manner to study the effect of the grain size distribution on the soil-pipe interaction. The external forces on the pipe induced by the surrounding soil movements were calculated based on the measurements of four strain gauges installed on the pipe. The shape of failure surface and pipe movements was monitored with the aid of advanced image processing techniques. The results indicate that a buried pipeline has the potential to affect the slope failure mechanism. Normalized force-pipe displacement relationships were derived and compared to the estimation methods suggested in previous studies which were mainly done on pipes installed in flat grounds. A new prediction method is introduced in this study which considers the pipe burial distance to the slope crest. Moreover, the slope angle effect on the ultimate force applied to the pipe is also investigated, and a generalised formula is developed. Finally, two examples of the application of the new method are presented for pipelines installed at the toe of two large scale subaerial and submarine slopes.

Key words*: Slope pipeline interaction, Physical modelling, Image analysis, Landslide, Pipeline*

3.2. Introduction

Pipelines are widely used to transport fluids over long distances and may pass through various geological and topographic conditions. Due to the environmental and safety concerns or constraints imposed by the land use, pipelines are sometimes placed in sloping ground in either onshore or offshore projects. However, relative movements of the soil and the pipe can impose major external loads to the structure, which might eventually result in the failure of pipelines along unstable slopes. It is reported that ground movement, such as slope instability, was the cause of 13% of European gas pipeline incidents during the period from 2004 to 2013 (Wu et al., 2017). The forces induced on the pipe by soil movements have a direct relationship with the relative soil-pipe movement (Chan and Wong, 2004, Feng et al., 2015, Rammah et al., 2014), and are categorised as one of the major threats to the pipeline operation. Therefore, reliable prediction of the external forces applied to the pipe as a result of slope instability is of utmost importance in the design or evaluation process. Moreover, the relationship between the peak external load and the corresponding pipe displacement, as well as the determination of the corresponding structural stresses or strains, are necessary for a safe design of pipelines buried in slopes.

During a slope or an embankment instability, an embedded pipe might move along a curved path with horizontal, vertical and/or longitudinal components (Figure 3.1a). Di Prisco and Galli (2006) indicated that the vertical and horizontal soil resistance have coupling effects. However, physical modelling of the soil-pipeline interaction is traditionally conducted by pulling or pushing the pipeline horizontally in level grounds using wires or rigid shafts along a constant direction (Figure 3.1b)(e.g. Almahakeri et al., 2013, Audibert and Nyman, 1977, Calvetti et al., 2004, Liu et al., 2015, Oliveira et al., 2009, Ono et al., 2017, Paulin, 1998, Roy and Hawlader, 2012, Sahdi et al., 2014, Tian and Cassidy, 2011, Trautmann et al., 1985, Zhang et al., 2002). Ignoring the direction of the pipe movement might result in an underestimation of the loads that can be exerted on the pipe (Calvetti et al., 2004).

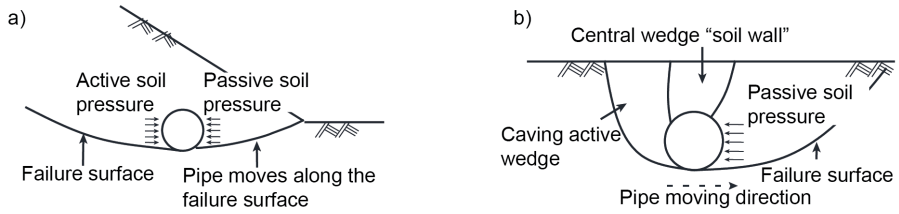

Figure 3.1: Failure mechanism: a) a pipe buried within a slope; b) a pipe pulled horizontally in a flat ground

3.2.1. Physical modelling of the soil–pipe interaction

Based on the results of small-scale tests on buried pipes pulled horizontally under a flat soil surface, Audibert and Nyman (1977) suggested that the ultimate soil

resistance (q_u) is expressed as:

$$q_u = \gamma H_c N_{uq} = F_{ud}/DL \tag{3.1}$$

where γ is the soil unit weight; H_c is the pipe embedment depth (from the soil surface to the centre of the pipe); N_{uq} is the ultimate bearing capacity factor proposed by Hansen (1961) which is also known as the ultimate dimensionless force; F_{ud} is the maximum drag force applied on the pipe; D and L are the pipe length and pipe diameter, respectively. Liu et al. (2015) designed several lateral pull-out tests to investigate the resultant forces on the pipelines both in sand and soft clay samples. They claimed that the lateral soil resistance increases with increasing embedment ratio, H_c/D. Oliveira et al. (2017) studied the lateral soil movement-pipe interaction in centrifuge conditions using a marine soil (soil internal friction angles, $\varphi' = 24.8°$). The soil movements were developed by moving a plate which was partially embedded into the clay samples towards the buried pipe. They observed that the induced force rises slightly as the embedment ratio increases.

Audibert and Nyman (1977) found that the normalized force-displacement relationship of a pipe pulled horizontally below a flat soil surface can be fitted by means of a hyperbolic curve as expressed by

$$\frac{F_d}{F_{ud}} = \frac{y/y_u}{a + b(y/y_u)} \tag{3.2}$$

where F_d is the drag force; y is the pipe movement; y_u is the pipe movement corresponding to F_{ud}; a and b are two model constants. Based on results from both loose and dense samples (φ' is $33°$ and $40°$, respectively, reported by Trautmann et al. (1985)), Audibert and Nyman (1977) found that all the results fell into a region bounded by an upper (a = 0.0486, b = 0.9554) and a lower (a = 0.2405, b = 0.7566) hyperbolic curves. Trautmann et al. (1985) fitted their test results using a = 0.17 and b = 0.83. Yimsiri et al. (2004) suggested a = 0.1 and b = 0.9 for deep-buried pipes in medium dense sand with H_c/D ranging from 11.5 to 100.

Trautmann et al. (1985) performed large-scale pipe pulling tests in a container with dimensions of 1.2 (length) x 2.3 (width) x 1.2 (depth) m^3 and discovered that N_{uq} increases linearly with H_c/D when H_c/D is less than eight. Hsu (1996) studied the soil restraint on pipelines which were pulled with various oblique angles with respect to the horizontal plane. They observed that N_{uq} decreases with the increase of the oblique angle, prominently when the oblique angle is within 45°. This observation is in agreement with the prediction of Nyman (1984) who extended the inclined anchor-soil behaviour to the buried pipe-soil behaviour.

For a pipe that moves 30° corresponding to the horizontal direction in loose sand sample ($\varphi' = 33°$), Hsu (1996) discovered that the $y_u = 0.075H_c$ and $0.085H_c$ for H_c/D = 3.5 and 1.5, respectively. Trautmann et al. (1985) suggested that the pipe displacement at the ultimate soil resistance, i.e. y_u in Equation 3.2, can be estimated as:

$$\begin{cases} y_u = 0.13H_c \text{ (for loose sand, } \varphi' = 31^\circ) \\ y_u = 0.08H_c \text{ (for medium dense sand, } \varphi' = 36^\circ) \\ y_u = 0.03H_c \text{ (for dense sand, } \varphi' = 44^\circ) \end{cases} \tag{3.3}$$

The majority of the experimental work conducted to study the soil-pipeline interaction is performed on small or medium scale models under normal Earth gravity conditions ($1g$). This type of physical modelling technique, although quite informative in a qualitative way, cannot be used reliably for quantitative analysis as the stress state of the soil in the model and prototype are different (Terzaghi, 1943). An alternative to this technique is the use of a geotechnical centrifuge. In a centrifuge test, a model with geometry N times smaller than the prototype is constructed and is tested under an enhanced acceleration field with a magnitude of N times Earth's gravity (Ng). This situation provides a gradient of body stresses within the model similar to the prototype, which ensures similar effective stresses and pore pressures at equivalent depths (Schofield, 1980, Taylor, 1995, Wood, 2014). The prototype behaviour is approximated in accordance with scaling laws in the centrifuge model testing. The major scaling laws are summarised in Table 3.1.

Table 3.1: Scaling laws for centrifuge model tests

Parameters	Unit	Model/prototype
Acceleration	m/sec^2	N
Dimensions (length, diameter, thickness)	m	$1/N$
Pipe external force (F_N)	kN/m	$1/N$
Pipe flexural rigidity (EI)*	kN·m	$1/N^3$
Pipe cross section outer strain (ε)	-	1
Bearing capacity factor (N_q)	-	1

*: I is the second moment of area per unit length

This paper presents the results of a series of centrifuge model tests with pipes buried in unstable dense sandy slopes. Slope failures were induced by the increasing loads at the slope crest. The interaction of the pipe and the unstable slope is studied to quantify the external forces exerted on the pipe due to the slope failures. Moreover, the influence of a buried pipe on the slope failure mechanism in terms of alterations in the shape of the failure surface is studied.

3.3. Physical modelling

3.3.1. Soil characterisation

Two types of sand were used in the tests of this study. The first one is the coarse grained, Merwede river Sand from the Netherlands, which is also known as the Delft Centrifuge Sand (DC Sand), and the second one is the fine Geba Sand. The geotechnical characteristics of these two sands are reported in Table 3.2. Direct shear tests with three normal stresses of 15.1 kPa, 31.0 kPa and 47.1 kPa were conducted on dense DC Sand samples with relative densities of Dr = 75%. Furthermore, drained triaxial tests at two cell pressures of 25 kPa and 100 kPa were

performed on Geba Sand samples with relative density of 55% to determine the internal friction angle. The grains of both sands are characterised as sub-angular based on image analysis techniques (De Jager et al., 2017, Maghsoudloo et al., 2017).

Table 3.2: Geotechnical characteristics of Delft Centrifuge Sand and Geba Sand

Property	DC Sand	Geba Sand
$D_{10}, D_{30}, D_{50}, D_{60}$ (mm)	0.74, 0.85, 0.92, 0.98	0.078, 0.110, 0.117, 0.121
Specific gravity, G_s (-)	2.65	2.67
Minimum void ratio (-)	0.52	0.64
Maximum void ratio (-)	0.72	1.07
Residual friction angle (°)	33.6	36.0

3.3.2. Centrifuge test set-up

The tests were performed using the beam geotechnical centrifuge at TU Delft which has an arm radius of 1.22 m and is capable of creating an acceleration field of 300 times Earth's gravity ($300g$) with a maximum payload of 30 kg (Allersma, 1994, Askarinejad et al., 2017). A strongbox was designed with two transparent Plexiglas walls in order to monitor the movements of the sand grains and the pipe assuming a plane strain condition (Figure 3.2). The strain field of the slope as well as the movements of the pipe during the loading on the slope crest were monitored using a high resolution digital camera facing the transparent side of the model. The images were analysed using the PIV technique (Askarinejad et al., 2015, Stanier et al., 2015, White et al., 2003). All tests were conducted at a centrifugal acceleration field of $30g$.

Model preparation

The samples were prepared using the dry pluviation technique (Pozo et al., 2016, Presti et al., 1992) in four steps:

1. Sand layers were poured into the strongbox up to the pipe position level.
2. The pipe was placed carefully on the sand bed.
3. The sand pluviation was resumed to form a flat horizontal layer up to the crest level of the eventual slope.
4. Thin layers of sand were carefully excavated from the model to form the slopes.

The sand falling height during the dry pluviation was kept fixed at 160 mm from the sand surface and the diffuser ratios (nozzle diameter/D_{50}) for DC Sand and Geba Sand samples were 6.0 and 25.4, respectively. The variation in the attained relative densities of the samples was very low and the average relative densities for the DC and Geba Sand samples were 71% (with a standard deviation of 3%)

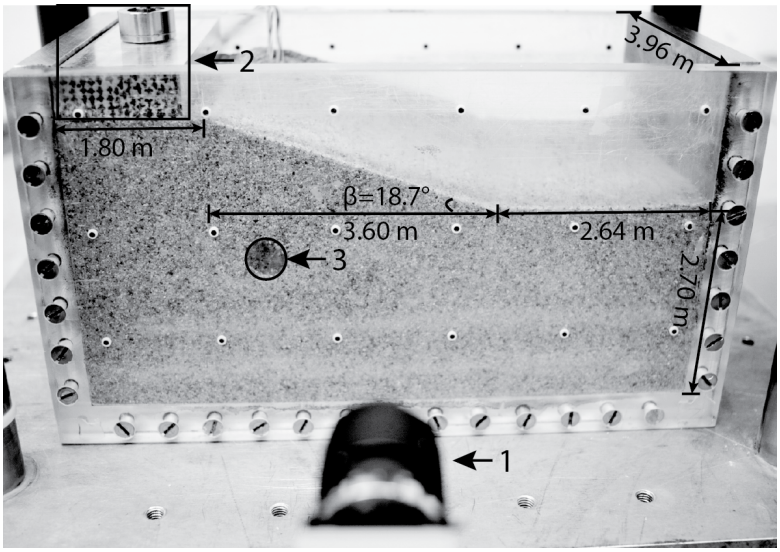

Figure 3.2: Test set-up: 1) High resolution digital camera; 2) load cell and footing; 3) instrumented pipe (dimensions in prototype scale).

and 43% (with a standard deviation of 1%), respectively. The final slopes have a length of 3.6 m (prototype scale) and angle of 18.7°.

Slope instabilities were induced by pushing a rigid footing onto the slope crests. The footing was connected to the displacement-controlled actuator using a rigid loading rod. A load cell with a capacity of 5 kN (equivalent to 4.5 MN in prototype scale) was installed between the loading rod and the footing.

The dimensions of the pipe have been selected based on three criteria: 1) D/D_{50} ratio, 2) the typical diameter and thickness of the gas pipes in practice and 3) the dimensions of the strong box of the centrifuge. Accordingly, a hollow steel pipe (Young's modulus E = 193 GPa) with the outer diameter of D = 18 mm (540 mm in prototype scale), wall thickness of t = 0.5 mm (15 mm in prototype scale) and length of L = 132 mm (3.96 m in prototype scale) was used as the model pipe in these tests (Figure 3.3).

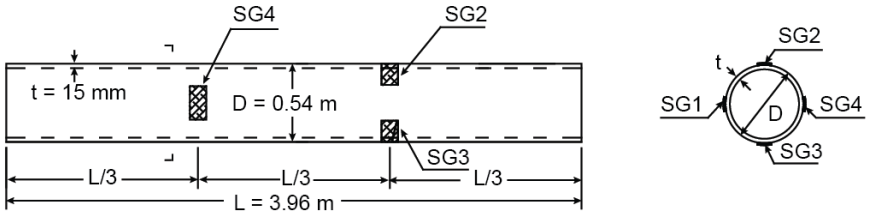

Figure 3.3: Steel pipe in prototype and strain gauges (SG1 to SG4) installation.

The model pipe dimensions have been selected based on typical gas pipes in

practice (e.g. Folga, 2007). Since the pipe dimensions including the thickness are scaled down by a factor of N as shown in Table 3.1, and the same material is used for the model pipe as the one in prototype, the scaling factor of pipe flexural rigidity is also satisfied (Taylor, 1995). Moreover, this ensures that the outer strain of pipe cross section in model scale is equal to that in prototype scale.

Ovesen (1981) investigated the uplift capacity of anchor slabs in dry sand by conducting both centrifuge and field tests. While varying the B/D_{50} ratio, where B is the width of the anchor slab, no scale error was observed if B/D_{50} = 25 in the centrifuge tests. Considering the analogy between anchor slab and a pipe as suggested by Garnier et al. (2007) and the fact that the value of D/D_{50} for DC sand is about 20, the particle size effect is evaluated to be minor or negligible in the tests of this study. Four strain gauges of type FLA-1-350-11 were installed at 90° angles on the pipe to monitor the cross section deformations caused by the external forces during the slope instability.

3.3.3. Testing programme

In total, eight tests were conducted on sandy slopes with and without buried pipes (Table 3.3). Six tests were performed on sample slopes built with DC Sand (NP, P1 to P5) and the other two were made on slopes with Geba Sand (NPG and P1G). While the geometry of all slopes is identical, the position of the pipes has been altered over 5 locations (P1 to P5). The geometry of the slopes in prototype scale and the location of the pipes are shown in Figure 3.4. For clarity, all tests were named based on the pipe positions. Pi represents the pipe at location i, where i = 1 to 5 (as shown in Figure 3.4 and summarised in Table 3.3); while NP is the test without a pipe. The added letter G to the last two tests refers to the Geba Sand tests. All tests were repeated at least once to check the reproducibility of the results.

Table 3.3: Summary of relative densities, pipe positions and embedment ratios

Test name	Dr	Pipe position		H_c/D
	(%)	X (m)	Y (m)	(-)
NP	70.7	-	-	-
P1	70.6	2.4	1.8	2.96
P2	69.4	2.4	1.2	1.85
P3	69.8	2.4	2.4	4.07
P4	70.0	3.6	1.8	2.22
P5	71.5	4.8	1.8	1.48
NPG	43.6	-	-	-
P1G	43.4	2.9	2.6	4.11

Pipe locations were designed based on the shape and location of the failure surface in the samples without a pipe which is regarded as the potential failure surface (PFS). The displacements and the shear strains of the samples as well as the exact location of the failure surfaces were obtained using the PIV method. For the DC Sand tests, firstly, the test without the pipe (NP) was conducted aiming

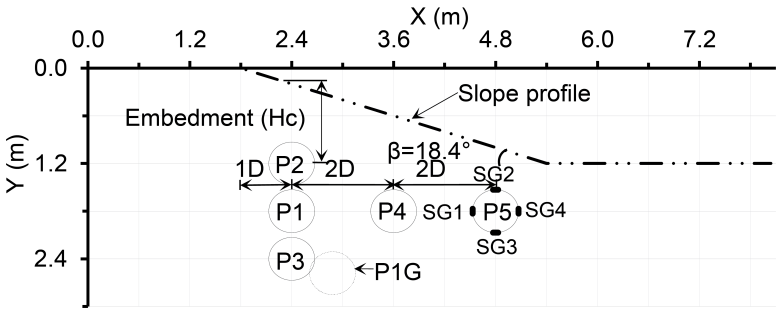

Figure 3.4: Five pipe locations for DC Sand tests (P1 to P5) and one pipe location for Geba Sand test (P1G)

to investigate the location of the PFS. Thereafter, five pipe locations (Figure 3.4) were selected to measure the loads applied to the pipes and to explore the effect of the pipes on the shape of the failure surface. Accordingly, pipe of the test P1 was placed at the deepest point of PFS, whereas, pipes of P2 and P3 were approximately $1D$ (one pipe diameter) above and below P1, respectively. P4 and P5 were approximately $2D$ and $4D$ further away from P1 towards the slope toe, respectively.

3.4. Results & Discussion

3.4.1. Failure mechanisms

Incremental shear strain plots at three successive normalized foundation settlements (ξ) of tests P1 and P3 are shown in Figure 3.5 and Figure 3.6, respectively. The factor ξ indicates the ratio between the footing settlement (δy_f) and the footing width (B_f). The incremental shear strain plot is the shear strain map obtained from two successive captured images during the loading process, and illustrates the location of the shear band in the slope. Figure 3.7 shows all of the incremental shear strain plots for DC Sand samples when the corresponding failure surfaces were fully formed.

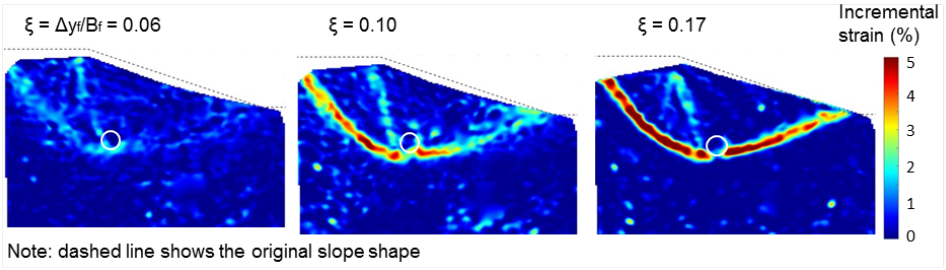

Figure 3.5: Incremental shear strain plots for test P1 at three successive normalized footing

Figure 3.5 and Figure 3.6 indicate that the shear strains initiated at the edges of the footing and extended towards the pipe at the early stages of the loading. With

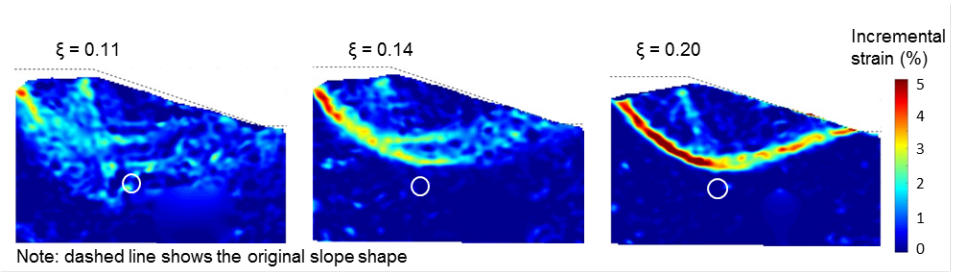

Figure 3.6: Incremental shear strain plots of test P3 at three successive normalized footing settlements

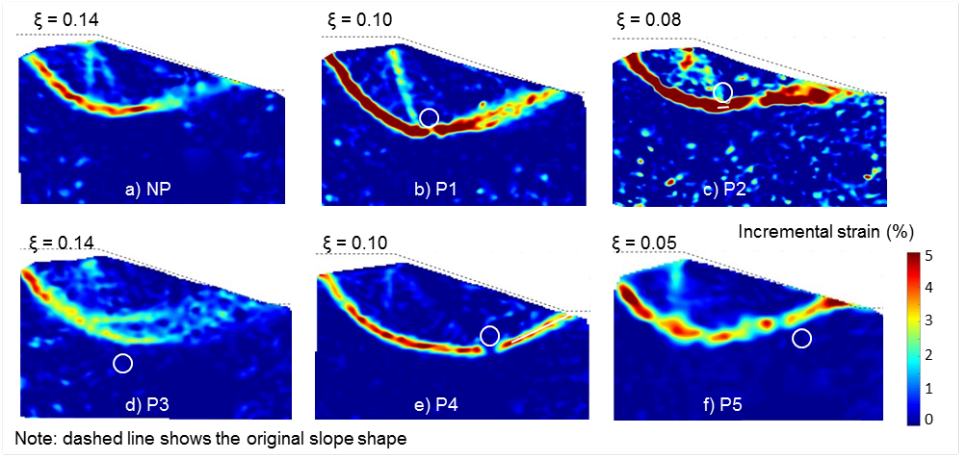

Figure 3.7: Failure surfaces of various models at peak bearing capacities of footing

increasing ξ, a shear band became more noticeable. The slope failure happened when the value of ξ reached about 0.10. It is obvious that the failure surface of test P1 (FS_P1) passes below the pipe and the same phenomenon can be observed in tests P2 and P4 (Figure 3.7). The failure surfaces of both tests P3 (Figure 3.6, FS_P3) and P5 (Figure 3.7, FS_P5) were above the pipes which are the deepest and farthest pipe positions with respect to the crest. These observations imply that only if the pipe is placed at a location close enough to the potential failure surface can the failure surface pass below the pipe.

All failure surfaces are summarised in Figure 3.8. By taking PFS as a benchmark, it is notable that the existence of the pipes influenced the propagation of the failure surfaces. Results of the tests in which the pipes were horizontally placed at about $1D$ distance to the crest edge (P2, P1 and P3) show that a deeper pipe results in a deeper failure surface. Failure surfaces in tests P1 and P2 formed beneath their respective pipes. Hence, the pipe can be regarded as a weak zone in each sample. There are two reasons: first, the hollow pipe is lighter than the soil mass with the same volume; second, the sand-pipe interface is smoother than the sand-

sand interface. For the test P3, though FS_P3 did not form below the pipe, it was deeper than FS_P1 and FS_P2. As P3 was about $1D$ deeper than PFS and had the highest confining stress condition, it moved the least (further shown in Figure 3.10). However, the amount of soil mass just above the crown of P3 was easier to deform compared with the soil at the same place of the test NP. This explains the fact that the first half of FS_P3 was steeper than that of PFS (Figure 3.8).

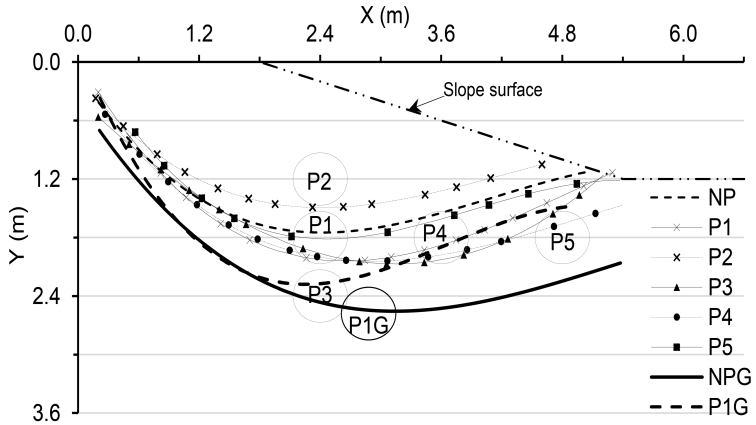

Figure 3.8: Failure surfaces of both DC Sand samples and Geba Sand samples

Similarly, results of the tests in which the pipes were positioned at the same horizontal level (P1, P4 and P5) illustrate that the influence of the pipes on the failure surfaces was getting less significant with increasing burial distance to the slope crest. The failure surface of P4 ended further than FS_P1, as P4 was buried further than P1. It is observed that FS_P5 was very close to PFS (Figure 3.8) which indicates that P5 hardly affected the slope failure. This might be due to the fact that it was the closest pipe to the slope toe and also lower than PFS. Comparing the effects of pipes on the failure mechanisms, it can be inferred that if a pipe is buried no more than $0.5D$ below PFS, the failure surface tends to pass below the pipe.

Comparing the test NPG with the test NP, the failure surface location of NPG is generally lower than that of NP (Figure 3.8). Furthermore, the failure surface of P1G developed above the pipe when the pipe was placed at the lowest point of the failure surface of NPG. This is a different behaviour compared to the test P1 but is similar to the test P3. P1G was close to but lower than P3 and had a larger value of H_c/D ratio than that of P3 which might result in the failure surface passing above P1G.

3.4.2. Pipe movement

It can be assumed that the friction between the pipe ends and the strong box walls is less than that between the sand grains and the side walls. Furthermore, to

prevent ingress of sand particles, the two ends of the pipe were carefully covered with thin lubricated layers of plastic. Hence, the friction between the strong box wall and the pipe is considered to be insignificant. Markers were made on the pipe end cover which was facing the camera in order to track the pipe movement using PIV method.

The traces of P1, P2 and P4 are demonstrated in Figure 3.9. It can be seen that the each pipe moved along broadly parallel to the failure surface in each slope instability test. Furthermore, the magnitude of pipe movement decreases as the distance to the slope crest increases. Figure 3.10 illustrates the total movements of the pipes with respect to the footing vertical movement. Comparing the behaviour of P1, P2 and P3, the shallower pipes had relatively larger movements. P2 had the largest pipe displacement since it had the shallowest burial depth and the shallowest failure surface. The movements of P1 and P4 demonstrate a decreasing trend as the original location of the pipe moved towards the toe. The moving rate of P2 was slightly higher than that of the footing, while the moving rates of P1 and P4 after their corresponding failures were comparable with the footing settlement rate.

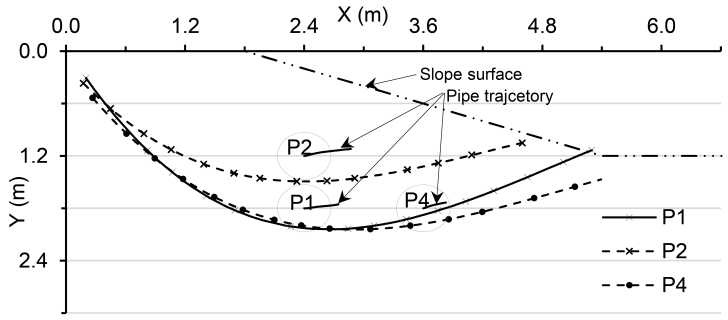

Figure 3.9: Trajectories of P1, P2 and P4

3.4.3. Cross section deformation of the pipes

The deformed shape of pipe cross section can be inferred from the measurements of the four strain gauges secured on the pipe as shown in Figure 3.3. All tests had the same pattern of strain development. Results of P1 are illustrated in Figure 3.11. The strain gauges reached their peak values at the same moment when the failure surface was fully generated.

The strain measurements before loading were subtracted from total strain measurements. Hence, the initial deformation due to the soil weight was excluded. The peak strain measurements of the pipes for different tests and the schematic deformed shape of the pipe are plotted in Figure 3.14. Based on the maximum pipe cross section strain measurements, it can be inferred that the pipe deformation of each test was symmetric since the peak values of the opposite strain gauges were almost identical (Figure 3.14a). The maximum average value of SG2 and SG3 as

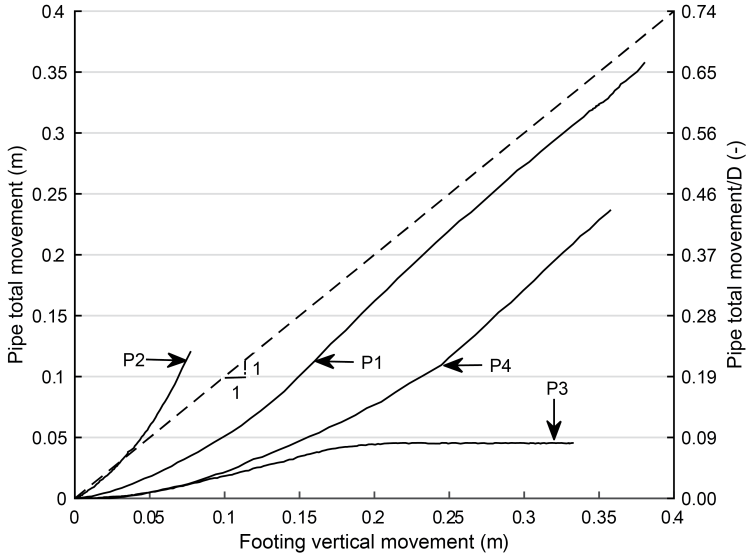

Figure 3.10: Total pipe movement with respect to footing vertical movement

well as that of SG1 and SG4 for each test are summarized in Table 3.4 and are used to calculate the external forces on the pipe in the following section.

Table 3.4: Estimated ultimate acting forces on the pipes and their respective directions

Test	$\frac{\varepsilon_{1,\max}+\varepsilon_{4,\max}}{2}$ ($\mu\varepsilon$)	$\frac{\varepsilon_{2,\max}+\varepsilon_{3,\max}}{2}$ ($\mu\varepsilon$)	The ultimate acting force, F_{uN} (kN/m)	F_{uN} direction, $\theta_u(^\circ)$
P1	-364.69	349.30	59.52	17.94
P2	-127.21	104.30	16.55	12.98
P3	-288.12	259.74	43.05	16.08
P4	-251.57	286.07	53.58	22.63
P5	-129.91	115.51	18.99	15.64
P1G	-372.13	374.60	65.47	19.39

3.4.4. External forces on the pipes

The external forces acting on the pipe during the soil movements can be simplified as a pair of dominant counterbalancing point forces (F_N) as depicted in Figure 3.14. The outer strain (ε) for an arbitrary point of the pipe with an angle of θ with respect to the direction of the counterbalancing point forces has the following relationship with the magnitude of the acting force F_N:

$$-\varepsilon = \frac{6F_N r}{Et^2}\left(\frac{1}{\pi} - \frac{|\sin\theta|}{2}\right) \tag{3.4}$$

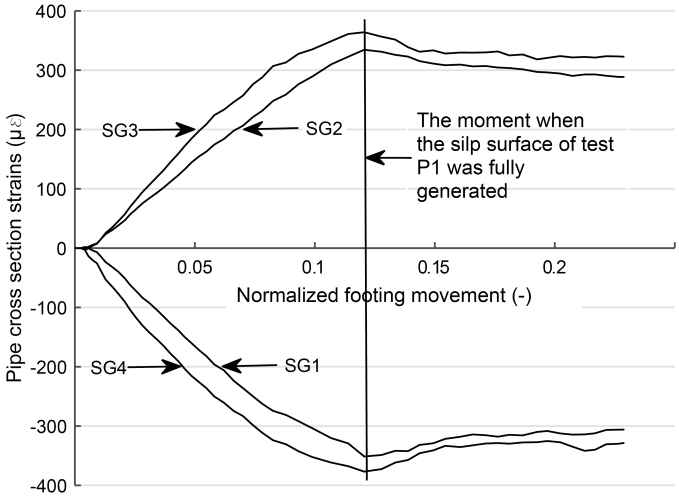

Figure 3.11: Development of the cross section strains of P1

where r is the outer radius, E is the Young's modulus of the pipe material and t is the wall thickness of the pipe. Note that F_{N} is in the unit of kN/m. Hence, the four cross section stain measurements (ε_i) can be expressed in Equation (3.5).

$$\begin{cases} -\varepsilon_3 = -\varepsilon_2 = \frac{6F_{\mathrm{N}}r}{Et^2}\left(\frac{1}{\pi} - \frac{\cos\theta}{2}\right) \\ -\varepsilon_1 = -\varepsilon_4 = \frac{6F_{\mathrm{N}}r}{Et^2}\left(\frac{1}{\pi} - \frac{\sin\theta}{2}\right) \end{cases} \tag{3.5}$$

By solving Equation (3.5) with the maximum strain measurements, $\varepsilon_{1,\max}$ and $\varepsilon_{3,\max}$, the ultimate values of point load and the direction, F_{uN} and θ_u can be determined from Equation (3.6) and Equation (3.7), respectively. Equation (3.6) has two answers, however, F_{uN} should be a positive value because the acting forces due to the slope instability should be compressing the pipe. The maximum acting forces and the respective directions with respect to horizontal are represented in Table 3.4. Note that, since the initial strains due to soil weight have been subtracted, F_{uN} in Table 3.4 was induced only by the slope failure.

$$F_{\mathrm{uN}} = -\frac{\pi E t^2}{3r} \frac{\varepsilon_{3,\max}^2 + \varepsilon_{1,\max}^2}{2\varepsilon_{1,\max} + 2\varepsilon_{3,\max} \pm \pi\sqrt{\varepsilon_{3,\max}^2 - \left(\frac{2}{\pi}(\varepsilon_{3,\max} - \varepsilon_{1,\max})\right)^2 + \varepsilon_{1,\max}^2}} \tag{3.6}$$

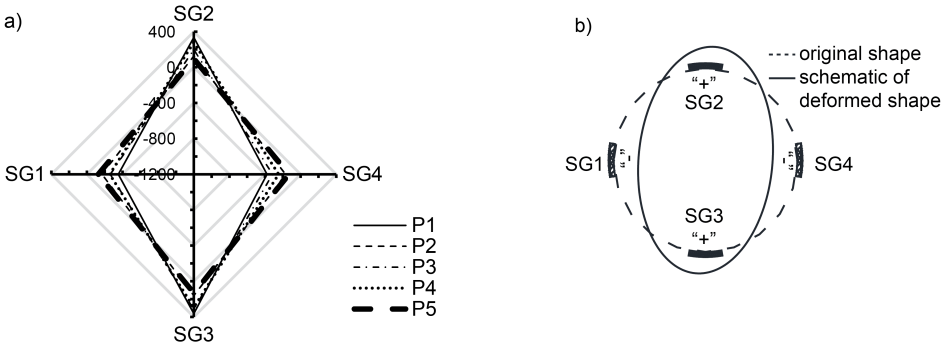

Note: positive value stands for extension

Figure 3.12: a) Maximum pipe strain measurements tests with DC Sand; b) Schematic deformation of the pipe cross section caused by the slope failure

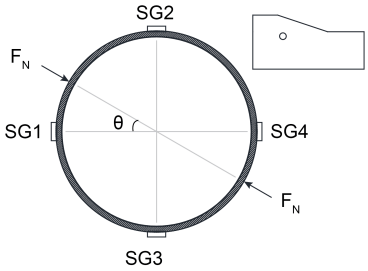

Figure 3.13: Simplified model of acting forces on a pipe embedded inside an unstable slope

$$\theta_u = \sin^{-1}\left(\frac{\frac{2}{\pi}(\varepsilon_{3,\max}-\varepsilon_{1,\max})\varepsilon_{3,\max} \mp \varepsilon_{1,\max}\sqrt{\varepsilon_{3,\max}^2-\left(\frac{2}{\pi}(\varepsilon_{1,\max}-\varepsilon_{3,\max})\right)^2+\varepsilon_{1,\max}^2}}{\varepsilon_{3,\max}^2+\varepsilon_{1,\max}^2}\right) \tag{3.7}$$

Audibert and Nyman (1977) found the normalized force-pipe movement relationships of their results were hyperbolic and were bounded by two curves. The normalized test results are compared with these two boundaries in Figure 3.14. The test results follow hyperbolic trend but are slightly below the lower boundary suggested by Audibert and Nyman (1977). This might be attributed to the difference between the two testing environments, i.e. level ground and sloping ground. The two constant values, a and b, in Equation (3.2) were obtained by fitting the test results. The average curve and corresponding function are shown in Figure 3.14. Only the results of tests P1, P2 and P4 are discussed here and after, because the pipes of other tests were not in the corresponding sliding zones.

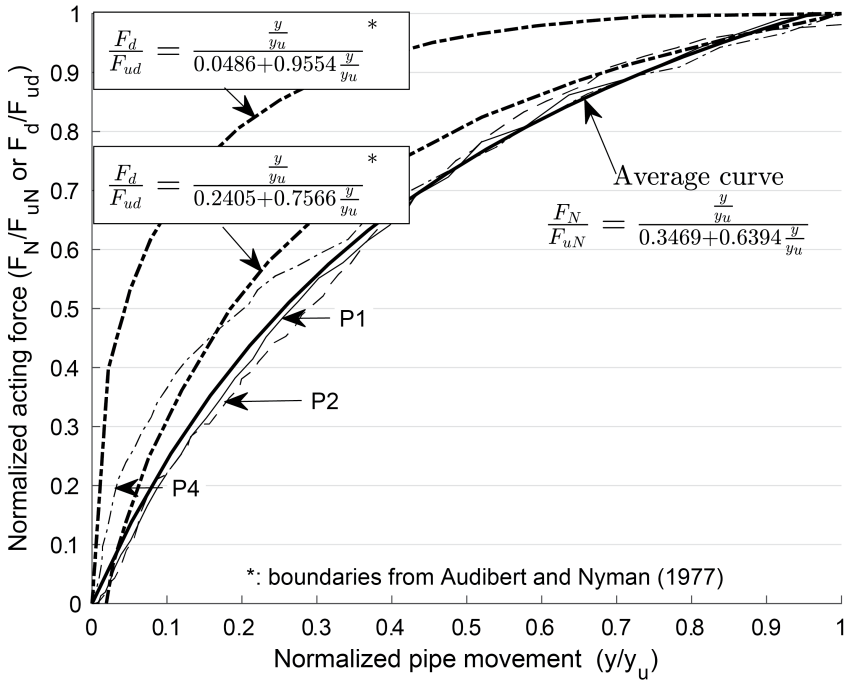

Figure 3.14: Normalized acting force vs. normalised pipe movement

The values of y_u/H_c are summarized in Table 3.5. The results of the tests P1 and P4 are in good agreement with the estimation by Trautmann et al. (1985) for medium dense sand. Nevertheless, y_u/H_c for test P2 is comparable with the estimation for loose sand.

Table 3.5: Ratios of ultimate pipe movements with respect to pipe embedment depths

	P1	P2	P3
y_u/H_c	0.09	0.12	0.08

3.5. Estimation of the ultimate acting forces on pipelines in slopes

The results of the centrifuge tests and the measurements of the load applied to the pipes are used in this chapter to derive a general formulation to determine the normal load applied to a pipe in an unstable slope. The maximum soil load acting on a pipe buried in a flat ground surface depends on the soil unit weight, pipe embedment depth and the ultimate bearing capacity factor which is a function of H_c/D and soil friction angle (Guo and Stolle, 2005, Trautmann et al., 1985). This

dependency is generally presented using Equation (3.1). However, the ultimate soil force acting on a pipe in the sloping ground condition (q_{us}) depends not only on the soil unit weight, pipe embedment depth and ultimate bearing capacity factor but also depends on the location of the pipe centre with respect to slope crest (L_c) as well as on the slope angle (β). The parameter L_c is specifically important for the case of a rotational slope failure mechanism. The effect of slope angle on the ultimate soil load on the pipe will be investigated in Section 3.5.1 and thereafter, a general equation is derived to account the impact of other factors on the load transferred from the moving soil to the pipe.

3.5.1. Effect of slope angle on the applied force to the pipe

Audibert and Nyman (1977) proposed Equation (3.1) for pipes buried under the flat ground condition; however, this equation cannot be directly applied to a pipe buried in a slope due to the geometric difference between the two ground surface conditions as shown in Figure 3.16. Line AO is the slope surface, line AC is the hypothetical level ground, and line BO has an inclination of $45° - \varphi'/2$ suggested by Hansen (1961), where φ' is the internal soil friction angle of the soil.

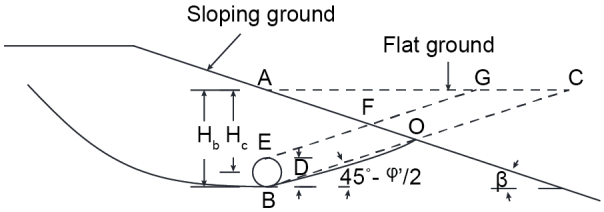

Figure 3.15: Slip surface of a slope with a buried pipe

In order to link the ultimate soil resistance for the sloping ground condition, q_{us}, with the ultimate soil resistance for the flat ground condition, q_u, a geometric factor α is introduced in this study. The factor α can also be regarded as the ultimate soil resistance ratio between the two ground surface conditions as expressed by Equation (3.8). The geometric factor α is approximated by the ratio between the areas of EBOF and EBCG, i.e. S_{EBOF}/S_{EBCG}, as shown in Equation (3.9), which is dependent on the soil friction angle and the slope angle.

$$q_{us} = \alpha q_u \tag{3.8}$$

$$\alpha = \frac{S_{EBOF}}{S_{EBCG}} = \frac{\tan(45° - \varphi'/2)}{\tan\beta + \tan(45° - \varphi'/2)} \tag{3.9}$$

It should be noted that during the process of slope failure, the pipe position and the slope surface (AO in Figure 3.16) are changing, however, these changes are assumed to be negligible at small soil strains.

3.5.2. Effect of buried depth and buried distance to the slope crest on the applied force to the pipe

Equation (3.10) is proposed to accommodate the dependencies of the burial depth (H_c) and the distance to the slope crest (L_c). The model parameter ω is a weight factor indicating the influence of H_c compared with the influence of L_c on q_{us}. Substituting Equation (3.1) and Equation (3.9) into Equation (3.10) yields the model parameter ω to be defined as demonstrated in Equation (3.11). When the pipe is buried under a flat surface, the geometric factor α is 1 (see Equation (3.9)) and yields ω to be 1, hence, Equation (3.10) reduces to Equation (3.1). In this study, the slope angle (β) is $18.4°$ and φ' is $33.6°$, hence, α equals to 0.62. The values of ω for P1, P2 and P4 can be obtained from Equation (3.11) and are listed in Table 3.6.

$$q_{us} = \gamma D \left(\frac{H_c}{D}\right)^{\omega} \left(\frac{D}{L_c}\right)^{(1-\omega)} N_{uq} \tag{3.10}$$

$$\omega = 1 + \frac{\ln \alpha}{\ln(L_c/D) + \ln(H_c/D)} \tag{3.11}$$

Table 3.6: Values of ω for tests P1, P2 and P4

	H_c (m)	L_c (m)	ω (-)
P1	1.6	0.6	0.594
P2	1.0	0.6	0.330
P4	1.2	1.8	0.759

The values of N_{uq} for tests P1, P2 and P4 are shown in Figure 3.16 with respect to the newly defined embedment ratio $\left((H_c/D)^{\omega}(D/L_c)^{(1-\omega)}\right)$. Results show a very good agreement with N_{uq} predicted by Ovesen (1964), Hansen (1961) and Hsu (1996).

Figure 3.17 illustrates N_{qs} versus normalized pipe movement for P1, P2 and P4. The results show that N_{qs} increased with the pipe movement and reached their ultimate values. After reaching peaks, N_{qs} fell down slightly (P1 and P4) or stayed constant (P2). It is also remarkable that a deeper sliding surface (see Figure 3.8) resulted in a higher stiffness for the normalized force-pipe movement curve. Furthermore, the development of N_{qs} with raising pipe movement generally follows the observations of Hsu (1996) as demonstrated in Figure 3.17 .

3.6. Application of Results

For illustrating the estimation of the ultimate soil load acting on a pipe, a sandy slope with the dimensions shown in Figure 3.18 is considered. Two scenarios of dry and fully submerged slopes are considered. The soil is composed of medium dense sand with a friction angle of $35°$, the dry and saturated unit weights are 18 and 20 kN/m^3, respectively. The sand layer is deposited above the bedrock layer in both cases. The slope instability is triggered by loading the slope crest. The

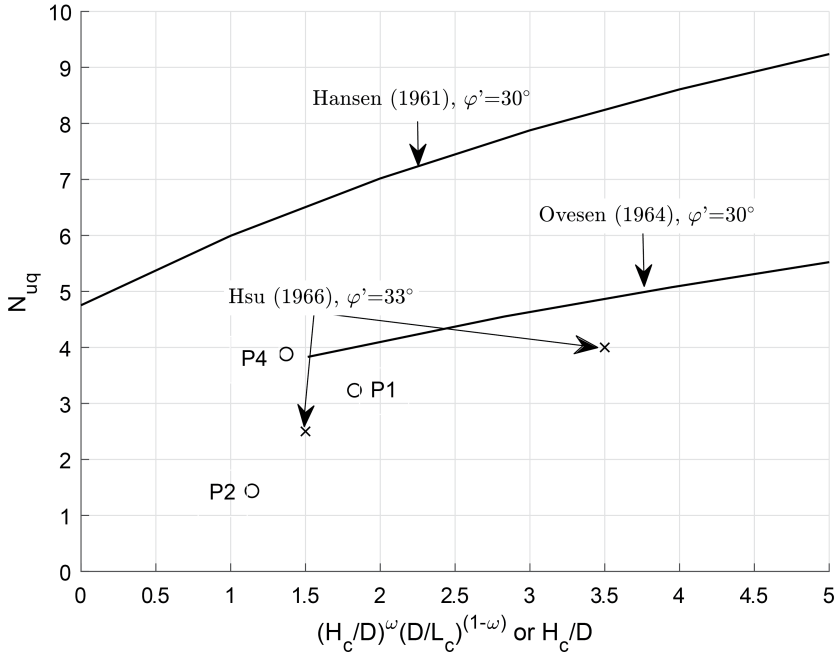

Figure 3.16: Comparison between measured and estimated N_{uqs} from two published methods

slope instability analysis is conducted based the Bishop's method of slices Bishop and Morgenstern (1960) using D-Geo Stability software (version 16.2), and gives a potential failure surface as illustrated in Figure 3.18.

A 1.0 m-diameter gas pipe is buried in the slope above the potential failure surface as illustrated in Figure 3.18. The ultimate soil load applied to the pipe can be calculated using the following steps:

- Step 1: Calculation of the geometric factor α. Equation (3.9) leads to a value of 0.589 for α when $\beta = 20°$ and $\varphi' = 35°$.
- Step 2: Calculation of parameter ω from Equation (3.11). H_c / D is 2.5 and L_c / D is 21.1 and these parameters result ω to be 0.867.
- Step 3: Calculation of the value N_{uq} from the method proposed by Ovesen (1964) based on the newly defined embedment ratio ($((H_c/D)^{\omega}(D/L_c)^{(1-\omega)}$=1.5). Figure 3.19 shows N_{uq} from the method of Ovesen (1964) which is applicable for both dry and saturated conditions. Hence, a value of 4.8 is selected for N_{uq} as indicated in Figure 3.19.
- Step 4: Calculation of q_{us}. The values of ultimate soil load on the pipe in two scenarios of dry and submarine slopes are calculated using Equation (3.10).

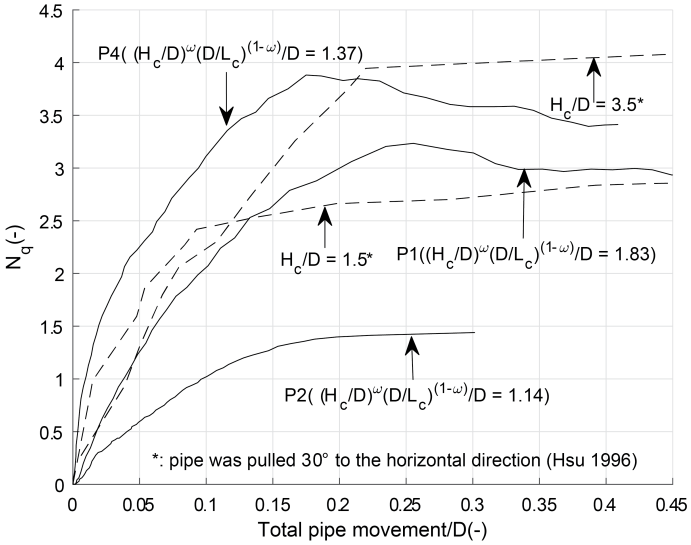

Figure 3.17: Development of dimensionless force on pipe with pipe movement

q_{us} = 127.2 kPa and q_{us} = 70.7 kPa are obtained for the dry and submerged slopes, respectively.

3.7. Summary and Conclusions

In this paper, the behaviour of buried pipes in unstable sandy slopes was studied by means of centrifuge modelling. The magnitudes of the slope failure-induced external forces on the pipes were investigated and the interactive influence of the pipes on the development of the failure surfaces were discussed. The forces acting on the pipes buried in sloping grounds were compared with published results based on the tests on pipes under flat surfaces. Moreover, the effect of the pipe burial distance to the slope crest on the bearing capacity factor was illustrated. In addition, a geometric factor was introduced to modify the bearing capacity factor suggested for pipes buried in flat surfaces. The following conclusions are made based on the conditions that the embedment ratio of a pipe is less than or equal to 4.1 in a sandy sloping ground subjected to surcharge loading:

1. Pipes buried within the potential failure zones of the slopes suffer larger movements than those buried outside the potential failure surfaces. The potential failure surface can be estimated using analytical or numerical methods, such as the Limit Equilibrium or Finite Element Methods in the process of the design or evaluating a segment of a pipeline in a slope cross section.

2. The failure surface tends to pass below the pipe when it is placed no more than $0.5D$ below the potential slip surface.

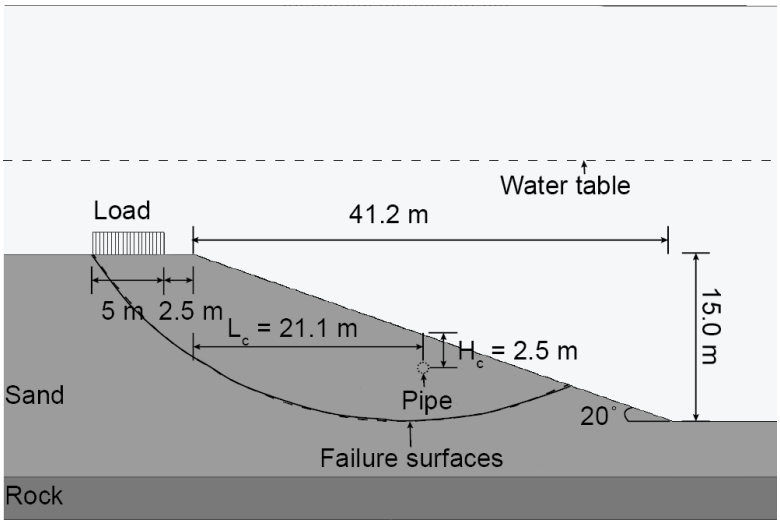

Figure 3.18: A case study of slope instability

3. The bearing capacity factors for pipes buried in slopes should be dependent on not only soil unit weight, pipe diameter and burial depth but also the slope angle and the pipe burial distance to the slope crest.

4. The normalized force-pipe displacement relationship could be represented by a hyperbolic equation.

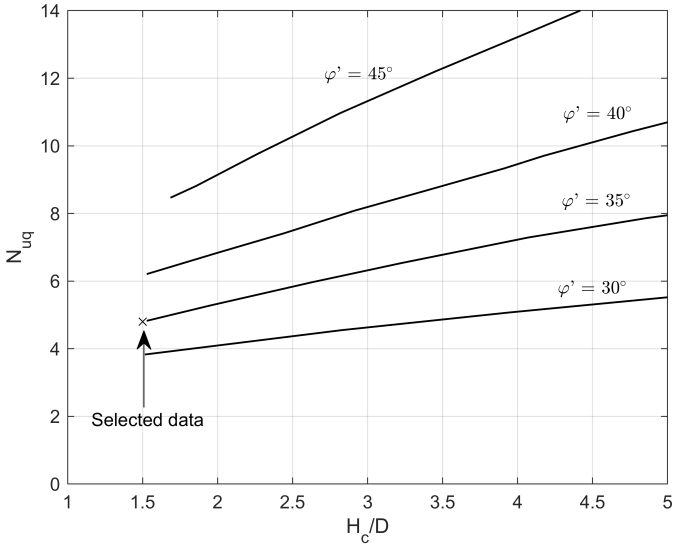

Figure 3.19: Plot of N_{uq} versus H_{c}/D modified from Ovesen (1964)

The maximum external force exerting on the pipe due to any circular failure mechanism of the slope can be predicted based on the method presented in this study. For the condition that the pipe is not located inside the failure zone, the proposed method for estimating the ultimate dimensionless force is invalid. However, in this case, the centrifuge test results of this study indicate that there is no necessity to consider the maximum pipe external forces induced by a landslide, as the pipe will be hardly influenced. Nevertheless, further investigations with other slope angles and more pipe positions are necessary to validate the proposed method.

List of Symbols

Symbol	Definition
PFS	potential failure surface
DC Sand	Merwede river sand is also called Delft Centrifuge Sand
FS	failure surface
NP, NPG	tests without a pipe for the DC Sand sample and Geba Sand sample, respectively
P1G	Geba Sand sample with a pipe placed at the deepest location of its corresponding potential failure surface
Pi	pipe at different locations (i is from 1 to 5) for the DC Sand samples
PIV	Particle Image Velocimetry
SGi	strain gauges (i is from 1 to 4)
a, b	factor for normalized drag force and pipe movement relationship
g	Earth's gravity
q_{u}	ultimate soil resistance
q_{us}	ultimate soil resistance for the sloping ground condition
r	pipe outer radius
t	pipe wall thickness
y	Pipe movement
y_{u}	pipe movement at the ultimate soil resistance
Δy_{f}	settlement of the footing
B	the width of the anchor slab
B_{f}	width of the footing
D	pipe outer diameter
D_{10}, D_{30}, D_{50}, D_{60}	maximum size of the smallest 10%, 30%, 50% and 60% of the sample, respectively
Dr	relative density
E	young's modulus
EI	pipe flexural rigidity
F_{d}	drag force
F_{N}	counterbalancing point forces
F_{ud}	the ultimate drag force
F_{uN}	the ultimate counterbalancing point forces
G_{s}	specific gravity
H_{b}	depth from the soil surface to the invert of the pipe
H_{c}	depth from the soil surface to the centre of the pipe
I	the second moment of area per unit length for a longitudinal section
L	pipe length
L_{c}	distance between the pipe centre and the slope crest
N	scaling factor
N_{q}	bearing capacity factor or dimensionless force
N_{qs}	bearing capacity factor for the sloping ground condition

Symbol	Definition
N_{uq}	the ultimate bearing capacity factor
X, Y	Cartesian coordinate
α	geometric factor
β	slope angle
γ	soil unit weight
ε	pipe cross section outer strain
ε_i	strain measurements for strain gauges (i is from 1 to 4)
$\varepsilon_{i,max}$	maximum strain measurements for strain gauges (i is from 1 to 4)
θ	angle with respect to the direction of the counterbalancing point forces
θ_u	F_{uN} direction with respect to the horizontal plan
ξ	normalized foundation settlement (the footing settlement / the footing width)
φ'	internal soil friction angle
ω	weight factor indicating the influence of the pipe burial depth compared to the distance between the pipe centre to the slope crest on the bearing capacity factor

References

Allersma, H. (1994). The university of delft geotechnical centrifuge. In *International conference centrifuge 94*, pages 47–52.

Almahakeri, M., Fam, A., and Moore, I. D. (2013). Experimental investigation of longitudinal bending of buried steel pipes pulled through dense sand. *Journal of Pipeline Systems Engineering and Practice*, 5(2):04013014.

Askarinejad, A., Beck, A., and Springman, S. M. (2015). Scaling law of static liquefaction mechanism in geocentrifuge and corresponding hydromechanical characterization of an unsaturated silty sand having a viscous pore fluid. *Canadian Geotechnical Journal*, 52(6):708–720.

Askarinejad, A., Sitanggang, A. P. B., and Schenkeveld, F. (2017). Effect of pore fluid on the behavior of laterally loaded offshore piles modelled in centrifuge. In *19th International Conference on Soil Mechanics and Geotechnical Engineering (ICSMGE 2017), Seoul, Korea*, pages 897–900.

Audibert, J. M. and Nyman, K. J. (1977). Soil restraint against horizontal motion of pipes. *Journal of the Geotechnical Engineering Division*, 103(10):1119–1142.

Bishop, A. W. and Morgenstern, N. (1960). Stability coefficients for earth slopes. *Geotechnique*, 10(4):129–153.

Calvetti, F., Di Prisco, C., and Nova, R. (2004). Experimental and numerical analysis of soil–pipe interaction. *Journal of geotechnical and geoenvironmental engineering*, 130(12):1292–1299.

Chan, P. D. S. and Wong, R. C. K. (2004). Performance evaluation of a buried steel pipe in a moving slope: a case study. *Canadian geotechnical journal*, 41(5):894–907.

De Jager, R. R., Maghsoudloo, A., Askarinejad, A., and Molenkamp, F. (2017). Preliminary results of instrumented laboratory flow slides. *Procedia Engineering*, 175:212–219.

Di Prisco, C. and Galli, A. (2006). Soil-pipe interaction under monotonic and cyclic loads: experimental and numerical modelling. In *Proceedings of the First Euromediterranean Symposium on Advances in Geomaterials and Structures, Hammamet, Tunisia*, pages 3–5.

Feng, W., Huang, R., Liu, J., Xu, X., and Luo, M. (2015). Large-scale field trial to explore landslide and pipeline interaction. *Soils and Foundations*, 55(6):1466–1473.

Folga, S. (2007). Natural gas pipeline technology overview. Technical report, Argonne National Lab.(ANL), Argonne, IL (United States).

Garnier, J., Gaudin, C., Springman, S. M., Culligan, P., Goodings, D., Konig, D., Kutter, B., Phillips, R., Randolph, M., and Thorel, L. (2007). Catalogue of scaling laws and similitude questions in geotechnical centrifuge modelling. *International Journal of Physical Modelling in Geotechnics*, 7(3):1–23.

Guo, P. and Stolle, D. (2005). Lateral pipe–soil interaction in sand with reference to scale effect. *Journal of geotechnical and geoenvironmental engineering*, 131(3):338–349.

Hansen, J. B. (1961). The ultimate resistance of rigid piles against transversal forces. *Bulletin 12, Danish Geotech. Institute*, pages 1–9.

Hsu, T.-W. (1996). Soil restraint against oblique motion of pipelines in sand. *Canadian geotechnical journal*, 33(1):180–188.

Liu, R., Guo, S., and Yan, S. (2015). Study on the lateral soil resistance acting on the buried pipeline. *Journal of Coastal Research*, 73(sp1):391–398.

Maghsoudloo, A., Galavi, V., Hicks, M. A., and Askarinejad, A. (2017). Finite element simulation of static liquefaction of submerged sand slopes using a multilaminate model. In *19th International Conference on Soil Mechanics and Geotechnical Engineering*, volume 2, pages 801–804.

Nyman, K. J. (1984). Soil response against oblique motion of pipes. *Journal of Transportation Engineering*, 110(2):190–202.

Oliveira, J. R., Almeida, M. S., Almeida, M. C., and Borges, R. G. (2009). Physical modeling of lateral clay-pipe interaction. *Journal of geotechnical and geoenvironmental engineering*, 136(7):950–956.

Oliveira, J. R. M., Rammah, K. I., Trejo, P. C., Almeida, M. S., and Almeida, M. C. (2017). Modelling of a pipeline subjected to soil mass movements. *International Journal of Physical Modelling in Geotechnics*, 17(4):246–256.

Ono, K., Yokota, Y., Sawada, Y., and Kawabata, T. (2017). Lateral force–displacement prediction for buried pipe under different effective stress condition. *International Journal of Geotechnical Engineering*, pages 1–9.

Ovesen, N. K. (1964). Anchor slabs, calculation methods and model tests. *Bulletin*, 16:39.

Ovesen, N. K. (1981). Centrifuge tests of uplift capacity of anchors. In *Proc. 10th. Int. Conf. on SMEE*, volume 1, pages 717–722.

Paulin, M. J. (1998). *An investigation into pipelines subjected to lateral soil loading*. Doctoral dissertation, Memorial University of Newfoundland.

Pozo, C., Gng, Z., and Askarinejad, A. (2016). Evaluation of soft boundary effects (sbe) on the behaviour of a shallow foundation. In *3rd European Conference on Physical Modelling in Geotechnics (EUROFUGE 2016)*, pages 385–390.

Presti, D. C. L., Pedroni, S., and Crippa, V. (1992). Maximum dry density of cohesionless soils by pluviation and by astm d 4253-83: a comparative study. *Geotechnical Testing Journal*, 15(2):180–189.

Rammah, K. I., Oliveira, J. R., Almeida, M. C., Almeida, M. S., and Borges, R. G. (2014). Centrifuge modelling of a buried pipeline below an embankment. *International Journal of Physical Modelling in Geotechnics*, 14(4):116–127.

Roy, K. S. and Hawlader, B. (2012). Soil restraint against lateral and oblique motion of pipes buried in dense sand. In *International Pipeline Conference*, volume 45158, pages 7–12. American Society of Mechanical Engineers.

Sahdi, F., Gaudin, C., White, D., Boylan, N., and Randolph, M. (2014). Centrifuge modelling of active slide-pipeline loading in soft clay. *Géotechnique*, 64(1):16–27.

Schofield, A. N. (1980). Cambridge geotechnical centrifuge operations. *Geotechnique*, 30(3):227–268.

Stanier, S. A., Blaber, J., Take, W. A., and White, D. (2015). Improved image-based deformation measurement for geotechnical applications. *Canadian Geotechnical Journal*, 53(5):727–739.

Taylor, R. (1995). *Geotechnical centrifuge technology*. Blackie Academic & Professional, Chapman & Hall, London.

Terzaghi, K. (1943). *Theoretical Soil Mechanics*. John Wiley & Sons.

Tian, Y. and Cassidy, M. J. (2011). Pipe-soil interaction model incorporating large lateral displacements in calcareous sand. *Journal of Geotechnical and Geoenvironmental Engineering*, 137(3):279–287.

Trautmann, C. H., O'Rourfce, T. D., and Kulhawy, F. H. (1985). Uplift force-displacement response of buried pipe. *Journal of Geotechnical Engineering*, 111(9):1061–1076.

White, D., Take, W., and Bolton, M. (2003). Soil deformation measurement using particle image velocimetry (piv) and photogrammetry. *Geotechnique*, 53(7):619–631.

Wood, D. M. (2014). *Geotechnical modelling*. CRC Press.

Wu, J., Zhou, R., Xu, S., and Wu, Z. (2017). Probabilistic analysis of natural gas pipeline network accident based on bayesian network. *Journal of Loss Prevention in the Process Industries*, 46:126–136.

Yimsiri, S., Soga, K., Yoshizaki, K., Dasari, G., and O' Rourke, T. (2004). Lateral and upward soil-pipeline interactions in sand for deep embedment conditions. *Journal of geotechnical and geoenvironmental engineering*, 130(8):830–842.

Zhang, J., Stewart, D. P., and Randolph, M. F. (2002). Modeling of shallowly embedded offshore pipelines in calcareous sand. *Journal of geotechnical and geoenvironmental engineering*, 128(5):363–371.

Zhang, W. and Askarinejad, A. (2019). Behaviour of buried pipes in unstable sandy slopes. *Landslides*, 16(2):283–293.

4

Centrifuge modelling of submarine landslides due to static liquefaction

子曰：“学而不思则罔，思而不学则殆。”

《论语. 为政篇》

Confucius said, “It throws one into bewilderment to read without thinking whereas it places one in jeopardy to think without reading.”

Analects of Confucius

The content of this chapter has been accepted as research paper in Landslides, Zhang and Askarinejad (2019).

4.1. Abstract

Sand erosion and scouring caused by waves and marine currents result in gradual increase of local seabed inclination and formation of slopes around hydraulic structures and offshore foundations. During this process, shear stresses in the soil body increase statically, which may lead to static liquefaction and damage of the adjacent offshore infrastructure. This paper presents the details of a newly developed static liquefaction triggering actuator to be used at an enhanced gravity condition in a geotechnical centrifuge. This actuator simulates the steepening process of submarine sand layers due to scouring and enables the investigation of failure mechanisms in submerged slopes. The details of the centrifuge test setup designed and constructed to simulate the process of triggering static liquefaction in loose sand layers are presented. Furthermore, the performance of the novel integrated model preparation facility using the sand fluidization technique is explained. The setup was used to conduct several centrifuge tests at four different slope steepening rates to investigate the slope steepening rate effects. Moreover, the effect of viscosity of the submerging pore fluid on the behaviour of the slopes at the onset of failure is investigated. The Coriolis effect on loose saturated sand samples during increasing of g-level is examined also. Results show that the built-up of pore pressure due to local shear deformations can be detected and considered as one of the triggering mechanisms of this kind of submarine slope instabilities.

Key words*: Submarine landslides, Static liquefaction, Centrifuge modelling, Offshore foundations*

4.2. Introduction

The failure of natural or man-made slopes under water is one of the main threats to offshore assets. Liquefied submerged slopes or embankments are often characterised by relatively small failure angle, sudden failure, a considerable amount of released soil mass and large influencing areas (Kvalstad et al., 2001). These make static liquefaction to be one of the most catastrophic mechanisms of underwater slope failures. Instability of these slopes can be triggered by static loads, such as sediments deposition, toe erosion, rising of an embankment height, scour near a structure or dredging activities (De Jager et al., 2017, Kvalstad et al., 2001, Maghsoudloo et al., 2017, Sadrekarimi, 2016, Wanatowski and Chu, 2012). Several cases of static liquefaction of submarine slopes and flow slides have been reported in the literature (Andresen and Bjerrum, 1968, Bjerrum, 1971, Kraft Jr et al., 1992, Kramer, 1988, Sladen et al., 1985). Numerous submerged slope instabilities have occurred in Zeeland, the Netherlands, over the past 200 years which were major threats for the flood defence systems (Silvis and Groot, 1995). Take the case of the Eastern Scheldt storm surge barrier as example (Silvis and Groot, 1995), due to waves and currents scouring happens near the structure as illustrated in Figure 4.1, which schematically shows the development of a scour hole. During the scouring process, the slope inclination increases before reaching a stable condition, which results in a change of stress state, leading to an unstable stress path and liquefaction, as shown in Figure 4.1b. Before the scouring occurs, the stress state of the soil element in Figure 4.1a is indicated as point A which lies on the K_0 line, where K_0 is the ratio of effective horizontal stress to effective vertical stress at rest. Then, as the scour hole develops and seabed slope angle (θ) rises gradually, mean effective stress (p') decreases while the deviator stress (q) increases monotonically under a drained condition. Hence the stress state constantly shifts to the upper left in the $p' - q$ space. At a certain point, due to collapse of voids in the soil structure, instability under undrained conditions would be triggered when the stress path hits the instability line (IL) at point B. As a result, excess pore pressure would be generated and the sand would lose its strength suddenly which is expressed as line BC which lies in between IL and the critical state line (CSL). Full liquefaction happens at point C. Therefore, understanding of soil behaviour and excess pore pressure generation during the increasing of slope inclination is necessary in assessing the failure mechanism of static load induced liquefaction for marine slopes.

Static liquefaction can occur in a loosely packed sand element under a slight change in the static load, due to the successive micro-collapses of the voids resulting in the build-up of pore water pressure in a temporarily undrained condition (Askarinejad et al., 2015, Lade, 1992, Lade and Yamamuro, 2011, Sladen et al., 1985, Take et al., 2004). Physical modelling techniques (large-/small-scaled models and centrifuge tests) have been applied to study under-water landslide failure behaviour, as they have the advantage of evaluating some specific features of prototypes (Wood, 2014). In many large-/small-scaled tests ($1g$ tests) the "releasing gate" method was adopted as the slope failure triggering mechanism to investigate the landslide post failure behaviour. For example, De Groot et al. (2012) and De Jager (2018) summarized a series of static liquefaction experiments in large

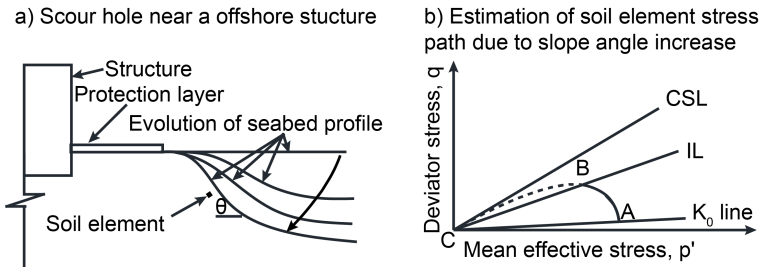

Figure 4.1: Schematic view of development of seabed inclination due to scouring and resultant effective stress path

and medium sized flumes. In the large flume, the valid length of samples was 24 m and the height varied from 1.0 to 2.1 m. The samples were kept in position by a rotatable gate, which would be lifted with a speed of around 0.1 m/sec during the tests. In their medium sized flume, samples' lengths were about 5.0 m and 10.0 m for coarse sand and fine sand, respectively, and their heights were around 0.63 m. By means of dredging, these samples were made with steep slope angles which were kept stable by applying suction from the base. Failures were induced by releasing the suction. Sudden development of excess pore pressures was observed at the onset of slope instabilities in these tests. Spence and Guymer (1997) adopted a similar idea to trigger flow slides. Samples were made on an inclined tank and were kept stable by a watertight barrier before testing. Flow slides were triggered by quickly removing the barrier. A retrogressive non-circular slipping behaviour of flow side motion was observed. Ilstad et al. (2004) studied subaqueous debris flows in a 10-m long tank. The clay-sand mixture was stored in a reservoir which was hanging above a 6° rough bed. By releasing the gate of the reservoir, debris could flow down along the bed during which the pore pressure evolution was recorded.

Similarly, Yamada et al. (2010) conducted several sandbox experiments using dry sand to study submarine landslides triggered by slope steepening due to tectonic deformation. However, this test model is unable to consider the build-up of pore water pressure. Alternatively, Byrne et al. (2000) built an 8-m high clay embankment with a slope angle of 21.8° over a loose saturated sand layer in the field as part of the Canadian Liquefaction Experiment project. The intent of this field test was to trigger liquefaction in the loose sand layer by applying static load rapidly, however, the embankment was stable during the event. They concluded that the direction of loading, which controls the soil residual strength, and the drainage conditions governed the stability of the base sand layer. De Jager (2018) designed a large scale $1g$ Liquefaction Tank at TU Delft with the main purpose of investigating slope over-steepening effects on under-water liquefaction. Submerged fine sand samples were prepared flat initially and then were triggered to failure by lifting up one side of the $1g$ Liquefaction Tank constantly and slowly. They found that slope failure is governed by the looser part of the sample and tilting rate (TR) affects slope instability. However, the maximum sand layer height is 1.5 m, and the max-

imum tilting angle is 10° in this facility. The application of $1g$ tests' results to field situation is restricted by the model scale effects.

Simulation of in situ stress conditions is vital for assessment of soil strength, soil resistance to liquefaction and pore pressure conditions (Kvalstad et al., 2001, Schofield, 1980). Centrifuge techniques have the advantage of preserving the stress condition in the field in a small-scaled model at a high centrifugal acceleration condition and have been widely applied in geotechnical engineering. The "releasing gate" method, adopted in the $1g$ tests performed by De Groot et al. (2012), De Groot et al. (2019), Spence and Guymer (1997) and Ilstad et al. (2004), has been applied into centrifuge modelling for studying the landslide flow behaviour as well (e.g. Acosta et al., 2017, Boylan et al., 2009, Gue et al., 2010, Yin et al., 2017). However, only clay/slurry materials have been used in these models. It has been acknowledged that the application of the "releasing gate" method is capable of providing useful information about flow slide behaviour, which is assumed to be independent of initiation method (Spence and Guymer, 1997).

However, knowing the potential triggering mechanisms of marine landslides is of crucial importance in order to reduce the chance of seabed liquefaction during construction and the whole lifetime of offshore structures, such as pipelines, wind turbine foundations and barriers. Several marine landslides triggering mechanisms were investigated in centrifuge, such as earthquake induced landslides (e.g. Coulter and Phillips, 2003, Elgamal et al., 2005) and wave induced landslides (e.g. Sassa and Sekiguchi, 1999). However, only a few centrifuge experiments have been conducted on fully saturated soil under a static loading condition. One of the first reported static liquefaction tests conducted in a centrifuge was done by Phillips and Byrne (1995). As a result of dropping a surcharge above the slope crest, liquefaction was induced and the slope angle changed from 16° to 7° after failure. Zhang et al. (2015) studied the generation of high pore pressure in gentle submarine slopes. Samples were composed of a layer of kaolin clay on the top and a thin sand layer below. Slope failures were triggered in flight by injecting pore fluid into the sand layer from the embedded perforated pipes. Accumulation of pore pressure was observed before the major failure. Zhang et al. (2015) used saline water to simulate seawater, whereas the scaling effect of pore fluid viscosity was not considered. Based on literature study, effects of the increasing of submarine slope inclination on the slope instability have not been studied in centrifuge yet.

The objective of this paper is to introduce a new geotechnical centrifuge testing facility which is designed to investigate the static liquefaction mechanism in submarine sandy slopes. Due to the special requirements for conducting centrifuge tests on very loose saturated sand samples, a new strongbox equipped with a fluidization system was developed. In this paper, the details of the testing facility are presented. Furthermore, the sample properties, such as uniformity, distribution of relative density and degree of saturation across the sample are discussed. Besides, the development of excess pore pressure inside the soil layer prior to and post failure are analysed.

4.3. Sample preparation

Sample preparation methods affect soil structure, saturation, uniformity and relative density and therefore have a major influence on the sample behaviour (Della et al., 2011, Vaid et al., 1999). Kramer (1988) compared several historical liquefaction flow slides happened in coastal areas, such as the slow slides occurred in Orkdalsfjord of Norway in 1930, and found that the natural deposit materials are similar in these areas which are described as silty fine sand or loose fine sand. Modelling the depositional process is essential for resembling prototype soil structure and for the assessment of the generation of excess pore pressure (Kvalstad et al., 2001). Therefore, the sample prepared for the physical modelling should have similar properties to that in the field for simulating slope static liquefaction. Furthermore, a special design is required for transporting the sample from the preparation area to the carrier of the geo-centrifuge. Since a small disturbance could cause sample densification. In this section, we discuss about the various conventional sample preparation methods and explain the details of a strongbox designed for making samples as well as the soil and pore fluid material used in this study.

4.3.1. Background

Coulter and Phillips (2003) prepared fully saturated sand samples for studying earthquake effects on soil liquefaction in centrifuge. Sand samples with relative densities (Dr) of 38% - 42% were made by a combination of air pluviation technique, sample saturation technique (using vacuum and carbon dioxide) and pore fluid replacing technique. Rietdijk et al. (2010) developed the drizzle method for creating saturated samples with Dr around 5%. However, such a loose sample would be densified in the process of sample transportation. Askarinejad et al. (2018) adopted the water pluviation method and successfully prepared saturated slopes with relative density of 15%. However, this technique was reported to be extremely time consuming, i.e. approximately 8 hours were required to construct a sample in a strongbox with dimensions of 270 mm x 150 mm x 135 mm.

Fluidization technique has been applied in physical modelling as the sample preparation technique to simulate the formation of a seabed/riverbed in coastal areas (De Groot et al., 2012, De Jager, 2018, Spence and Guymer, 1997). The fluidization technique has the following three advantages: i. the sample properties are reproducible; ii. the uniformity of samples can be guaranteed; iii. the achieved average relative density can be as low as that of the prototype. Spence and Guymer (1997) got loose samples with Dr less than 31% by fluidizing sand around 30 mins. De Groot et al. (2012) reported that the relative density was discharge-related. The $1g$ Liquefaction Tank at TU Delft (De Jager, 2018) is equipped with a fluidization system at the base which is composed of a filter and perforated pipes. Samples with relative densities ranging from 28% to 58% were made by adjusting the discharge of the fluidization system.

4.3.2. Fluidization system

A strongbox was constructed for the beam centrifuge at TU Delft with a U-shaped aluminium frame and two transparent side walls made of Plexiglass. The dimensions of the strongbox were designed to take advantage of the space in the centrifuge carrier. Samples with a length of 355 mm, a width of 134 mm and height of up to 110 mm, at model scale, can be prepared (Figure 4.2). The pore pressure developments in the soil layer can be monitored by three pore pressure transducers (PPTs, MPXH6400A) during both sample preparation and testing.

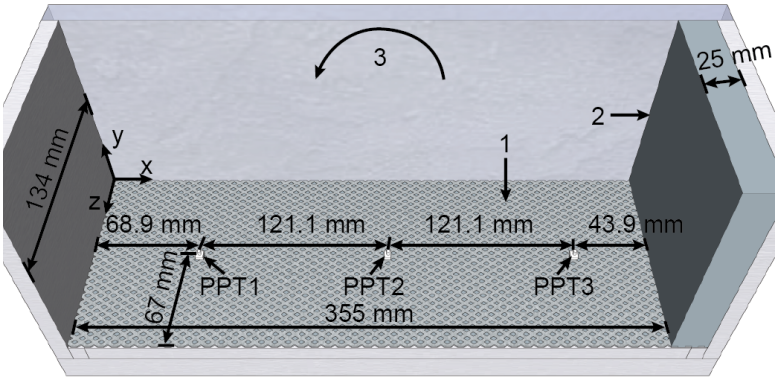

Figure 4.2: Fluidization system (outside view, model scale): 1) filter layer; 2) PVC block; 3) tilting direction

A fluidization system was integrated to the base of the strongbox. It is composed of three parts, a filter layer (Figure 4.3), a network of perforated pipes system (Figure 4.4) and a pump. The filter layer is sandwiched between the sand (on top) and the perforated pipes system (at the bottom). The filter layer has two main functions: i. to prevent sand particles from blocking the perforated pipes system, and, ii. to allow a smooth and uniform flushing of external fluid into the sand layer. Moreover, the filter layer was designed to be rigid enough to resist the deformation which might be caused by the sand weight during centrifuge spinning. The filter is made up of three mesh layers, a top mesh which is a fine square hole perforated stainless steel mesh, a bottom mesh which is a coarse round hole perforated stainless steel mesh, and a middle mesh which is a fine Nylon mesh filter (Figure 4.3). The bottom mesh has an opening size of 3 mm and a thickness of 1 mm, and it is seen as the backbone of the filter layer; the pore size of the Nylon mesh filter is 41 micro-meters which is chosen to be smaller than D_{10} of Geba Sand (Table 4.1); the top mesh has an opening size of 0.5 mm and a thickness of 0.5 mm which functions as the protection layer for the Nylon mesh filter. The filter layer was fixed onto a 6-mm thick aluminium frame (Figure 4.4), which was mounted on the base of the strongbox through screws; besides, it was supported by four 3-mm thick and evenly distributed PVC sticks as well. The PVC sticks were also used to secure the perforated pipes. A sealing rubber belt was placed in between the filter layer and the aluminium frame for preventing leakage along the boundaries of the

filter layer (Figure 4.3).

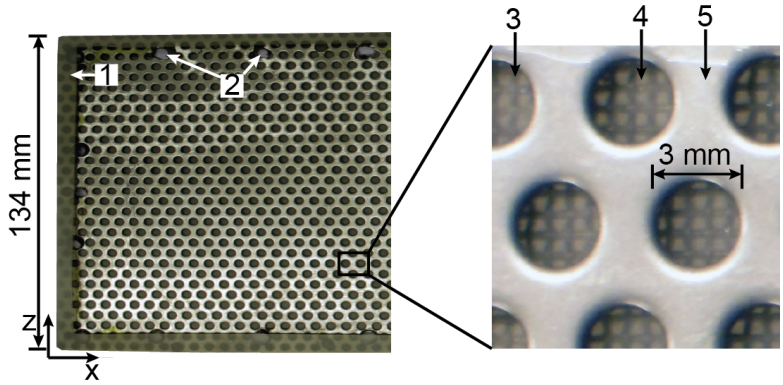

Figure 4.3: Filter layer of fluidization system (model scale): 1) sealing rubber; 2) screw holes; 3) top mesh; 4) middle filter; 5) bottom mesh

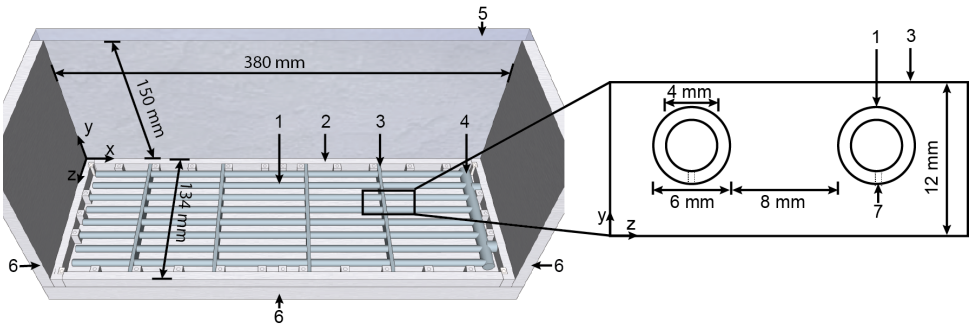

Figure 4.4: Fluidization system (inside view, model scale): 1) parallel pipes; 2) aluminium frame; 3) PVC sticks; 4) transverse pipe; 5) Plexiglas; 6) U-shape frame; 7) openings with diameter of 0.5 mm

The perforated pipe system is composed of eight parallel pipes with outer diameter of D_o = 6 mm and inner diameter of D_i = 4 mm which are connected to a transverse pipe with D_o = 12 mm and D_i = 10 mm (Figure 4.4). Fifty openings with diameter of 0.5 mm are evenly distributed along each small pipe. Based on experience of the construction of the $1g$ Liquefaction Tank (De Jager, 2018), a uniform sand sample requires a uniform fluid pressure in the fluidization system. Considering that the outflow will generate a pressure gradient along each perforated pipe, the rule that the area of outlet should be smaller than or equal to the inlet area is guaranteed, e.g. the total area of the fifty openings on one perforated pipe is smaller than the inner area of the pipe, thus the pressure difference in the pipe remains relatively small. The existence of the fine Nylon mesh filter may further smooth the fluid pressure specially within the fluidization system. Moreover, these openings are designed to be facing downwards (Figure 4.4). This design is assumed

to be useful to improve the uniformity of the fluid pressure below the fluidization filter.

Two inlet valves were connected to the transverse pipe from outside of the strongbox (see further in Figure 4.11). These valves were open during the fluidization and closed during the centrifuge tests. Because there are no openings on the transverse pipe, less discharge would be expected in the zone above the transverse pipe which may cause sample non-uniformity. Therefore, a PVC block was fixed onto the filter layer above the area of the transverse pipe (Figure 4.2). The submerging fluid height from the sample bottom was 180 mm (model scale) for all tests. A modular four-sided "extension box" on top of the strongbox provides enough space for the submerging fluid and generated waves after the landslides (see further in Figure 4.11).

A Grundfos PO07 water pump was used to fluidize the sand. One side of the pump was connected to the two valves (Figure 4.11) and the other side was connected to a container filled with de-aired fluid. A third valve was installed in a tube connecting the pump and the strongbox for controlling the discharge. The minimum fluid velocity for fluidizing the sample (V_{mf}) can be estimated based on Equation 4.1 proposed by Lowe (1976),

$$V_{\mathrm{mf}} = -\frac{150\alpha_2\mu_{\mathrm{f}}}{3.5\alpha_1 D_{\mathrm{particle}}\rho_{\mathrm{f}}} + \left[\left(\frac{150\alpha_2\mu_{\mathrm{f}}}{3.5\alpha_1 D_{\mathrm{particle}}\rho_{\mathrm{f}}}\right)^2 + \frac{D_{\mathrm{particle}} g(\rho_{\mathrm{particle}} - \rho_{\mathrm{f}})}{1.75\alpha_1\rho_{\mathrm{f}}}\right]^2 \quad (4.1)$$

where α_1 and α_2 are suggested to be as 14 and 11, respectively (Wen and Yu, 1966); μ_{f} is kinematic viscosity of the fluidization fluid (g/(cm s)); D_{particle} is sand particle diameter (cm); ρ_{f} and ρ_{particle} are fluidization fluid density and sand particle density (g/cm^3), respectively; g is acceleration due to gravity (cm/sec^2). Substituting μ_{f} = 0.01 g/(cm s), D_{particle} = 1.17 x 10^{-2} cm (= D_{50} in Table 4.1), ρ_{particle} = 2.67 g/cm^3 obtained from G_{s} in Table 4.1, ρ_{f} = 1.0 g/cm^3 for de-aired water and g = 981 cm/sec^2 into Equation 4.1 yields V_{mf} = 1.36 x 10^{-4} m/sec. The applied discharge was around 1.8 x 10^{-3} m/sec from the filter of the fluidization mesh when using de-aired water, which is larger than the estimated minimum fluid velocity for fluidizing the sample (V_{mf} = 1.36 x 10^{-4} m/sec). Applying this discharge during sample preparation, the excess pore pressure ratio (r_{u}) at PPT1 is around 1.0 and r_{u} at PPT3 is around 0.93. Hence, it is believed that this fluidization system is able to uniformly liquefy sand samples during the process of fluidization.

4.3.3. Soil material

Sub-angular and sub-rounded sand, known as Geba Sand, supplied by Eurogrit (www.eurogrit.com) was used in this study which was also used and characterised by De Jager (2018), Askarinejad et al. (2018) and Maghsoudloo et al. (2018). The soil properties are listed in Table 4.1, where D_{10}, D_{50} and D_{60} are the intercepts for 10%, 50% and 60% of the cumulative mass; $\varphi'_{\mathrm{residual}}$ is the residual friction angle; K is coefficient of permeability tested with water as the submerging fluid; e is the

void ratio, and the subscriptions min and max denote the minimum and maximum void ratios, respectively; and G_s is sand specific gravity.

Table 4.1: Main sand properties (after Maghsoudloo et al., 2017)

D_{10} (mm)	D_{50} (mm)	D_{60} (mm)	$\varphi'_{residual}$ (°)	K (m/sec)	e_{min} -	e_{max} -	G_s -
0.078	0.117	0.121	36	4.2×10^{-5} or 1.3×10^{-5}*	0.64	1.07	2.67

*: Theoretical value when the submerging fluid has a viscosity of 3.2 cSt

4.3.4. Pore Fluid

In this study, both de-aired water and de-aired viscous fluid were used. Hydroxypropyl Methylcellulose (HPMC) powder is biodegradable and can dissolve in water easily. Viscous fluid made of HPMC has been widely used in centrifuge modelling considering the difference in the scaled time for the pore fluid generation and dissipation under Ng condition (N times Earth's gravity, g). Dewoolkar et al. (1999) and Ko (1994) argued that the soil constitutive properties will not be changed by HPMC solutions. Stewart et al. (1998) reported that for a concentration of 2% for HPMC, the solution has a density of no more than 0.5% higher than water. Therefore, HPMC powder marketed as Benecel E10M supported by ASHLAND was used in this research.

The employed dispersion method was the 'hot/cold' technique (Company, 2002). The de-aired viscous fluid was made by the following steps: i. approximately 20% of the required volume of water was heated to around 90°C; ii. the HPMC powder was mixed into the warm water in a blender; iii. agitation was continued until the powder was evenly dispersed; iv. the prepared fluid was mixed into the rest of required water; v. the viscous fluid was de-aired by vacuum for at least 12 hours.

4.3.5. Sample preparation procedures at $1g$ condition

The sand mixed with de-aired fluid was put into a vacuum for 24 hours. It was carefully transported into the strongbox, which had been filled with de-aired fluid in advance to avoid any air bubbles. In order to prepare samples easily and in a reproducible manner, the procedures listed in Appendix A were repeated for every centrifuge test. The pore pressure change recorded during the sample preparation for all the samples are similar, which confirms the reproducibility of the fluidization technique. The fluid was put under vacuum for at least 12 hours after every two tests.

There are four main advantages associated with this sample preparation technique. Firstly, the sample preparation time is no more than 40 minutes, which is far less compared than the 8 hours per sample required for the wet pluviation method (Askarinejad et al., 2018); secondly, each sample can be made in the centrifuge carrier, which excludes any possible artificial disturbance before starting the centrifuge; thirdly, no extra space above the strongbox on the centrifuge carrier is needed for preparing a sample, hence, the vertical space of the centrifuge carrier can be fully utilised; lastly, since the same procedures are followed for every test,

the reproducibility, the fully saturated condition and the loose state of the sand samples are ensured. These qualities are discussed in the following section.

4.4. Sample properties

4.4.1. Relative density

The average sand layer height of each test was obtained from five scales which were attached on inside of the Plexiglas walls of the strongbox at different positions (two of them can be seen in Figure 4.11 and the rest of scales were attached onto the other Plexiglas wall) at $1g$ condition and from two scales (see Figure 4.11 and Figure 4.14) at Ng condition. The initial relative densities at $1g$ condition (Dr_{1g}) and relative densities at Ng condition (Dr_{Ng}) are listed in Table 4.2, where N is 10 in this study. As a result of the rise of centrifugal acceleration, the samples became denser.

Table 4.2: Summary of centrifuge tests

Test name*	TR_m (°/sec)	TR_p	g-level (N)	Dr_{1g} (%)	Dr_{Ng} (%)	Height** (m)	θ_f (°)
W_0.01_10g	0.1	0.01	10	28	43	1.07	-
W_0.1_10g	1.0	0.1	10	35	49	1.07	-
W_0.2_10g	2.0	0.2	10	20	32	0.74	13.4
V_0.01_10g_NoSand	0.1	0.01	10	-	-	-	-
V_0.01_10g	0.1	0.01	10	23	35	0.83	17.7
V_0.05_10g	0.5	0.05	10	27	37	0.86	12.2
V_0.1_10g	1.0	0.1	10	31	42	0.83	11.1
V_0.2_10g	2.0	0.2	10	27	43	0.88	9.0

*: W stands for de-aired water; V stands for viscous fluid; the number after W or V stands for the testing tilting rate at prototype scale in [°/sec]; 10g represents the testing g-level; NoSand means the test was done with viscous fluid only and no sand.
**: prototype scale

4.4.2. Degree of saturation

Submerged sand samples were kept under vacuum for more than 24 hours before being transferred into the strongbox. The sand column method (Chapuis, 2004) was adopted to examine the degree of saturation (S_r) of sand layer after fluidization. Results are presented in Table 4.3. The prepared de-aired viscous fluid was put under vacuum after every two tests.

Table 4.3: Degree of saturation measured from four samples after fluidization

	Sample 1	Sample 2	Sample 3	Sample 4	Average
S_r (%)	99.9 ±1.8	98.7 ±1.7	98.7 ±1.6	99.2 ±1.7	99.1 ±1.7

4.4.3. Uniformity

Petrovic et al. (1982) concluded that computed tomography (CT) scanning is a useful technique to evaluate soil bulk density. The homogeneity (Table 4.2) in terms of relative density was investigated by scanning a sample using a Siemens Somatom Volume Zoom CT scanner with a maximum resolution of 0.6 mm. This CT scanner is capable of generating 24 sequential images for a layer with thickness of 30 mm in a single scan. Thus, each image has a thickness of 1.25 mm. Each pixel of the images has a size of 0.59 x 0.59 mm^2. The voltage and current were set at 120 kV and 35 mA, respectively.

A loose soil sample was made following the same preparation procedures as that applied for other samples listed in Table 4.2. This sample was prepared directly on the CT scanner table so that the sample was intact before scanning. The same sand and de-aired water was used. The influence of fluid viscosity on the samples' homogeneity is considered to be insignificant as all the tested samples were fully fluidized and consolidated at $1g$ condition. Therefore, the soil properties of this sample are assumed to be similar to that of centrifuge test samples. The computed tomography number (CT_{number}), which is expressed in Hounsfield Units (HU) and is proportional to the densities of scanned materials. Figure 4.5 illustrates 3D view of the strongbox in HU in grey-scale. In Figure 4.5 and following figures which are shown in HU, a material with higher density is presented brighter than a material with a lower density. For example, in Figure 4.5, the density of the aluminium frame of the strongbox (number 8) is higher than that of submerged sand (number 4) which is higher than that of submerging fluid (number 3), hence number 8 is the brightest and number 3 has the lowest brightness among these three materials. The air has the lowest density in the system, therefore it is shown in black in these images. With assumption of full saturation, the sand sample can be considered as a porous medium with two phases.

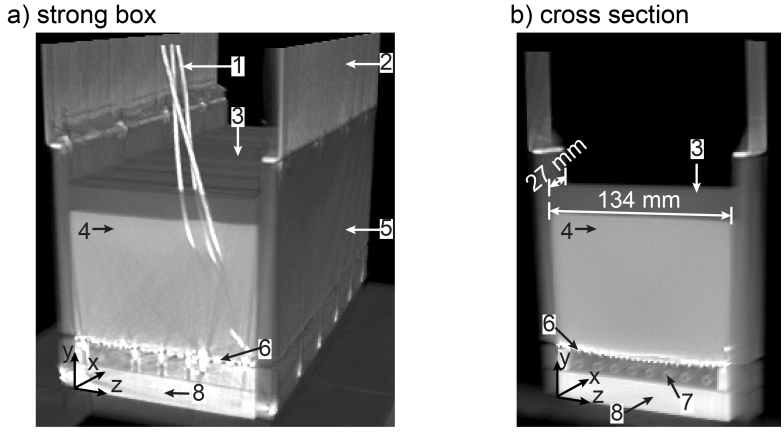

Figure 4.5: 3D view of the strongbox in Hounsfield Units in grey-scale (model scale): 1) cables of PPTs; 2) extension box; 3) submerging fluid (de-aired water); 4) submerged sand; 5) Plexiglas; 6) filter layer; 7) parallel fluidization pipes; 8) base of the U-shape aluminium frame of the strongbox

Calibration of CT results

The CT_{number} is proportional to scanned material density when the voltage of the CT scanner is larger than 100 kV (Gupta et al., 2018, Higo et al., 2011). Based on the CT_{number} for air, water, Plexiglas and aluminium which have densities of 0.0012 g/cm^3, 1 g/cm^3, 1.19 g/cm^3 and 2.7 g/cm^3, respectively, the CT scanner was calibrated as shown in Figure 4.6. The bulk density of saturated sand material can be expressed in Equation 4.2, ρ_{f} is submerging fluid density which is 1 g/cm^3 in this study. Thus, sample void ratio can be obtained from CT_{number} based on Equation 4.3, where $\alpha_1 = 0.0010$ and $\alpha_2 = 1.0146$ are two parameters determined after calibrating CT_{number}.

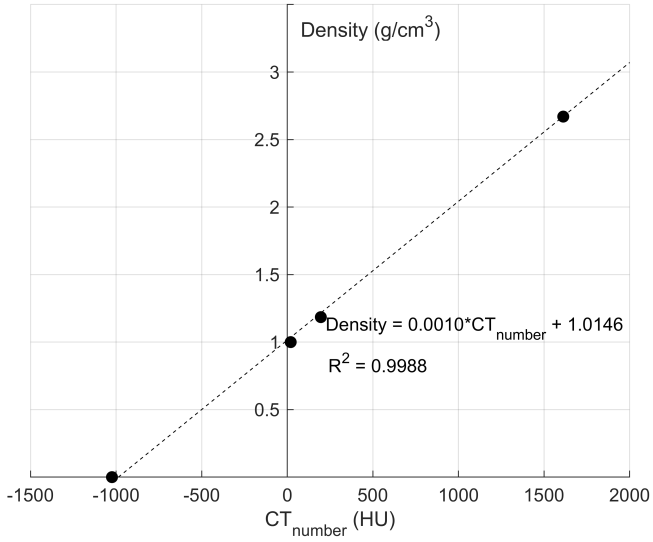

Figure 4.6: Calibration of CTnumber

$$\text{Bulk density} = \frac{G_{\text{s}} + e\rho_{\text{f}}}{1+e} \tag{4.2}$$

$$e = \frac{G_{\text{s}} - 1}{\alpha_1 CT_{\text{number}} + \alpha_2 - 1} - 1 \tag{4.3}$$

Beam hardening correction (BHC) method

Due to the difference in densities of the submerged sand and the stainless steel (filter layer) there are beam hardening artefacts existing in the sample especially in the zone close to the filter layer. A large unexpected variation in CT_{number} was observed. Application of advanced and complicated beam hardening correction (BHC) algorithms, such as the algorithms proposed by Kyriakou et al. (2010) and Gu and Dogandžić (2016), is out of scope of this study; hence, a simple way of

correcting beam hardening was adopted. According to the maximum and minimum void ratios (Table 4.1) and Equation 4.3, the largest and lowest expected CT_{number} can be obtained which are 975.4 (HU) and 760.1 (HU). Thus, every CT_{number} which either exceeds 965.7 (HU) or lower than 760.1 (HU) is deleted.

Relative density distribution along sample height, width and length

It should be noted that due to the setting of the CT scanner, only a slice of sample with a thickness around 30 mm in length direction, i.e. x direction, could be scanned still as shown in Figure 4.5; then the scanner table carrying the strongbox had to be moved in order to scan the whole sample in x direction. However, due to the movement of the scanner table the sample was disturbed. Hence, only relative density distributions over sample width and depth could be obtained from the undisturbed sample (Figure 4.7a); relative density distribution over sample length could be only evaluated based on the same sample which was partially disturbed as illustrated in Figure 4.7b.

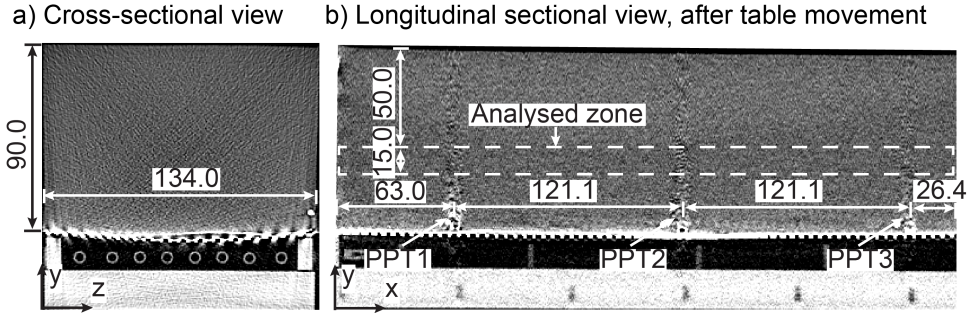

Figure 4.7: 2D view of the sample in Hounsfield Units in grey-scale (model scale): a) Cross-sectional view scanned before the table movement used for analysing the Dr distribution along width and depth; b) Longitudinal sectional view scanned after the table movement and the analysed zone is used for analysing Dr distribution along sample length

Figure 4.7a demonstrates 2D view of cross section of the sample (around 27 mm in out-of-plane direction, i.e. x direction). The whole sand sample cross section (90×134 mm^2) was used to analyse the relative density distribution over sample depth and width. The Dr along the sample depth is illustrated in Figure 4.8. By comparing with the results before and after BHC, it can be seen that the beam hardening artefacts exist and go severely from depth 60 mm to sample bottom and a large amount of beam hardening artefacts can be corrected by the BHC method.

Results after BHC shows that, the relative density profile over sample depth is characterized by a looser top layer (0 mm - 10 mm), a denser bottom layer (from 70 mm to 90 mm) and a relative constant value in between (Figure 4.8). It is reasonable that the sample bottom layer is denser than the sand above, as the vertical effective stress increases with the sample depth. However, there might be still some beam hardening artefacts in the bottom layer, considering the fact that the effortless BHC method applied in this study is a simplistic. The Dr profile over sample width is uniform from 7 mm to 124 mm (Figure 4.9). The relatively low Dr

near the two sides might be a consequence of the wall friction effect during sand sedimentation. It can be concluded that the main sample is reasonably uniform in the cross-section plane. The average relative densities over depth and width are around 30.8% (with a standard deviation of 7.4%) and 30.4% (with a standard deviation of 3.1%), respectively.

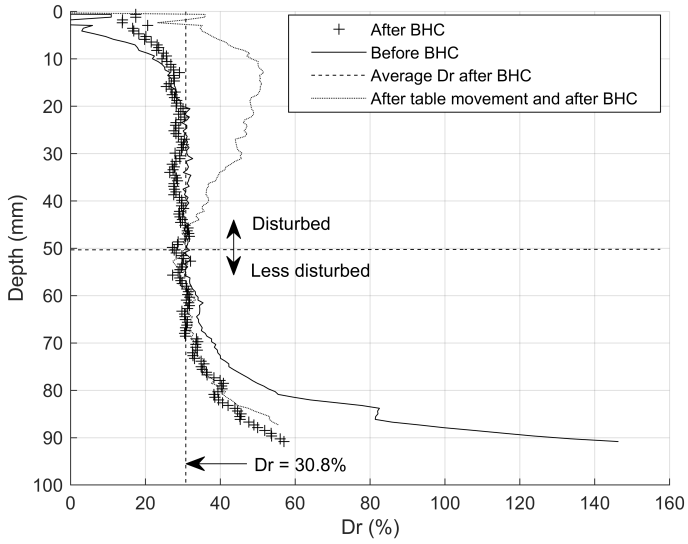

Figure 4.8: Variation of relative density over depth (model scale)

The Dr profile in the length direction for the sample that was affected by the movement of CT Scanner table shows that the top 50 mm sand was densified, however below 50 mm the sand remained nearly unaffected (Figure 4.8). The top 10 mm of the sample was looser than the sand below, hence this part of sand was prone to densification. However, a 50-mm depth of sand was densified. This might be due to the disturbance being strong enough to densify the sample more than the top 10-mm layer, and the densification of this layer may further influence the sand below due to the dissipation of pore pressure that was expected to be generated. Therefore, not the whole sample but only the analysed zone, in Figure 4.7b, which was selected to be within the sample depth from 50 mm to 70 mm, was used to obtain the Dr distribution over sample length. The analysed zone is assumed to be less affected by the movement of the scanner table and beam hardening effects from the filter. Dr along the sample length is presented in Figure 4.10. The existence of PPTs might influence the Dr above them and beam hardening artefacts caused by the sensors might be not corrected completely. Considering the Dr in sample length, it is believed that the sample is uniform in this direction as well. The average relative density over length is about 29.6% with a standard deviation of 5.9%.

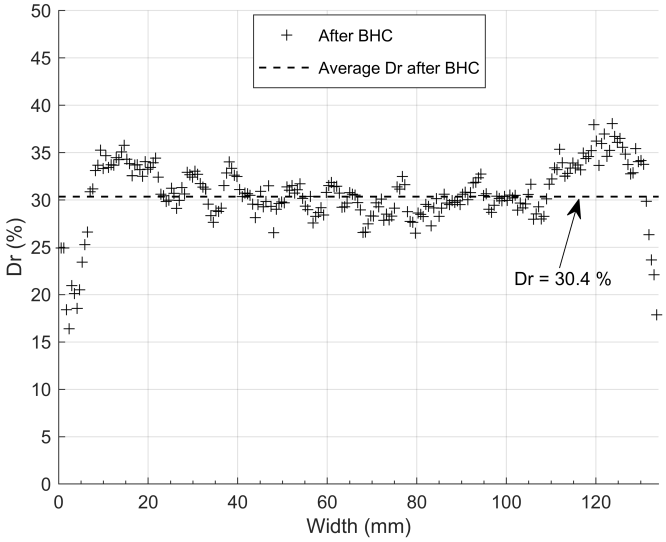

Figure 4.9: Variation of relative density over width (model scale)

4.5. Submarine landslide triggering mechanism

A single-plane rotatable set-up was designed to study static liquefaction of submarine slopes induced by the slope over-steepening as a result of the scouring effect (De Groot et al., 2012) or dredging actives. The overview of this set-up is shown in Figure 4.11. The base plate, supporting the strongbox, is connected to the 40-mm rotating axis with five bearing blocks. The set-up can rotate using a linear actuator (Linak 282100-40150100, capacity: 1 kN). Six shaft blocks connect the casing of the rotating axis to the centrifuge carrier. The outer frame, which consists of four angled profiles at four corners and a lid plate on the top, keeps the strongbox in place and prevents sliding during tilting. A potentiometer (S13FLP25A) linking the base plate and the centrifuge carrier is used to measure the tilting angle. For safety reasons, in case of excessive tilting two end switches were installed. Metal components of the set-up are made of (7075 aluminium sheet) and designed to be as light as possible.

The weight of the sample is mainly carried by the casing of the rotating axis below the middle of the strongbox, therefore this structure of the set-up requires a low capacity for the linear motor. Furthermore, a smooth and linear change of load acting on the linear motor during tilting is expected. The set-up can bear a maximum static load of 47 kN. The maximum tilting angle is 20°. By controlling the linear motor, the strongbox can rotate with a tilting rate ranging from 0.1°/sec to 2.0°/sec with a precision of 0.002°/sec at model scale; the corresponding tilting rates at prototype will be N times smaller than that at model scale as explained in the next section.

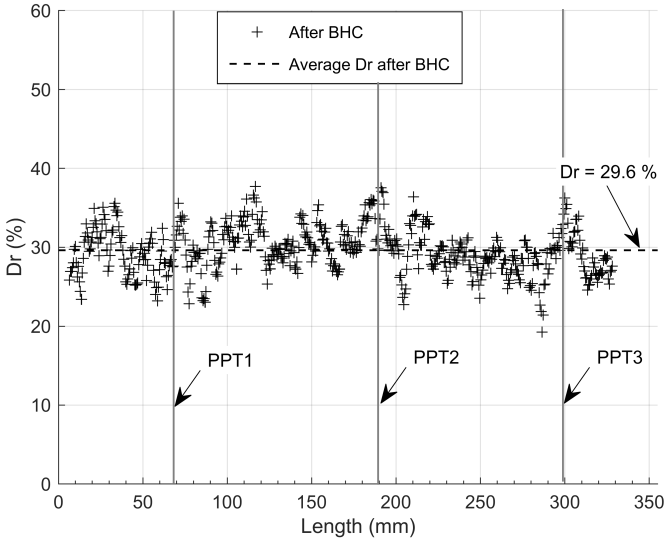

Figure 4.10: Variation of relative density over length (model scale)

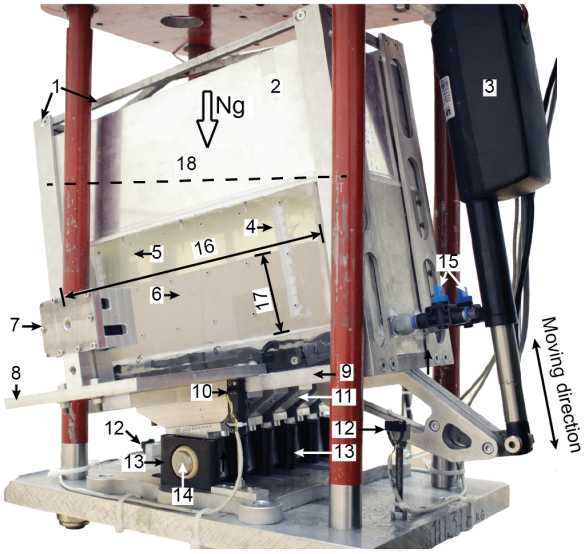

Figure 4.11: Test set-up in the centrifuge carrier (model scale): 1) outer frame; 2) extension box; 3) linear motor; 4) scale; 5) fluid; 6) submerged sand; 7) high resolution, high speed camera; 8) camera holder; 9) base plate; 10) linear potentiometer; 11) bearing blocks; 12) switches; 13) shaft blocks; 14) rotation axis; 15) valves; 16) sample length: 355 mm; 17) sample height: 87 mm; 18) fluid table (it is initially parallel to the sample bottom with a distance of 180 mm)

4.6. Scaling law

4.6.1. Scaling law for tilting rate

In a centrifuge test, the scale factor for acceleration (a) is $a_r = a_p / a_m = 1 / N$, where henceforward the subscripts 'p', 'm' and 'r' indicate prototype, model and the ratio of prototype to model, respectively; furthermore, the scale factor for length (L) is $L_r = L_p / L_m = N$. Therefore, considering the unit of acceleration, the scale factor for kinematic time (t_r^k) is:

$$t^k = \sqrt{\frac{L}{a}},\ t_r^k = \sqrt{\frac{t_p^k}{t_m^k}} = \sqrt{\frac{L_p a_m}{L_m a_p}} = N \tag{4.4}$$

where the superscript 'k' refers to kinematic. Tilting rate has a unit of degree per second. The scale factor for slope angle is unity. Hence, the scale factor for tilting rate is:

$$TR_r = \frac{TR_p}{TR_m} = \frac{1}{t_r^k} = \frac{1}{N} \tag{4.5}$$

4.6.2. Scaling laws for pore fluid viscosity for static liquefaction

Based on Darcy's law, the specific discharge (q) can be expressed in the form of Equation 4.6, where q has a unit of m/sec, K is the hydraulic conductivity (as shown in Equation 4.7), which is also called the coefficient of permeability with a unit of m/sec, i is the hydraulic gradient (dimensionless), κ is the intrinsic permeability (m^2) which depends on the soil properties, μ is the dynamic viscosity (kg m^{-1} s^{-1}), ν is the kinematic viscosity (St), ρ_f is the fluid density and γ_f is the unit weight of fluid at which the permeability is measured (Zienkiewicz et al., 1999).

$$q = Ki \tag{4.6}$$

$$K = \frac{\kappa \gamma_f}{\mu},\ \mu = \nu \rho_f \tag{4.7}$$

Macroscopic scale

It is widely accepted that, in a $1/N$-time scaled model under Ng condition, the scale factors for K, i and q are 1, $1/N$ and $1/N$, respectively, if the same pore fluid and soil are used in the model and prototype (Arulanandan et al., 1988, Cargill and Ko, 1983, Garnier et al., 2007, Singh and Gupta, 2000, Taylor, 1995). Hence, the scale factor for the seepage time (t_r^s) is N^2 as shown in Equation 4.8 (Schofield, 1980, Taylor, 1995), where the superscript 's' refers to seepage. Due to the conflict between the scaling laws for the kinematic time (Equation 4.4) and seepage time (Equation 4.8), a pore fluid which is N times more viscous than water is recommended (e.g. Dewoolkar et al., 1999, Schofield, 1980, Taylor, 1995). The viscous fluid makes the

ratio of kinematic time to seepage time in the prototype equals to that in the model, as explained in the Equations 4.9 and 4.10.

$$t^{\mathrm{s}} = \frac{L}{q},\ t_{\mathrm{r}}^{\mathrm{s}} = \frac{L_{\mathrm{r}}}{q_{\mathrm{r}}} = N^2 \tag{4.8}$$

$$\frac{\mu_{\mathrm{p}}}{\mu_{\mathrm{m}}} = \frac{1}{N} \rightarrow \frac{K_{\mathrm{p}}}{K_{\mathrm{m}}} = N \rightarrow \frac{q_{\mathrm{p}}}{q_{\mathrm{m}}} = 1 \rightarrow \frac{t_{\mathrm{p}}^{\mathrm{s}}}{t_{\mathrm{m}}^{\mathrm{s}}} = N \tag{4.9}$$

$$\frac{t_{\mathrm{p}}^{\mathrm{k}}}{t_{\mathrm{p}}^{\mathrm{s}}} = \frac{t_{\mathrm{m}}^{\mathrm{k}}}{t_{\mathrm{m}}^{\mathrm{s}}} \text{ or } t_{\mathrm{r}}^{\mathrm{k}} = t_{\mathrm{r}}^{\mathrm{s}} \text{ (when } \frac{\mu_{\mathrm{p}}}{\mu_{\mathrm{m}}} = 1/N) \tag{4.10}$$

Grain scale

Take et al. (2004) proposed that soil collapse initiates the sudden increase of pore pressure, which can be the triggering mechanism of static liquefaction. They mentioned that the duration of the generation of excess pore pressure can be a function of falling distance of a grain on to another (h) and acceleration as expressed in Equation 4.11, where the superscripts 'gen' and 'grain' stand for 'generation' and 'grain scale', respectively. The scaling factor for length related factors is 1 at grain scale (Askarinejad et al., 2015).

$$t^{\mathrm{gen,grain}} \propto \sqrt{\frac{h}{a}},\ t_{\mathrm{r}}^{\mathrm{gen,grain}} = \sqrt{\frac{1}{a_{\mathrm{r}}}} = \sqrt{N} \tag{4.11}$$

Askarinejad et al. (2015) postulate that the initial soil voids collapse should happen locally and hence the grain scale is of interest in the case of static liquefaction. They argue that the generation time of excess pore pressure due to the collapse of soil structure is $\sqrt{N}$ times slower than its dissipation time at grain scale under Ng acceleration (see Equation 4.11). Therefore, a fluid which is $\sqrt{N}$ times more viscous than water as the pore fluid for a test at Ng is recommended so that the time for excess pore pressure generation and that for excess pore pressure dissipation are both scaled with the same factor as explained in Equations 4.12 and 4.13.

$$\frac{\mu_{\mathrm{p}}}{\mu_{\mathrm{m}}} = \frac{1}{\sqrt{N}} \rightarrow \frac{K_{\mathrm{p}}}{K_{\mathrm{m}}} = \sqrt{N} \rightarrow \frac{q_{\mathrm{p}}}{q_{\mathrm{m}}} = \frac{1}{\sqrt{N}} \rightarrow \frac{t_{\mathrm{p}}^{\mathrm{s,grain}}}{t_{\mathrm{m}}^{\mathrm{s,grain}}} = \sqrt{N} \tag{4.12}$$

$$t_{\mathrm{r}}^{\mathrm{gen,grain}} = t_{\mathrm{r}}^{\mathrm{s,grain}} \text{ (when } \frac{\mu_{\mathrm{p}}}{\mu_{\mathrm{m}}} = \frac{1}{\sqrt{N}}) \tag{4.13}$$

Therefore, based on the scaling laws for pore fluid at grain scale, a submerging fluid with a viscosity of $\sqrt{10}$ should be used for a test under $10g$ condition. Hence, HPMC powder was used in this study to make the viscosity of the submerging fluid to be 3.2 cSt. The permeability of the sample with the viscous fluid was 3.2 times less than 4.2 $\times 10^{-5}$ m/sec, i.e. 1.3 $\times 10^{-5}$ m/sec (Table 4.1). Furthermore, in order to investigate fluid viscosity effect on the sample failure water as the submerging fluid was also applied.

4.7. Results and Discussion

The landslides were triggered by tilting the sand layers gradually. To investigate the effects of the steepening rate of slope on slope instability, four tilting rates, namely 0.01 °/sec, 0.05 °/sec, 0.1 °/sec and 0.2 °/sec at prototype scale, were tested at $10g$. The tilting started around 1200 seconds (prototype scale) after achieving the target g-level. No change in pore pressure was noticed before tilting, i.e. the consolidation due to the increase in g-level had finished. The characteristics of the tests are summarised in Table 4.2.

4.7.1. Coriolis effect on very loose sample during increasing of g-level

Due to the high sensitivity of the very loose sand samples, the standard increment rate of the angular velocity of the geo-centrifuge at TU Delft, which takes 67 seconds from $1g$ to $10g$, could cause a local liquefaction (Figure 4.12). This disturbance could happen due to the Coriolis effect. Hence, a very low increasing rate of centrifugal acceleration was adopted for all the tests listed in Table 4.2, which would take 990 seconds from $1g$ to $10g$ and could provide a gradual and smooth increase of hydrostatic pressure during the process of rising g-level.

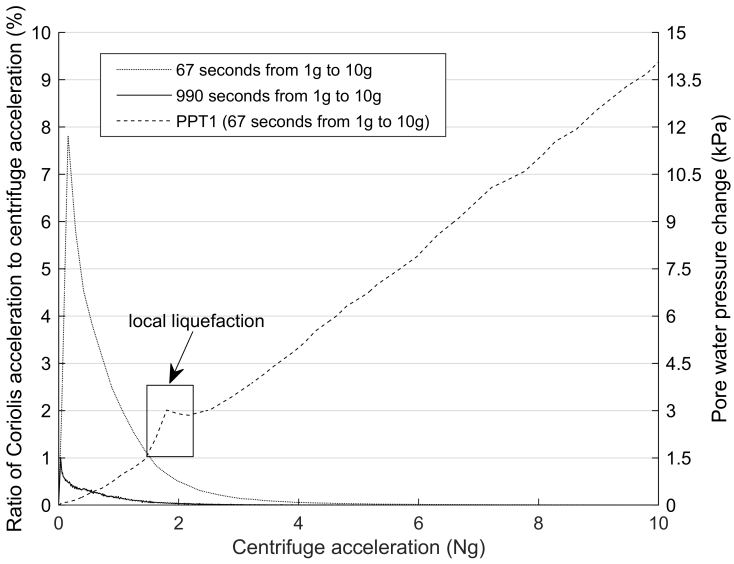

Figure 4.12: Ratio of Coriolis acceleration to centrifuge acceleration and partial liquefaction during increasing of g-level

The Coriolis acceleration (a_{Coriolis}) depends on the centrifuge angular velocity (ω) and the sample velocity in the centrifuge rotation plane (v_{rotation}), as described in Equation 4.14 (Schofield, 1980), where R_{ac}, R_{beam} and R_{sample} in Equation 4.15 are the centrifuge rotation radius, length of centrifuge beam and the distance be-

tween the hinge of the centrifuge carrier and 1/3 of the sample height, respectively, and β is the position angle indicating the rotation of the centrifuge carrier. During the development of ω, the centrifuge acceleration (a_c) rises and the sample position changes with increasing β as illustrated in Figure 4.13 and Equation 4.16. In this process, the soil sample moves in the centrifuge rotation plan, hence it has a certain velocity in the centrifuge rotation plane v_{rotation} which can be expressed in Equation 4.17. The changing rate of β (Equation 4.18) can be obtained from Equations 4.15 and 4.16.

Figure 4.12 demonstrates that the maximum value of a_{Coriolis}/a_c is about 7.8% when the centrifuge takes 67 seconds from $1g$ to $10g$ and it is around 1% when the centrifuge takes 990 seconds from $1g$ to $10g$. Hysteresis upon the local liquefaction was observed. Taylor (1995) proposed that Coriolis effects could be negligible when the ratio of Coriolis acceleration to centrifuge acceleration is less than 10% for dynamic modelling in centrifuge. However, this limit needs to be lowered for testing a saturated loose sand sample with Dr in the range of 20% - 30%. It is found that 1% is a reasonable value as the limit of a_{Coriolis}/a_c in this case.

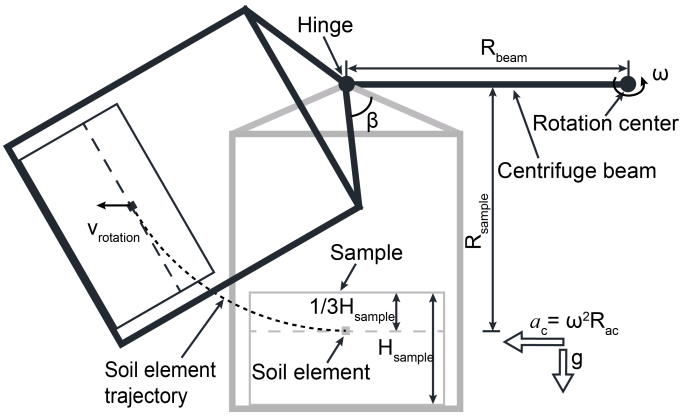

Figure 4.13: Schematic description of sample moving velocity in the centrifuge rotation plane during the process of increasing centrifuge acceleration (grey: initial position when ω= 0; black: position due to a certain amount of ω)

$$\frac{a_{\text{Coriolis}}}{a_c} = \frac{2\omega v_{\text{rotation}}}{\omega^2 R_{\text{ac}}} \tag{4.14}$$

$$R_{\text{ac}} = R_{\text{beam}} + R_{\text{sample}} \sin\beta \tag{4.15}$$

$$\beta = \tan^{-1}\left(\frac{\omega^2 R_{\text{ac}}}{g}\right) \tag{4.16}$$

$$v_{\text{rotation}} = \frac{d(R_{\text{sample}} \sin\beta)}{dt} = R_{\text{sample}} \cos\beta \frac{d\beta}{dt} \tag{4.17}$$

$$\frac{d\beta}{dt} = \frac{2\omega R_{ac}}{g + \omega^4 {R_{ac}}^2/g - \omega^2 R_{sample}\cos\beta}\frac{d\omega}{dt} \tag{4.18}$$

4.7.2. Sample failure

A high resolution (3840 x 2160 pixels), high speed camera (the highest frame rate is 30 fps) was used to take videos during all tests. The camera was connected to the tilting device with the camera holder (Figure 4.11). Thus, it could rotate together with the strongbox. The captured videos (30 fps) show that the slope failures happened almost without any visible precursor. Figure 4.14 illustrates three frames at three tilting angles (θ), namely 0°, 17.0° and 17.7°, for test V_0.01_10g (Table 4.2). There was no local or global movement could be detected during tilting before the liquefaction. The videos indicate that the liquefaction happened over the entire length and around 85% depth of the sample.

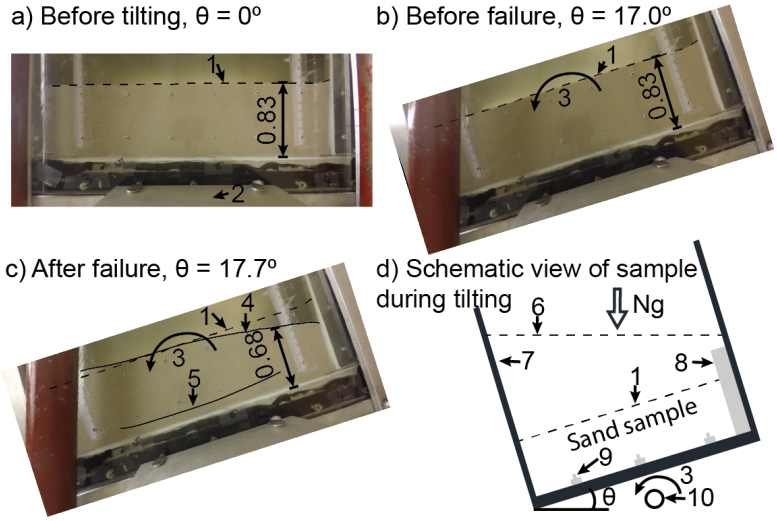

Figure 4.14: Three frames of V_0.01_10g (prototype scale): 1) sand surface before tilting/failure; 2) camera holder; 3) tilting direction; 4) sand surface after failure; 5) observed failure surface; 6) water table; 7) strongbox; 8) PVC block; 9) PPTs (from left to right: PPT1, PPT2 and PPT3); 10) rotation axis

Due to the fact that excess pore pressure dissipated during the liquefaction, the sliding sand stopped when the excess pore pressure reduced to zero. It should be noted that boundary effects would be expected from the low end of the strongbox which would prohibit moving of liquefied sand. It is expected that a larger scale in length would give a gentler slope after failure (De Groot et al., 2019). Considering that W_0.01_10g and W_0.1_10g did not fail up to the maximum tilting angle of the setup (20°), while all other tests failed before reaching the limitation (Table 4.2), it can be concluded that the boundary effects play an important role in the post-failure behaviour of flow slides, but barely influence the samples before the onset of liquefaction. Since this paper mainly focuses on investigating the triggering

mechanism of static liquefaction, we believe that the boundary effects are of minor importance before the onset of static liquefaction.

4.7.3. Failure angle

The failure angles for centrifuge tests are demonstrated in Figure 4.15 with respect to the tilting rate at prototype scale. The tilting rate effect on slope instability can be revealed by comparing the failure angles in slopes with the same viscous fluid (Figure 4.15). A reduction in the failure angle is visible with the increasing tilting rate. This is also observed from results of $10g$ tests with water, as failure occurred in W_0.2_10g but did not happen in W_0.1_10g and W_0.01_10g. The generation and dissipation of pore pressure coexist when a fully saturated sand sample is under shearing (Goren et al., 2010, Iverson, 1993, Taylor, 1995). It is reasonable to assume that the dependency of slope instability on tilting rate is related to the difference between the pore pressure generation rate and the pore pressure dissipation rate. A faster increase of the slope angle increases the probability of the occurrence of micro-collapses in the soil body and hence triggers the switch of the drainage condition from drained to undrained, which then causes the generation of the excess pore pressure and liquefaction.

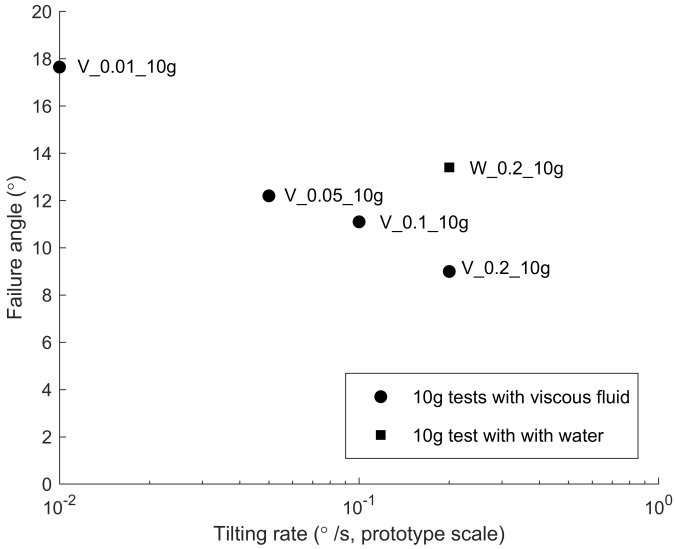

Figure 4.15: Tilting rate effect on slope failure angles for $10g$ tests

The tilting mechanism applied in the centrifuge tests mimics the rise of seabed slope angle as a result of scouring/dredging. Therefore, the development of stress state for a soil element in the samples is similar to that of a soil element which lies below a seabed slope with gradually increasing inclination as shown in Figure 4.1. The tilting rate effect, i.e. slope angle changing rate ($\dot{\theta}$) effect, is expressed in Figure 4.16. For a test with a higher tilting rate, the sample was stable before

arriving at point B1 with a failure angle of θ_{f1}, and then the stress state follows path 1 till to full liquefaction at point C; for a test with a lower tilting rate, the stress path continues further under a drained condition to point B2 with a failure angle of $\theta_{f2}(> \theta_{f1})$ following by the path 2 under an undrained condition. It can be inferred that the instability line is a function of shear rate as demonstrated in Figure 4.16.

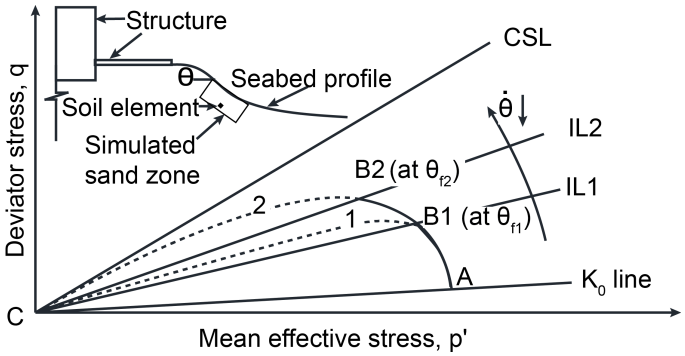

Figure 4.16: Dependency of static liquefaction triggering mechanism on slope angle changing rate

This postulation can also explain the two tests performed by De Jager (2018) in the Liquefaction Tank as shown in Table 4.4. Test1, with a tiling rate of 0.12 °/sec, failed at a slope angle of 6.1°, while Test2, with a tiling rate of 0.01 °/sec, did not fail even at a slope angle of 10° (the maximum tilting angle of the Liquefaction Tank). Test1 and V_0.1_10g have a similar tilting rate, while the slope failure angles for these two tests are different (i.e. 6.1° for Test1 and 11.5° for V_0.1_10g). It is believed that the difference in the relative densities of these two tests (i.e. 35.0% for Test1 and 41.0% for V_0.1_10g) is the main reason for the difference in the failure angles (Askarinejad et al., 2019).

Table 4.4: Two tests performed by De Jager (2018) in the $1g$ Liquefaction Tank

Test name	Tilting rate (°/sec)	D_r (%)	Failure angle (°)	Sand layer height (m)
Test1	0.12	35.0	6.1	0.51
Test2	0.01	35.9	No failure*	0.51

*: The maximum tilting angle for the Liquefaction Tank is 10°.

It can be found that the fluid viscosity plays an important role in triggering static liquefaction as well. W_0.2_10g failed at a larger slope angle than V_0.2_10g (the failure angles for W_0.2_10g and V_0.2_10g are 13.4° and 9.9°, respectively), and W_0.1_10g and W_0.01_10g did not fail but V_0.1_10g and V_0.01_10g failed. The pore fluid viscosity of the tests with viscous fluid is 3.2 times higher than that for the tests with water. Therefore, the possible generated pore pressure for the tests with water dissipates 3.2 times faster than that for the tests with viscous fluid. Dewoolkar et al. (1999) discovered a similar behaviour from results of level ground seismic centrifuge tests. By giving the same earthquake motion, the sample

submerged by a viscous fluid liquefied, while the sample submerged by water did not.

4.7.4. Excess pore pressure due to static liquefaction

Static liquefaction of submerged loose sand layer is related to sudden development of pore fluid pressure, which reduce effective stresses under undrained conditions. Therefore, knowing the behaviour of pore fluid pressure during the increase of slope angle is important to evaluating the sand behaviour. Pore fluid pressures were measured using three pore pressure transducers (PPT1, PPT2 and PPT3) located at sample bottom as illustrated in Figure 4.2 and Figure 4.14.

Figure 4.17 demonstrates the pore fluid pressure change for tests V_0.01_10g_NoSand and V_0.01_10g taking the pore fluid pressure before the tilting as zero. V_0.01_10g_NoSand was performed with viscous fluid only but no sand. During tilting, the slope angle increased, as shown in Figure 4.14, however the fluid table remained perpendicular to the direction of the resultant centrifuge acceleration. Therefore, the distance between the fluid surface and each PPT changed according to the tilting angle. As a result of increasing fluid table near slope toe, the hydrostatic fluid pressure of PPT1 increased, i.e. positive values as illustrated in Figure 4.17. PPT3 shows the opposite change since it was situated at slope crest side. The hydrostatic fluid pressure of PPT2 dropped less than that of PPT3 as it was close to the middle of the sample (see Figure 4.2). Moreover, the transient build-up of pore pressures indicates the static liquefaction for V_0.01_10g. The moment at which the pore pressure starts to increase is defined as the moment of failure.

The difference between the pore fluid pressures from the tests with sand (V_0.2_10g, V_0.1_10g, V_0.05_10g and V_0.01_10g) and the hydrostatic fluid pressures from V_0.01_10g_NoSand gives the change of excess pore pressure as shown in Figure 4.18. The transient increase in excess pore pressures was detected in all the four tests. Due to the fact that the data logging rate was one sample per five seconds at prototype scale (two samples per second at model scale), details of the development of pore pressures were not completely recorded especially for V_0.2_10g which has the highest tilting rate (see Figure 4.18a). Assuming the transient excess pore pressures increased and decreased linearly around their summits, the maximum excess pore pressures can be taken as the intersection of growing segment and declining segment of the transient excess pore pressures, for instance, the estimated peak for PPT1 in Figure 4.18a.

For tests V_0.2_10g and V_0.1_10g, PPT3 detected a faster variation in pore pressure than PPT1 and PPT2 which can be seen around five seconds (prototype scale) before the failures. While after failure, the pore pressures recorded by PPT1 and PPT2 increased faster than that recorded by PPT3 before reaching the peaks. It implies that a local part of the samples failed firstly and then caused the liquefaction. This local area should be closer to PPT3 (near slope crest during the change in slope angle) than the other two sensors. Positive excess pore pressures were observed in tests V_0.2_10g to V_0.05_10g, while, in contrast, slight negative excess pore pressures were detected in test V_0.01_10g before failure. It can be inferred that a

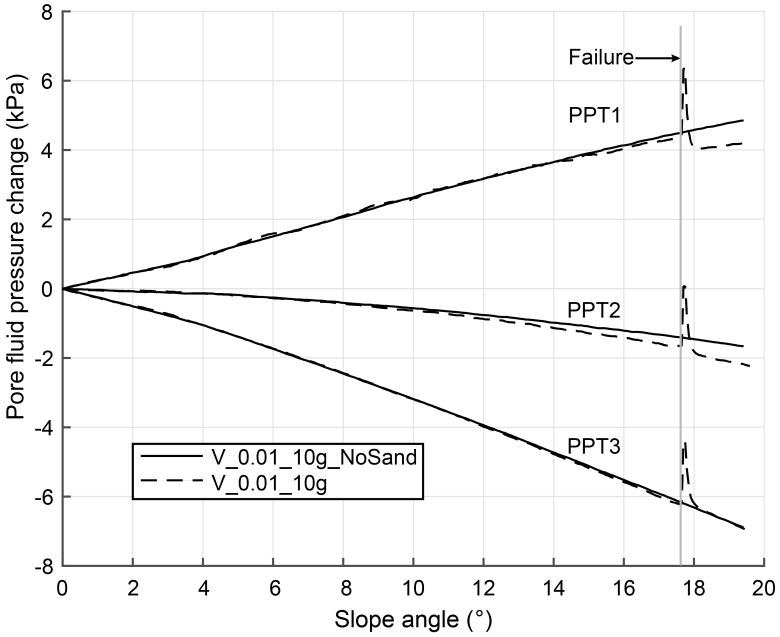

Figure 4.17: Pore pressure change with increasing slope angle for tests V_0.01_10g_NoSand and V_0.01_10g

faster changing rate of the slope angle (V_0.2_10g to V_0.05_10g) would result in a faster growth of shear stress in the loose sand layer, hence a quicker increase in excess pore pressure due to the contraction of the sand layer. The negative excess pore pressures for V_0.01_10g indicate that dilation was happening at the bottom layer of the sample before the failure, however, the side images captured during this test show that the top loose layer of the sample failed first and the liquefied zone propagated quickly toward the lower levels of this sample.

The excess pore pressure ratio for a soil element inside a submerged infinite slope can be defined using Equation 4.19 (Biondi et al., 2000),

$$r_{\mathrm{u}} = \frac{\Delta u}{\sigma_v'} = \frac{\Delta u}{\gamma' H \cos\theta_{\mathrm{f}}} \tag{4.19}$$

where, Δu is the measured excess pore pressure, γ' is the effective unit weight, H is the normal distance between the slope surface and the soil element, θ_{f} is the slope angle (at failure). The excess pore pressure ratios (r_{u}) for the centrifuge tests with liquefaction are demonstrated in Figure 4.19. The excess pore pressure distribution was very much influenced by the dynamic motion of the liquefied mass during slope failures, i.e. affected by the post-failure behaviour. Hence the excess pore pressure ratio at the position of PPT1 (near slope toe) is the highest and that of PPT3 (near slope crest) is the lowest among the three PPTs (see Figure 4.2).

According to the definition of r_{u} (Equation 4.19), r_{u} = 1 would be expected when

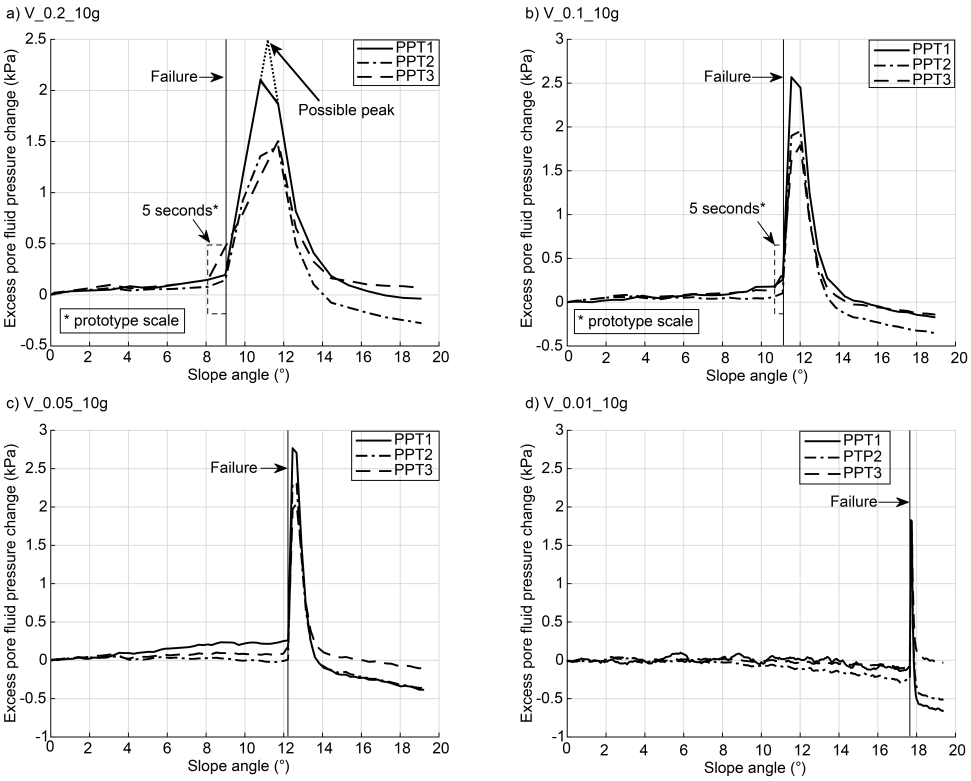

Figure 4.18: Excess pore pressure with increasing slope angle for $10g$ tests with viscous fluid Excess pore pressure ratio

liquefaction happens. However, all the obtained r_u values are less than 1 in this study. This might be explained by the following two facts: firstly, only around 85% of the depth of the samples failed during slope liquefaction whereas the PPTs were located at sample bottom. Since the pressure generation and dissipation coexist during flow slides, the excess pore pressure measured by the sensor is less than that in the sliding soil mass; secondly, the real maximum excess pore pressures might not be recorded by the PPTs due to the relatively low data logging rate as explained in Figure 4.18a.

4.8. Summary and Conclusions

In this study, the performance of a newly developed strongbox with an integrated fluidization system for preparing very loose, fully saturated and uniform sand samples were discussed. Moreover, the details of a novel setup made for simulating triggering mechanisms of submarine landslides in a beam centrifuge have been illustrated. The soil properties of the samples have been examined using computed tomography technique. The tilting rate effects have been investigated by testing

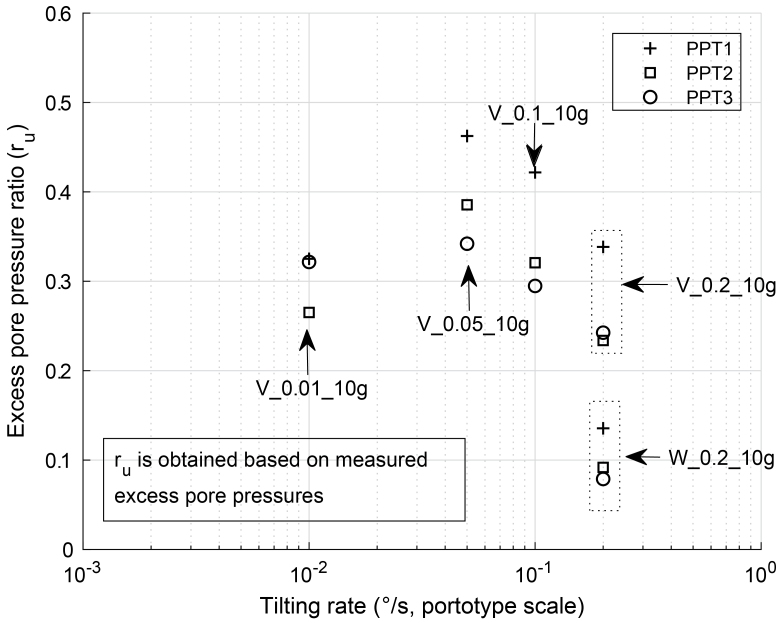

Figure 4.19: Excess pore pressure ratios for all $10g$ tests with static liquefaction

samples at various slope steepening rates under $10g$ conditions. Static liquefaction has been observed at various slope angles. Submerging fluid has been prepared based on the scaling law for pore fluid flow at the grain scale. The main conclusions are presented below:

- The fluidization technique can be applied to prepare samples for centrifuge models. This technique could make reproducible, very loose and uniform fully saturated samples directly on the beam centrifuge carrier ruling out any disturbance which could be caused by sample transportation. Less effort is needed compared to the traditional techniques such as dry pluviation, moist tamping, drizzle and wet pluviation methods.
- Statically liquefied submarine landslides can be triggered in centrifuge condition by the tilting technique. This technique is similar to the natural process of slopes over-steepening due to scouring erosion or dredging activities.
- Tilting rate (or slope overstepping rate) affects the generation of pore pressure and hence governs the slope instability regime. The instability line is a function of slope increasing rate, i.e. shearing rate.
- A statically liquefied submarine landslide happens in a very short time with no visible precursors long before the failure.
- Coriolis effects during starting of the centrifuge should be taken into account

when testing loose saturated samples. A value of 1% for the ratio of Coriolis acceleration to centrifuge acceleration is suggested.

References

Acosta, E. A., Tibana, S., de Almeida, M. d. S. S., and Saboya Jr, F. (2017). Centrifuge modeling of hydroplaning in submarine slopes. *Ocean Engineering*, 129:451–458.

Andresen, A. and Bjerrum, L. (1968). Slides in subaqueous slopes in loose sand and silt. *Norwegian Geotechnical Institute Publ*.

Arulanandan, K., Thompson, P., Kutter, B., Meegoda, N., Muraleetharan, K., and Yogachandran, C. (1988). Centrifuge modeling of transport processes for pollutants in soils. *Journal of Geotechnical Engineering*, 114(2):185–205.

Askarinejad, A., Beck, A., and Springman, S. M. (2015). Scaling law of static liquefaction mechanism in geocentrifuge and corresponding hydromechanical characterization of an unsaturated silty sand having a viscous pore fluid. *Canadian Geotechnical Journal*, 52(6):708–720.

Askarinejad, A., Zhang, W., de Boorder, M., and van der Zon, J. (2018). Centrifuge and numerical modelling of static liquefaction of fine sandy slopes. *Physical Modelling in Geotechnics*, 2:1119–1124.

Askarinejad, A., Zhang, W., and Maghsoudloo, A. (2019). Physical modelling of static liquefaction of seabed due to scouring.

Biondi, G., Cascone, E., Maugeri, M., and Motta, E. (2000). Seismic response of saturated cohesionless slopes. *Soil Dynamics and Earthquake Engineering*, 20(1-4):209–215.

Bjerrum, L. (1971). Subaqueous slope failures in norwegian fjords. In *Proceedings of the First International Conference on Port and Ocean Engineering Under Arctic Conditions*, pages 24–47. Norwegian Geotechnical Institute Publ.

Boylan, N., Gaudin, C., White, D., Randolph, M., and Schneider, J. (2009). Geotechnical centrifuge modelling techniques for submarine slides. In *ASME 2009 28th International Conference on Ocean, Offshore and Arctic Engineering*, pages 65–72. American Society of Mechanical Engineers Digital Collection.

Byrne, P., Puebla, H., Chan, D., Soroush, A., Morgenstern, N., Cathro, D., Gu, W., Phillips, R., Robertson, P., and Hofmann, B. (2000). Canlex full-scale experiment and modelling. *Canadian geotechnical journal*, 37(3):543–562.

Cargill, K. W. and Ko, H.-Y. (1983). Centrifugal modeling of transient water flow. *Journal of Geotechnical Engineering*, 109(4):536–555.

Chapuis, R. P. (2004). Permeability tests in rigid-wall permeameters: Determining the degree of saturation, its evolution, and its influence of test results. *Geotechnical Testing Journal*, 27(3):304–313.

Company, T. D. C. (2002). Methocel cellulose ethers: Technical handbook.

Coulter, S. and Phillips, R. (2003). Simulating submarine slope instability initiation using centrifuge model testing. In *Submarine Mass Movements and Their Consequences*, volume 19, pages 29–36. Springer, Dordrecht.

De Groot, M., Lindenberg, J., Mastbergen, D., and Van den Ham, G. (2012). Large scale sand liquefaction flow slide tests revisited. pages 1–22.

De Groot, M., Lindenberg, J., Mastbergen, D. R., and Van den Ham, G. A. (2019). Liquefaction flow slides in large flumes. *International Journal of Physical Modelling in Geotechnics*, 19(1):37–53.

De Jager, R. R. (2018). *Assessing Liquefaction Flow Slides: Beyond Empiricism*. Doctoral dissertation, Delft University of Technology.

De Jager, R. R., Maghsoudloo, A., Askarinejad, A., and Molenkamp, F. (2017). Preliminary results of instrumented laboratory flow slides. *Procedia Engineering*, 175:212–219.

Della, N., Arab, A., and Belkhatir, M. (2011). Influence of specimen-reconstituting method on the undrained response of loose granular soil under static loading. *Acta Mechanica Sinica*, 27(5):796.

Dewoolkar, M. M., Ko, H.-Y., Stadler, A. T., and Astaneh, S. (1999). A substitute pore fluid for seismic centrifuge modeling. *Geotechnical Testing Journal*, 22(3):196–210.

Elgamal, A., Yang, Z., Lai, T., Kutter, B. L., and Wilson, D. W. (2005). Dynamic response of saturated dense sand in laminated centrifuge container. *Journal of Geotechnical and Geoenvironmental Engineering*, 131(5):598–609.

Garnier, J., Gaudin, C., Springman, S. M., Culligan, P., Goodings, D., Konig, D., Kutter, B., Phillips, R., Randolph, M., and Thorel, L. (2007). Catalogue of scaling laws and similitude questions in geotechnical centrifuge modelling. *International Journal of Physical Modelling in Geotechnics*, 7(3):1–23.

Goren, L., Aharonov, E., Sparks, D., and Toussaint, R. (2010). Pore pressure evolution in deforming granular material: A general formulation and the infinitely stiff approximation. *Journal of Geophysical Research: Solid Earth*, 115(B09216).

Gu, R. and Dogandžić, A. (2016). Blind x-ray ct image reconstruction from polychromatic poisson measurements. *IEEE Transactions on Computational Imaging*, 2(2):150–165.

Gue, C., Soga, K., Bolton, M., and Thusyanthan, N. (2010). Centrifuge modelling of submarine landslide flows. In Springman, S. M., Laue, J., and Linda, S., editors, *Physical Modelling in Geotechnics (ICPMG 2010)*, volume 2, pages 1113–1118, Zurich, Switzerland. CRC Press.

Gupta, L. P., Tanikawa, W., Hamada, Y., Hirose, T., Ahagon, N., Sugihara, T., Abe, N., Nomura, S., Masaki, Y., and Wu, H. Y. (2018). Examination of gas hydrate-bearing deep ocean sediments by x-ray computed tomography and verification of physical property measurements of sediments. *Marine and Petroleum Geology*.

Higo, Y., Oka, F., Kimoto, S., Sanagawa, T., and Matsushima, Y. (2011). Study of strain localization and microstructural changes in partially saturated sand during triaxial tests using microfocus x-ray ct. *Soils and foundations*, 51(1):95–111.

Ilstad, T., Marr, J. G., Elverhøi, A., and Harbitz, C. B. (2004). Laboratory studies of subaqueous debris flows by measurements of pore-fluid pressure and total stress. *Marine Geology*, 213(1-4):403–414.

Iverson, R. M. (1993). Differential equations governing slip-induced pore-pressure fluctuations in a water-saturated granular medium. *Mathematical geology*, 25(8):1027–1048.

Ko, H. (1994). Modeling seismic problems in centrifuges. In Leung, C. F., Lee, F. H., and Tan, T. S., editors, *Centrifuge 94: proceedings of the International Conference Centrifuge 94*, pages 3–12, Rotterdam. Balkema.

Kraft Jr, L. M., Gavin, T. M., and Bruton, J. C. (1992). Submarine flow slide in puget sound. *Journal of Geotechnical Engineering*, 118(10):1577–1591.

Kramer, S. (1988). Triggering of liquefaction flow slides in coastal soil deposits. *Engineering Geology*, 26(1):17–31. Nature.

Kvalstad, T., Nadim, F., Arbitz, C., et al. (2001). Deepwater geohazards: geotechnical concerns and solutions. In *Offshore Technology Conference*. Offshore Technology Conference.

Kyriakou, Y., Meyer, E., Prell, D., and Kachelrieß, M. (2010). Empirical beam hardening correction (ebhc) for ct. *Medical Physics*, 37(10):5179–5187.

Lade, P. V. (1992). Static instability and liquefaction of loose fine sandy slopes. *Journal of Geotechnical Engineering*, 118(1):51–71.

Lade, P. V. and Yamamuro, J. A. (2011). Evaluation of static liquefaction potential of silty sand slopes. *Canadian Geotechnical Journal*, 48(2):247–264.

Lowe, D. R. (1976). Subaqueous liquefied and fluidized sediment flows and their deposits. *Sedimentology*, 23(3):285–308.

Maghsoudloo, A., Askarinejad, A., De Jager, R., Molenkamp, F., and Hicks, M. (2018). Experimental investigation of pore pressure and acceleration development in static liquefaction induced failures in submerged slopes. In *9th International Conference of Physical Modelling in Geotechnics, London*, volume 2, pages 987–992. CRC Press.

Maghsoudloo, A., Galavi, V., Hicks, M. A., and Askarinejad, A. (2017). Finite element simulation of static liquefaction of submerged sand slopes using a multilaminate model. In *19th International Conference on Soil Mechanics and Geotechnical Engineering*, volume 2, pages 801–804.

Petrovic, A., Siebert, J., and Rieke, P. (1982). Soil bulk density analysis in three dimensions by computed tomographic scanning. *Soil Science Society of America Journal*, 46(3):445–450.

Phillips, R. and Byrne, P. (1995). Modeling flowslides caused by static loading. *Transportation Research Record*, pages 12–21.

Rietdijk, J., Schenkeveld, F., Schaminée, P., and Bezuijen, A. (2010). The drizzle method for sand sample preparation. In Springman, S. M., Laue, J., and Linda, S., editors, *Physical Modelling in Geotechnics (ICPMG 2010)*, volume 1, pages 267–272, Zurich, Switzerland. CRC Pres.

Sadrekarimi, A. (2016). Static liquefaction analysis considering principal stress directions and anisotropy. *Geotechnical and Geological Engineering*, 34(4):1135–1154.

Sassa, S. and Sekiguchi, H. (1999). Wave-induced liquefaction of beds of sand in a centrifuge. *Geotechnique*, 49(5):621–638.

Schofield, A. N. (1980). Cambridge geotechnical centrifuge operations. *Geotechnique*, 30(3):227–268.

Silvis, F. and Groot, M. d. (1995). Flow slides in the netherlands: experience and engineering practice. *Canadian geotechnical journal*, 32(6):1086–1092.

Singh, D. N. and Gupta, A. K. (2000). Modelling hydraulic conductivity in a small centrifuge. *Canadian Geotechnical Journal*, 37(5):1150–1155.

Sladen, J., D'hollander, R., and Krahn, J. (1985). The liquefaction of sands, a collapse surface approach. *Canadian Geotechnical Journal*, 22(4):564–578.

Spence, K. and Guymer, I. (1997). Small-scale laboratory flowslides. *Geotechnique*, 47(5):915–932.

Stewart, D. P., Chen, Y.-R., and Kutter, B. L. (1998). Experience with the use of methylcellulose as a viscous pore fluid in centrifuge models. *Geotechnical Testing Journal*, 21(4):365–369.

Take, W., Bolton, M., Wong, P., and Yeung, F. (2004). Evaluation of landslide triggering mechanisms in model fill slopes. *Landslides*, 1(3):173–184.

Taylor, R. (1995). *Geotechnical centrifuge technology*. Blackie Academic & Professional, Chapman & Hall, London.

Vaid, Y. P., Sivathayalan, S., and Stedman, D. (1999). Influence of specimen-reconstituting method on the undrained response of sand. *Geotechnical Testing Journal*, 22(3):187–195.

Wanatowski, D. and Chu, J. (2012). Factors affecting pre-failure instability of sand under plane-strain conditions. *Géotechnique*, 62(2):121–135.

Wen, C. and Yu, Y. (1966). A generalized method for predicting the minimum fluidization velocity. *AIChE Journal*, 12(3):610–612.

Wood, D. M. (2014). *Geotechnical modelling*. CRC Press.

Yamada, Y., Yamashita, Y., and Yamamoto, Y. (2010). Submarine landslides at subduction margins: insights from physical models. *Tectonophysics*, 484(1-4):156–167.

Yin, M., Rui, Y., and Xue, Y. (2017). Centrifuge study on the runout distance of submarine debris flows. *Marine Georesources & Geotechnology*, pages 1–11.

Zhang, J., Lin, H., and Wang, K. (2015). Centrifuge modeling and analysis of submarine landslides triggered by elevated pore pressure. *Ocean Engineering*, 109:419–429.

Zhang, W. and Askarinejad, A. (2019). Centrifuge modelling of submarine landslides due to static liquefaction. *Landslides*, 16(10):1921–1938.

Zienkiewicz, O. C., Chan, A., Pastor, M., Schrefler, B., and Shiomi, T. (1999). *Computational geomechanics*. John Wiley & Sons, Chichester, New York, Weinheim, Brishane, Singapore, Toronto.

5

Centrifuge modelling of static liquefaction in submarine slopes: the scaling law dilemma

God opposes the proud but shows favour to the humble.

James 4:6, New International Version.

The content of this chapter has been accepted as research paper in Canadian Geotechnical Journal, Zhang and Askarinejad (2020).

5.1. Abstract

The scaling laws for the centrifuge modelling of the initiation and propagation of static liquefaction in submerged slopes are investigated in this paper. A theoretical model is developed to analytically determine the scaling factor of fluid viscosity in simulating the onset of static liquefaction by detailed analysis of the hydro-mechanical processes at the grain scale. Based on this, a fluid with a viscosity of $\sqrt{N}$-times that of water ($\sqrt{N}$-fluid) is suggested, where N is the geometrical scaling factor in centrifuge modelling. A fluid with a viscosity of N-times that of water (N-fluid) was adopted for simulating dynamic events in the centrifuge, which is used and suggested by previous researchers. Centrifuge tests were designed to examine and verify the scaling factors for pore fluid viscosity in simulating the onset of static liquefaction and the post-liquefaction behaviour of subaqueous landslides. These tests were performed at $10g$, $30g$ and $50g$ conditions, with $\sqrt{N}$-fluid, N-fluid or water, where g is the Earth's gravitational acceleration. Results confirm that the correct scaling factors (prototype/model) for pore fluid viscosity are $1/\sqrt{N}$ and $1/N$ for investigating the onset of static liquefaction and the post-failure behaviour of the submarine slopes, respectively.

Key words*: static liquefaction, geotechnical centrifuge modelling, scaling law, submarine slopes*

5.2. Introduction

Subsea slope instabilities could be induced by monotonic loads, such as: rapid accumulation of sediments, erosion and some human activities (Hance, 2003, Locat and Lee, 2002, Ye et al., 2017). The onset of static liquefaction in loose sand is related to the change of soil drainage regime, from drained to temporarily undrained conditions, and the resulting development of excess pore pressure (EPP) due to monotonic loading (Askarinejad et al., 2015, Lade, 1992, Lade and Yamamuro, 2011, Sladen et al., 1985, Take et al., 2004). Centrifuge modelling provides an experimental technique to investigate the triggering mechanisms of static liquefaction (Askarinejad et al., 2015, Take and Beddoe, 2014, Zhang and Askarinejad, 2019). The general physics of soil grains and pore fluid behaviour during porous matrix deformation can be described by mass conservation equations (Goren et al., 2010, Taylor, 2014). The mass conservation for soil grains over a time period (t) is expressed in Equation 5.1,

$$\nabla \cdot \left[(1-n)\rho_{\text{grain}} V_{\text{grain}}\right] + \frac{\partial (1-n)\rho_{\text{grain}}}{\partial t} = 0 \tag{5.1}$$

where, n is the soil porosity; ρ_{grain} is the grain density; V_{grain} is the grain velocity vector. The pore fluid mass conservation equation can be demonstrated in Equation 5.2,

$$\nabla \cdot (n\rho_{\text{f}} V_{\text{f}}) + \frac{\partial n\rho_{\text{f}}}{\partial t} = 0 \tag{5.2}$$

where, ρ_{f} is the pore fluid density; V_{f} is the pore fluid velocity which is shown in Equation 5.3.

$$nV_{\text{f}} = nV_{\text{grain}} - q \tag{5.3}$$

The specific pore fluid discharge, q, given by Darcy's law (Darcy, 1856, Taylor, 2014, Verruijt and Van Baars, 2007) is shown in 5.4,

$$q = \frac{\kappa}{\mu}\nabla(\Delta p) \text{ with } \Delta p = \Delta h_{\text{h}}\gamma_{\text{f}} \tag{5.4}$$

where, κ is the intrinsic permeability; μ is the fluid dynamic viscosity; Δp represents the pore pressure or energy difference and $\nabla(\Delta p)$ denotes the pressure or energy gradient; Δh_{h} is the hydraulic head difference over a certain length inside the porous medium; γ_{f} is the fluid unit weight. The pore pressure in a soil matrix is related to the development of excess pore pressure (EPP), thus it depends on the triggering mechanism that generates the EPP.

Centrifuge modelling techniques have been used to investigate the triggering mechanisms of static liquefaction (Askarinejad et al., 2015, Take and Beddoe, 2014, Zhang and Askarinejad, 2019). Due to the complexity of the soil-fluid system, a consensus on the triggering mechanism of static liquefaction has not been agreed upon yet between the researchers who has investigated this phenomenon. To the authors' knowledge, the first centrifuge tests to simulate static liquefaction of submerged slope were carried out as part of the CANLEX program (Phillips and Byrne,

1995). Monotonic loads were applied on the slope crests by dropping steel blocks to trigger static liquefaction flow. These tests were performed at $50g$, and the samples were saturated with Canola vegetable oil with a dynamic viscosity of approximately 50 times that of water. Moreover, the pore pressure accumulation effect on marine landslides due to gas hydrate dissociation was investigated by Zhang et al. (2015) using a geotechnical centrifuge at $50g$. Water was used as the pore fluid with the assumption that the soil material (clay) in the model represented a prototype soil with a permeability 50 times higher. Several centrifuge model tests were performed at HKUST to simulate static liquefaction of loose sandy slopes (with a slope angle of 30°) induced by the mechanism of rising ground water table and rainfall (Ng, 2014, Zhang, 2006). Zhang (2006) mentioned that fluid that is N times more viscous than water should be used in the tests, although, due to practical reasons, water was used instead.

Take et al. (2004) simulated rainfall-induced unsaturated slope failures and proposed that the collapse of soil voids could result in the build up of transient pore water pressure. They used water as the pore fluid in the centrifuge tests and concluded that the difference in the scaling factors applied to the time duration for the generation of pressure pulse due to the soil voids collapse and for the dissipation of induced pore pressure was the reason that static liquefaction was not triggered in their centrifuge models. Therefore, in order to simulate static liquefaction of subaqueous slopes, it is essential to investigate the pore-fluid interaction response to soil matrix deformation caused by monotonic loads at the grain scale.

Askarinejad et al. (2015) hold the same opinion and further propose that attentions should be paid onto the grain scale as voids collapse initiates locally at a scale of a small pack of grains. They have investigated the gravitational falling of a sand particle and pore fluid dissipation theoretically at the grain scale. They believe that $\sqrt{N}$-fluid should be used in centrifuge tests on N-times scaled down models in order to simulate the onset of static liquefaction at an acceleration field of Ng. However, the derivation of this scaling factor is limited to the unsaturated condition. Accordingly, for simulating static liquefaction of underwater slopes which is under fully saturated conditions, the triggering mechanism and the scaling factor for pore fluid viscosity need to be studied.

This paper aims at presenting an understanding of scaling laws for the onset of static liquefaction in centrifuge modelling. Once seabed static liquefaction happens, the post-liquefaction behaviour and its influence on surrounding structures is of interest in practical engineering. Several researchers have experimentally confirmed that a fluid with a viscosity N-times higher than that of water (prototype pore fluid) should be used in order to study dynamic processes in a centrifuge including liquefaction induced by earthquakes and waves, and debris flows (e.g. Arulanandan et al., 1988, Bowman et al., 2010, Cargill and Ko, 1983, Garnier et al., 2007, Singh and Gupta, 2000, Taylor, 1995). The post-liquefaction of saturated sand layer initiated by monotonic loads is similar to seismic-induced liquefaction and debris flows, as all these events include dynamic interaction between grains and fluid along with the generation and dissipation of pore pressure. Hence, the scaling factor with a value of N for pore fluid viscosity was adopted. The validity of the scaling laws for

both the onset of static liquefaction and post-liquefaction is checked by conducting centrifuge tests at three different acceleration fields. These tests have been conducted using the geo-centrifuge at TU Delft which is equipped with a tilting system designed for controlled triggering of static liquefaction in submerged slopes. Three types of pore fluid were applied, namely water, N-fluid and $\sqrt{N}$-fluid.

In this paper, firstly, a triggering mechanism of pore pressure development for saturated soil material during deformation induced by monotonic loads is presented; secondly, the derivation of the scaling factor for pore fluid viscosity for simulating the onset of static liquefaction is illustrated; and lastly, the results of centrifuge tests are discussed in terms of slope failure angle, development of liquefaction and generated EPP (ratios) as verifications for the developed theoretical model.

5.3. The scaling law for pore fluid viscosity at the onset of static liquefaction

5.3.1. General equation for simulating deformation of saturated granular material in centrifuge

The schematic sketches in Figure 5.1a and Figure 5.1b demonstrate the deformation of a loosely packed saturated granular matrix due to shear force in a drained condition. At the beginning, the sand grains move with a velocity of V_{grain} during shearing ($V_{\text{grain,x}}$ and $V_{\text{grain,x}}^{undrained}$ are the sand grains velocity in the x direction under drained and undrained drainage conditions, respectively). During this stage, pore fluid could drain freely, and the pore pressure generation rate ($\dot{\text{GPP}}$) is smaller than the pore pressure dissipation rate ($\dot{\text{DPP}}$), i.e. there is no EPP being generated. The sand grains and pore fluid behaviour during this process can be classically described by Equations 5.1 and 5.2. Assuming the sand grain density and pore fluid density are constant, Equations 5.1 and 5.2 can be rewritten as Equations 5.5 and 5.6. Equations 5.3, 5.4 and 5.6 lead to a general mass conservation equation as shown in Equation 5.7.

$$\nabla \cdot V_{\text{grain}} = \frac{1}{(1-n)}\left[\frac{\partial n}{\partial t} + V_{\text{grain}}\nabla n\right] \tag{5.5}$$

$$\nabla \cdot (nV_{\text{f}}) + \frac{\partial n}{\partial t} = 0 \tag{5.6}$$

$$\nabla \cdot (nV_{\text{grain}}) - \nabla \cdot \left[\frac{\kappa}{\mu}\nabla(\Delta p)\right] + \frac{\partial n}{\partial t} \tag{5.7}$$

Equation 5.7 can be written as Equation 5.8 and be further simplified as Equation 5.9 by only considering the grain and fluid movement in the x direction shown in Figure 5.1 for the sake of clarity, where C_{x} is a constant in the range from 0 to 1.

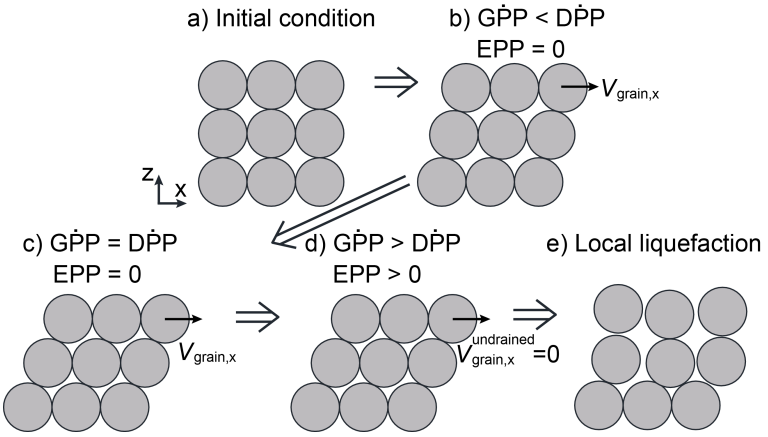

Figure 5.1: Schematic illustration of soil and pore fluid behaviour in loose porous matrix during deformation: a) initial soil structure before deformation; b) when the generated pore fluid can fully dissipate in response to the reduction of pore volume under drained condition; c) the moment when GṖP equals to DṖP while the sand grains still have the potential to move; d) shortly after previous stage, the grain velocity reduces to zero and EPP develops under (partially) undrained condition as the locally trapped pore fluid resists further reduction of pore volume size, hence it prevents the movement of sand grains; e) local liquefaction due to the build-up of EPP which might further lead to the sample liquefaction

5

$$\frac{\partial(nV_{\mathrm{grain,x}})}{\partial x}+\frac{\partial(nV_{\mathrm{grain,y}})}{\partial y}+\frac{\partial(nV_{\mathrm{grain,z}})}{\partial z}-\frac{1}{\mu}\left[\kappa\left(\frac{\partial^2\Delta p}{\partial x^2}+\frac{\partial^2\Delta p}{\partial y^2}+\frac{\partial^2\Delta p}{\partial z^2}\right)+\frac{\partial\kappa}{\partial x}\frac{\partial\Delta p}{\partial x}+\frac{\partial\kappa}{\partial y}\frac{\partial\Delta p}{\partial y}+\frac{\partial\kappa}{\partial z}\frac{\partial\Delta p}{\partial z}\right]+\frac{\partial n}{\partial t}=0 \quad (5.8)$$

$$\frac{\partial(nV_{\mathrm{grain,x}})}{\partial x}-\frac{1}{\mu}\left[\kappa\left(\frac{\partial^2\Delta p}{\partial x^2}\right)+\frac{\partial\kappa}{\partial x}\frac{\partial\Delta p}{\partial x}\right]+C_{\mathrm{x}}\frac{\partial n}{\partial t}=0 \quad (5.9)$$

Equation 5.9 generally describes mass conservation for sand grains and pore fluid in a deforming soil matrix, hence, it is valid both in prototype and model. Equation 5.9 can be expressed as Equation 5.10 and Equation 5.11 for prototype and model, respectively. Equation 5.10 can be further rewritten as Equation 5.12, where * determines the scaling ratio of prototype to model.

$$\frac{\partial(n_{\mathrm{p}}V_{\mathrm{grain,x,p}})}{\partial x_{\mathrm{p}}}-\frac{1}{\mu_{\mathrm{p}}}\left[\kappa_{\mathrm{p}}\left(\frac{\partial^2\Delta p_{\mathrm{p}}}{\partial x_{\mathrm{p}}^2}\right)+\frac{\partial\kappa_{\mathrm{p}}}{\partial x_{\mathrm{p}}}\frac{\partial\Delta p_{\mathrm{p}}}{\partial x_{\mathrm{p}}}\right]+C_1\frac{\partial n_{\mathrm{p}}}{\partial t_{\mathrm{p}}}=0 \quad (5.10)$$

$$\frac{\partial(n_{\mathrm{m}}V_{\mathrm{grain,x,m}})}{\partial x_{\mathrm{m}}}-\frac{1}{\mu_{\mathrm{m}}}\left[\kappa_{\mathrm{m}}\left(\frac{\partial^2\Delta p_{\mathrm{m}}}{\partial x_{\mathrm{m}}^2}\right)+\frac{\partial\kappa_{\mathrm{m}}}{\partial x_{\mathrm{m}}}\frac{\partial\Delta p_{\mathrm{m}}}{\partial x_{\mathrm{m}}}\right]+C_1\frac{\partial n_{\mathrm{m}}}{\partial t_{\mathrm{m}}}=0 \quad (5.11)$$

$$\left(\frac{n^* V^*_{\text{grain,x}}}{x^*}\right)\frac{\partial(n_{\text{m}} V_{\text{grain,x,m}})}{\partial x_{\text{m}}} - \left(\frac{\kappa^* \Delta p^*}{\mu^* (x^*)^2}\right)\frac{1}{\mu_{\text{m}}}\left[\kappa_{\text{m}}\left(\frac{\partial^2 \Delta p_{\text{m}}}{\partial x_{\text{m}}^2}\right) + \frac{\partial \kappa_{\text{m}}}{\partial x_{\text{m}}}\frac{\partial \Delta p_{\text{m}}}{\partial x_{\text{m}}}\right] + \left(\frac{n^*}{t^*}\right) C_1 \frac{\partial n_{\text{m}}}{\partial t_{\text{m}}} = 0 \quad (5.12)$$

By comparing Equation 5.12 with Equation 5.11, it can be therefore concluded that Equation 5.13 should be guaranteed in order to simulate loosely packed soil under monotonic shear load in a centrifuge.

$$\frac{n^* V^*_{\text{grain,x}}}{x^*} = \frac{\kappa^* \Delta p^*}{\mu^* (x^*)^2} = \frac{n^*}{t^*} \quad (5.13)$$

If the soil in the centrifuge model is the same as that in the prototype, then $n^* = \kappa^* = 1$, and Equation 5.13 becomes Equation 5.14.

$$\frac{V^*_{\text{grain,x}}}{x^*} = \frac{\Delta p^*}{\mu^* (x^*)^2} = \frac{1}{t^*} \quad (5.14)$$

5.3.2. Triggering mechanism at the onset of static liquefaction

During the process of shearing caused by an external monotonic load, a loose soil tends to contract under a drained condition. However, at a certain stage (Figure 5.1c, as a result of voids contraction, $\dot{\text{GPP}}$ becomes equal to $\dot{\text{DPP}}$ at a local zone in the sand layer. Due to inertia, the grains tend to keep on moving forward with a velocity of V_{grain}, i.e. the pore volume tends to decrease further. The balance between the generation and dissipation of pore pressure is suddenly broken, due to further minor changes in soil fabric. The drainage condition may transform to partially drained or even undrained condition, and $\dot{\text{GPP}}$ becomes higher than $\dot{\text{DPP}}$, as demonstrated in Figure 5.1d. Since the pore fluid cannot flow out freely from the contracting void, the pore fluid would prevent soil contraction (i.e. grain movements) under (partially) undrained condition. Thus, in a short period, the grain velocity ($V_{\text{grain}}^{\text{undrained}}$) approaches zero. Due to the grain-fluid interaction, EPP would be generated at a much higher rate than before, which would result in an increase in shear stress ratio as the mean effective stress reduces and the shear stress remains nearly constant. This could potentially lead to static liquefaction (Figure 5.1e).

Equation 5.15 shows Newton's second law Stronge (2018), where F represents force, m is mass, a is acceleration and V denotes velocity. Based on Newton's second law, a certain force would be applied on the pore-fluid interface ($F_{\text{grain-fluid}}^{\text{impulse}}$) in the process shown in Figure 5.1c and Figure 5.1d. In the x direction, if the net force $F_{\text{grain-fluid}}^{\text{impulse}}$ is constant at a time interval of dt, the momentum of the grains changes by an amount expressed by Equation 5.16, where dt represents the kinematic time interval and m_{grain} is the sand grain mass.

$$F = ma = m\frac{dV}{dt}, i.e.\ Fdt = m\ dV \tag{5.15}$$

$$F^{\text{impulse}}_{\text{grain-fluid}}dt = m_{\text{grain}}(V_{\text{grain,x}} - V^{\text{undrained}}_{\text{grain,x}}) = m_{\text{grain}}V_{\text{grain,x}} \tag{5.16}$$

Take et al. (2004) proposed that the increase of pore pressure due to the collapse of saturated voids locally can be a possible triggering mechanism of static liquefaction. Askarinejad et al. (2015) proposed the grain scale analysis method for deriving the scaling factor for pore fluid viscosity in the case of rainfall-induced static liquefaction in an unsaturated silty sand layer. The grain-scale analysis method assumes that the clollapse of sand voids is the internal mechanism leading to static liquefaction. It also assumes that the scaling factor for dimensions, such as length (L), is 1 as expressed in Equation 5.17, if the prototype soil structure is similarly reproduced in the model using the same soil material.

$$x^* = \Delta L^* = 1 \tag{5.17}$$

5

The proposed hypothesis on the triggering mechanism of liquefaction of saturated sand due to a monotonic increase of shear stresses is also based on the assumption that the collapse of sand voids is the internal mechanism, as illustrated in Figure 5.1. Hence the grain-scale analysis method is adopted in this study.

The scaling factor for time, t^*, can be obtained from the dimensional analysis of centrifugal acceleration (a) which has a unit of length divided by square of time (L/t^2) as illustrated in Equation 5.18. Hence, it can be concluded that the scaling factor for time is $\sqrt{N}$.

$$a^* = \frac{a_{\text{p}}}{a_{\text{m}}} = \frac{L_{\text{p}}}{(t_{\text{p}})^2}\frac{(t_{\text{m}})^2}{L_{\text{m}}} = \left(\frac{1}{t^*}\right)^2 = 1/N \rightarrow t^* = \sqrt{N} \tag{5.18}$$

The dimensional analysis of velocity which has a unit of length divided by the kinematic time (L/t) yields a scaling factor of $1/\sqrt{N}$ for the grain velocity ($V^*_{\text{grain,x}}$), as expressed in Equation 5.19.

$$V^*_{\text{grain,x}} = \frac{L_{\text{p}}}{t_{\text{p}}}\frac{t_{\text{m}}}{L_{\text{m}}} = \frac{1}{t^*} = \frac{1}{\sqrt{N}} \tag{5.19}$$

If the soil material in the model and prototype is the same, the scaling factor of soil mass is unity (Equation 5.20).

$$m^*_{\text{grain}} = \frac{m_{\text{grain,p}}}{m_{\text{grain,m}}} = 1 \tag{5.20}$$

Substituting Equations 5.18 - 5.20 into Equation 5.16 yields a scaling factor of $1/N$ for the induced force in-between the grain and pore fluid (Equation 5.21).

$$F^{\text{impulse},*}_{\text{grain-fluid}} = \frac{m^*_{\text{grain}}V^*_{\text{grain}}}{t^*} = \frac{1}{N} \tag{5.21}$$

The generated pore pressure equals the pressure acting on the grain, hence the scaling factor for excess pore pressure (Δp^*) is $1/N$ as illustrated in Equation 5.22,

$$\Delta p^* = \frac{F^{\text{impulse},*}_{\text{grain-fluid}}}{A^*_{\text{grain}}} = \frac{1}{N} \text{ with } A^*_{\text{grain}} = 1 \tag{5.22}$$

where A^*_{grain} is the scaling factor for the contacting area between the grain and pore fluid, which equals one at the grain scale.

Substituting Equations 5.17, 5.18, 5.19 and 5.22 into Equation 5.14 yields that the pore fluid dynamic viscosity in the model should be $\sqrt{N}$ times of that in the prototype, as shown in Equation 5.23.

$$\mu^* = \frac{\Delta p^* t^*}{(x^*)^2} = \frac{\Delta p^*}{x^* V^*_{\text{grain}}} = \frac{1}{\sqrt{N}} = \frac{\mu_{\text{p}}}{\mu_{\text{m}}} \tag{5.23}$$

5

5.4. Centrifuge modelling of static liquefaction at various centrifugal accelerations

5.4.1. Testing method

A novel strong box with an integrated tilting system was designed for triggering static liquefaction in loose sand layers. The test setup is illustrated in Figure 5.2. One side of the strongbox can be lifted up by the linear actuator (Linak 282100-40150100), and the sample is tilted around the centre of the rotation axis. Hence, the gradual steepening of sea floor can be simulated. The applicable tilting rate (TR) ranges from 0.1°/sec to 2.0°/sec with a precision of 0.002°/sec at model scale. The maximum slope angle that could be reached is 20°. Moreover, three pore pressure transducers (PPTs, MPXH6400A) were placed at the sample base, as illustrated in Figure 5.3, to monitor the pore pressure development during testing.

In this study, a linear potentiometer (item number 10 in Figure 5.2a) was fixed to the tilting frame on the top (point A) and had a ball connection at the tip (point C). Hence, both lines BA and BC in Figure 5.2b are fixed throughout the tests, which denote the distances from the centre of the rotation axis (point B) to the top and to the tip of the linear potentiometer, respectively. The change in the length of line AC can be indicated by the readings from the linear potentiometer which is related to the change in angle ABC and hence in slope inclination.

Initially all the prepared samples had an inclination of zero degree as the tilting frame was kept flat. The centrifuge carrier has a hinge connection to the horizontal beam of the centrifuge as shown in Figure 4.13. Hence, the resultant acceleration (due to the centrifugal acceleration and Earth's gravity) was always perpendicular to the surface of each sample in-flight before tilting. The hinge of the centrifuge has been maintained regularly, therefore, the effect of hinge friction in centrifuge carrier inclination is regarded as minimal.

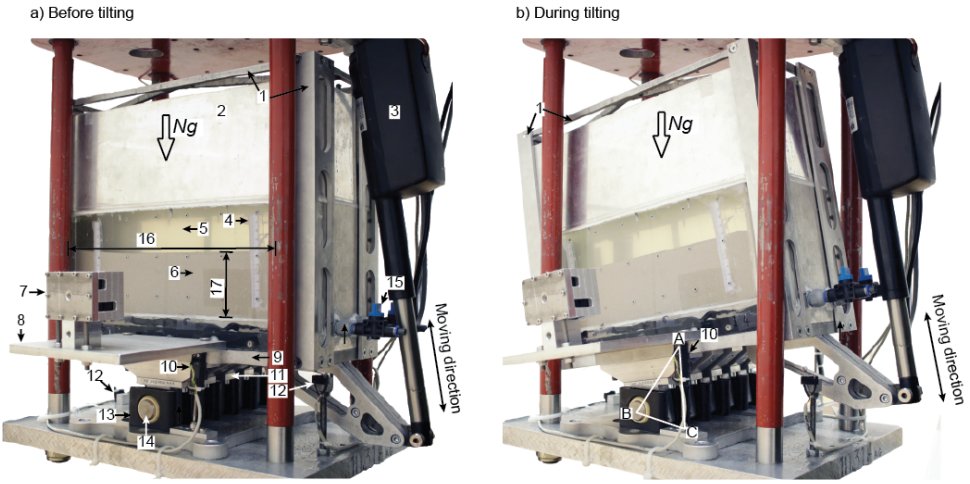

Figure 5.2: Test set-up in the centrifuge carrier (after Zhang and Askarinejad, 2019): 1) outer frame; 2) extension box; 3) linear motor; 4) scale; 5) fluid; 6) submerged sand; 7) high resolution, high speed camera; 8) camera holder; 9) base plate; 10) linear potentiometer; 11) bearing blocks; 12) switches; 13) shaft blocks; 14) rotation axis; 15) valves; 16) sample length: 355 mm (model scale); 17) sample height

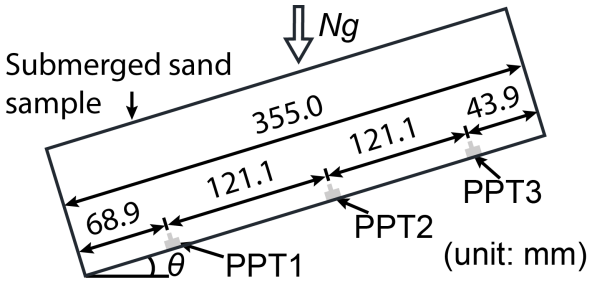

Figure 5.3: Schematic illustration of PPTs in a sample with a slope angle of θ (model scale) Test scenarios

5.4.2. Soil material and pore fluid

Geba Sand was used as the soil material in this paper, which has been characterised by De Jager (2018), Askarinejad et al. (2018) and Maghsoudloo et al. (2018). The material is fine, sub-angular and sub-rounded sand, with D_{10} = 0.078 mm, D_{30} = 0.108 and D_{60} = 0.121 mm, where D_{10}, D_{30} and D_{60} are the grain diameters at 10%, 30% and 60% passing, respectively. The internal friction angle is 34°. The minimum and maximum void ratios, $e_{\min}$ and $e_{\max}$ are 0.64 and 1.07, respectively. The sand has a specific gravity (G_s) of 2.67. It is determined that the intrinsic permeability, κ, is about 4.3 x 10^{-12} m^2 when Dr is approximately 30% at $1g$ (Krapfenbauer, 2016).

In this study, viscous fluids with six different viscosities were prepared with Hydroxypropyl Methylcellulose (HPMC) powder, which has been widely applied in

centrifuge models (Stewart et al., 1998). The adopted fluid preparation technique was explained in Chapter 4. The fluid dynamic viscosities were selected based on the scaling laws for pore fluid and testing g-levels, which are listed in Table 5.1. The viscous fluid density, ρ_{f}, is assumed to be equal to the water density as all of the applied concentrations of HPMC powder are less than 1% (Stewart et al., 1998).

5.4.3. Test scenarios

In order to validate the proposed scaling laws for simulating both the onset of static liquefaction (Equation 5.23) and post liquefaction in centrifuge, three centrifugal accelerations ($10g$, $30g$ and $50g$) and two types of viscous fluids (N-fluid tests and $\sqrt{N}$-fluid) were adopted as shown in Table 5.1. Besides, a test with water as the submerging fluid was performed at $10g$ also to investigate the fluid viscosity effect on the onset of static liquefaction. During a centrifuge test, the g-level varies with the sample depth following a second order polynomial. In order to minimise the error in stress distribution due to this effect, the effective centrifuge radius is defined as from the centrifuge central axis to $1/3H_{\mathrm{s,1g}}$ as suggested by Taylor (2014), where $H_{\mathrm{s,1g}}$ is sample height. In this study, the maximum error in the stress profile is less than 2%.

The samples were tilted at a controlled TR as shown in Figure 5.2. The adopted tilting rate was 0.1°/sec at model scale (TR_{m}) in this study. The corresponding tilting rate at prototype will be N times smaller than that at model scale as explained in Chapter 4, i.e. $TR_{\mathrm{p}} = TR_{\mathrm{m}}/N$. The same sample preparation method was followed and a similar amount of sand was used, so all the samples have a similar height ($H_{\mathrm{s,1g}}$) initially after sample preparation. The slope angles at the onset of static liquefaction (θ_{f}) and the relative densities after sample preparation (Dr_{1g}) and at Ng (Dr_{Ng} , where N is 10, 30 and 50, hereinafter) are included in Table 5.1 as well. Both Dr_{1g} and Dr_{Ng} are the average relative density of the whole samples calculated from the sample heights (i.e. total sample volumes). Due to the enhanced stress levels, the samples have been consolidated differently, hence Dr_{Ng} is larger than Dr_{1g} and their difference gets larger as the g-level increases.

5.4.4. Similarities between samples at three g-levels

Figure 5.4 schematically illustrates three samples with the same height ($H_{\mathrm{s,m}}$, at model scale) and the corresponding stress distribution profiles along the sample height at three different g-levels, namely $10g$, $30g$ and $50g$. ρ' denotes the average buoyancy density which varies with testing g-levels. It can be concluded that the sand layer heights in prototype represented by the three samples have a relationship of $H_{\mathrm{s,10g,p}} \approx 1/3H_{\mathrm{s,30g,p}} \approx 1/5H_{\mathrm{s,50g,p}}$, where the subscripts $10g$, $30g$ and $50g$ denote the testing g-levels. Accordingly, in the view of the stress distribution profiles, the entire $10g$ sample is similar to around 1/3 depth of the $30g$ sample and is similar to about 1/5 depth of the $50g$ sample from top, as shown in Figure 5.4. These layers are named as ”comparable layers” hereafter.

In this study, loose saturated samples were prepared using the fluidization technique. Chapter 4 shows the relative density distribution of a sample prepared with this technique on the computed tomography (CT) scanner table. It is concluded

Table 5.1: Summary of centrifuge tests

Test name[a]	TR_{p} (°/sec)	g-level (g)	μ (cP)	$Dr_{1\mathrm{g}}$ (%)	Dr_{Ng} (%)	$H_{\mathrm{Ng,p}}$ (m)	θ_{f} (°)
W_$10g$	0.01	10	1.0	28	41	1.04	-
V_$\sqrt{N}$_$10g$	0.01	10	3.2	23	32	0.83	17.7
V_N_$10g$	0.01	10	8.5	28	40	0.79	16.2
V_N_$10g^{+}$	0.01	10	8.5	24	38	0.82	14.3
V_$\sqrt{N}$_$30g$	0.003	30	5.5	28	45	2.68	17.2
V_$\sqrt{N}$_$30g^{+}$	0.003	30	5.5	29	46	2.66	18.5
V_N_$30g$	0.003	30	30	25	49	2.53	10.5
V_N_$30g^{+}$	0.003	30	30	33	49	2.51	10.8
V_$\sqrt{N}$_$50g$	0.002	50	7.0	28	52	4.24	16.3
V_N_$50g$	0.002	50	50	33	54	4.12	10.1

[a]: W stands for de-aired water; V stands for viscous fluid; $10g$, $30g$ and $50g$ represent the testing g-levels; $^{+}$ denotes a repeated test.

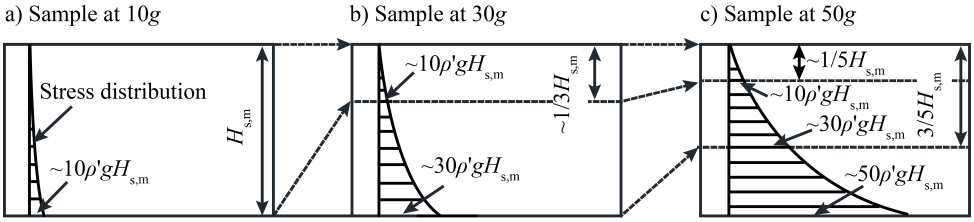

Figure 5.4: Stress distribution of samples tested at $10g$, $30g$ and $50g$ with the same sample height at model scale, i.e. $H_{\mathrm{s},10\mathrm{g,m}} = H_{\mathrm{s},30\mathrm{g,m}} = H_{\mathrm{s},50\mathrm{g,m}}$

that the relative density distribution over sample depth before the spin-up of the centrifuge is characterized by a thin loose top layer with Dr ranging from 15% to 31% and a major uniform soil layer below with Dr around 31%. However, the prepared samples densify upon centrifuge spin-up. The top soil densifies more than the soil layer below due to the looser structure. Thus, the variation in Dr in the top layer after spin-up is believed to be less than that at the $1g$ condition resulting in a more uniform sample at the target g-levels.

An initially loose sandy sample will be densified upon increase in the centrifugal acceleration to lesser degree in the top layer compared with the lower layers (i.e. stress densification effect). This response is due to the non-linear stress profile along the sample depth. Byrne et al. (2004) proposed that the resultant relative density of an initially uniform sample prepared by the dry pluviation method has an approximately linear relationship with the square root of the vertical effective stress, as explained in the following equation, where Dr_0 is the initial relative density at 0 kPa, C_{Dr} is a constant factor related to sand properties including Dr_0, $e_{\max}$, $e_{\min}$ and sand stiffness, σ'_{v} is the vertical effective stress and Pa is atmospheric pressure.

$$Dr = Dr_0 + C_{\mathrm{Dr}} \sqrt{\frac{\sigma'_{\mathrm{v}}}{Pa}} \tag{5.24}$$

However, the sand grain structures in a sample prepared by the fluidization method can be more compressible than a sample built up by the dry pluviation method. In the former method, the sand particles suspense in the fluid with the supplied fluid pressure and then fall down under the effect of gravity. The formation of the sample is similar to that of natural sediment deposits in coastal areas.

As it is shown in Table 5.1, the average relative densities for the samples at $10g$, $30g$ and $50g$ are 38%, 47% and 53%, respectively. The intrinsic permeability can be estimated from Equation 5.25 proposed by Chapuis (2004) based on the Kozeny-Carman equation (Carman, 1939) for sand, where C_{sand} is a factor of sand grain diameter and shape and tortuosity of channels which is approximately 1.0 x 10^{-11} m^2 in this study.

$$\kappa = C_{\mathrm{sand}} \frac{e^3}{(1+e)} \tag{5.25}$$

The difference in the sample densities and Equation 5.25 yields that the maximum difference in κ in the prototypes of three types of samples is less than 17%, which is approximately equivalent to the accuracy of the measurements for a loose sand packing therefore, the difference in κ between various samples can be regarded as minimal. Note that values of Dr_{NG} in Table 5.1 represent the average relative densities of the whole samples.

The theory of "modelling of models" has been assumed to be valid in the three tests summarised in Figure 5.4, if one considers the similarity of stress distribution in the "comparable layers" and if liquefaction initiates within these layers. It is reported in Chapter 4 that the loose sand samples failed originally from the top of the layer, which is also observed in this series of tests as explained in the next section. It can be inferred that the top sand layer is the most critical part in the slope and dominates the initiation of liquefaction when the seabed slope inclination (i.e. shear stress) gradually increases. However, this assumption might be limited by the possible boundary effects especially at the sand layer base which is discussed afterwards.

5.5. Results and discussions

As listed in Table 5.1, in total, seven types of centrifuge tests were conducted at three different g-levels with water and two types of viscous fluid as the submerging fluid, i.e. $\sqrt{N}$-fluid and N-fluid. Figure 5.4 shows that, for each type of submerging fluid, the sample tested at $50g$ can serve as the prototype of the ones conducted at $10g$ and $30g$. Therefore, it can be assumed that the soil-fluid behaviour should be similar for all the tests at various g-levels if an appropriate scaling factor for pore fluid viscosity is applied (Schofield, 1980, Taylor, 1995). Since the onset of static liquefaction can be indicated by the sample failure angles, it can

be expected that the failure angles for $\sqrt{N}$-fluid tests should be similar according to Equation 5.23.

Furthermore, the image analysis results indicate that the liquefaction initiated at the sample surface and propagated downwards to the base of the layer. Details are discussed in following sections. The downward propagation of the liquefied zone and the magnitude of the generated EPP are governed by the post-failure dynamic behaviour of the liquefied soil. Hence, the similarities in these two factors can be used to examine the scaling factor for the pore fluid viscosity in simulating the post-liquefaction behaviour. Therefore, the details of sample failure angles, development of liquefied sand layer and EPP ratios are discussed below.

5.5.1. Failure angles

The test with water as the pore fluid, W_$10g$, did not fail before reaching the maximum slope angle, 20°. It is expected that failure of a similar sample at $30g$ and $50g$ will not happen either, considering the hypothesis developed based on Figure 5.4. Comparing the failure angles of W_$10g$ (larger than 20°), V_$\sqrt{N}$_$10g$ (17.7°) and V_N_$10g$ (16.2°), it appears that a higher fluid viscosity results in a lower failure angle, i.e. a higher potential of static liquefaction. This phenomenon can be seen in Figure 5.5 as well, which shows the angles at the onset of liquefaction for all the centrifuge tests. At the same g-level, the N-fluid tests failed earlier than $\sqrt{N}$-fluid tests. A higher fluid viscosity reduces the capability of fluid dissipation, and thus boosts the process of changing soil drainage regime from drained to undrained conditions.

Figure 5.5 demonstrates similar failure angles for $\sqrt{N}$-fluid tests. However, the failure angles for N-fluid tests are not comparable and decrease with increasing g-level. The agreement in the failure angles for $\sqrt{N}$-fluid tests proves that the appropriate scaling factor for pore fluid dynamic viscosity in case of simulating the onset of static liquefaction should be $\sqrt{N}$. According to Equations 5.4, the application of N-fluid would reduce the discharge $\sqrt{N}$ times more than the one given by $\sqrt{N}$-fluid. Hence, fluid discharge difference between an N-fluid test and a $\sqrt{N}$-fluid test is increasingly prominent with the increasing value of N. This can explain the dependency of failure angles on g-levels for N-fluid tests.

Furthermore, the consistency in failure angles for the tests which were repeated confirms that the testing system is able to produce repeatable results. Thus, for the sake of simplicity, only one of the tests with a repetition is presented and discussed in the following sections.

5.5.2. Development of liquefaction

During the centrifuge tests, high resolution images were captured from the side transparent window of the box at a frame rate of 30 fps (model scale). By comparing the last frame captured before the onset of the flow slide (frame_0) with the first and second frames (frame_1 and frame_2) after the failure, the development of the liquefied zones could be visualised. The results of this image analysis in terms of the extent of the liquefied zone at each time are summarised in Figure 5.6. The subfigures in Figure 5.6 show the soil status before failure. The deeper line in each

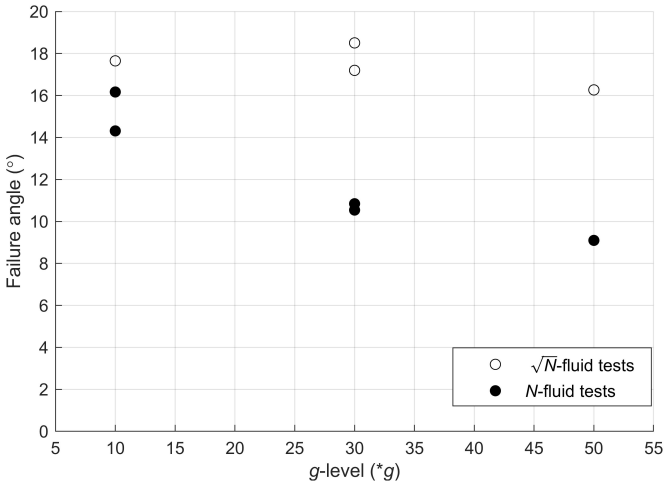

Figure 5.5: Failure angles of centrifuge tests at various g-levels

subfigure roughly represents the largest extent of the liquefied zone. All samples liquefied suddenly, and no visible precursor could be found before liquefaction.

The results indicate that the failure of each sample initiated at the top layer and propagated towards the base. This phenomenon is similar to the results of Byrne et al. (2004), Steedman et al. (2000) and Gonzalez et al. (2002) who designed several centrifuge model tests to evaluate liquefaction response of sandy samples under cyclic loads. Byrne et al. (2004) hypothesised that this observation is dominated by the stress densification effect which would result in a looser surface layer and a relatively dense layer at base at the testing centrifugal acceleration condition. The top layer is, thus, more compressible than the base layer which is beneficial to the accumulation of excess pore pressure, i.e. liquefaction, during tilting/shearing.

The shape of the liquefied layers in Figure 5.6 shows that all the failure zones have a flat section in the middle (far from the longitudinal boundaries) which is parallel to the sand surface before failure. This is in agreement with the pattern of slide surface of a submarine landslide which is generally parallel to the seabed (Ye et al., 2017).

Table 5.2 summaries the downward liquefaction propagation rates, at prototype scale. A constant liquefaction propagation rate can be found for the N-fluid tests. This rate has been determined to be 1.1 m/s on average. However, the liquefaction propagation rate for the $\sqrt{N}$-fluid tests does not show a constant value. Considering the theory of ”modelling of models” (Schofield, 1980), only if an appropriate scaling law for pore fluid is applied can models tested at different g-levels represent similar prototype behaviour. Hence, it can be inferred that a fluid that is N-times more viscous than water should be used for simulating the propagation of liquefaction, which is a dynamic process.

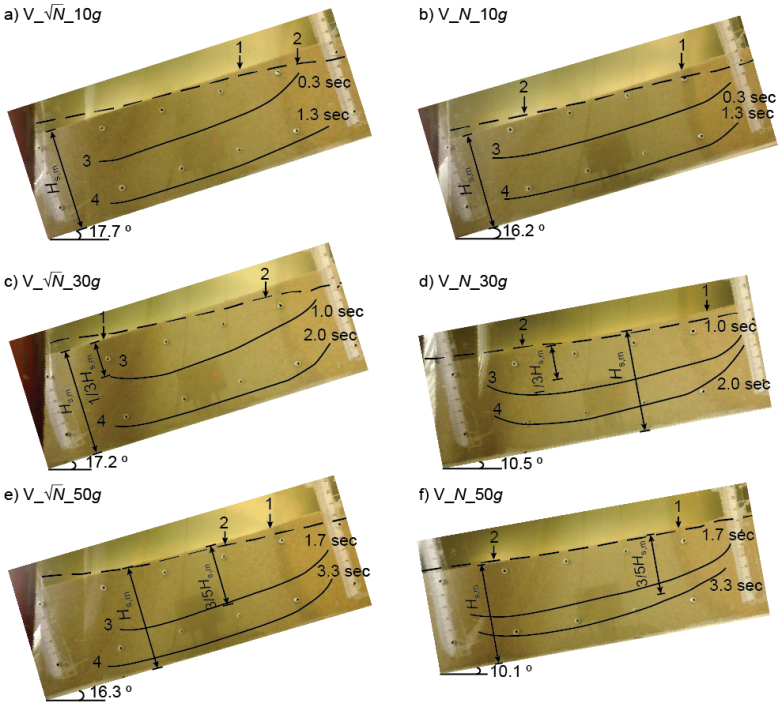

Figure 5.6: Development of failure surfaces for tests at three g-levels with N-fluid and $\sqrt{N}$-fluid (time is expressed at prototype scale): 1) sand surface before failure; 2) sand surface after failure; 3) failure surface from frame_1; 4) failure surface from frame_2

Table 5.2: Propagation rates of failure surfaces for tests with viscous fluid (prototype scale)

Test Name	V_$\sqrt{N}$_10g	V_$\sqrt{N}$_30g	V_$\sqrt{N}$_50g	V_N_10g	V_N_30g	V_N_50g
Propagation rate (m/sec)	1.1	1.2	1.5	1.0	1.2	1.2

5.5.3. Excess pore pressures and excess pore pressure ratios

The development of EPP measured by PPT3 is shown in Figure 5.7. The moment of the sudden increases in the EPP indicates the onset of liquefaction in samples. EPP is measured close to zero before the onset of liquefaction and drops back to zero again after liquefaction. For the tests at the same g-level, samples with higher viscosity (N-fluid-tests) show larger generated EPP. The permeability of N-fluid is $\sqrt{N}$-times smaller than that of $\sqrt{N}$-fluid, hence ($\dot{\mathrm{DPP}}$) for an N-fluid test is $\sqrt{N}$-times less than that for a $\sqrt{N}$-fluid test at the same g-level. Thus, it can be expected that a lower ($\dot{\mathrm{DPP}}$) (closer to fully undrained conditions) would result in a higher EPP.

The excess pore pressure ratios as defined in Equation 5.26 (Biondi et al., 2000) are illustrated in Figure 5.8,

$$r_{\mathrm{u}} = \frac{\Delta u}{\gamma' H \cos\theta_{\mathrm{f}}} \tag{5.26}$$

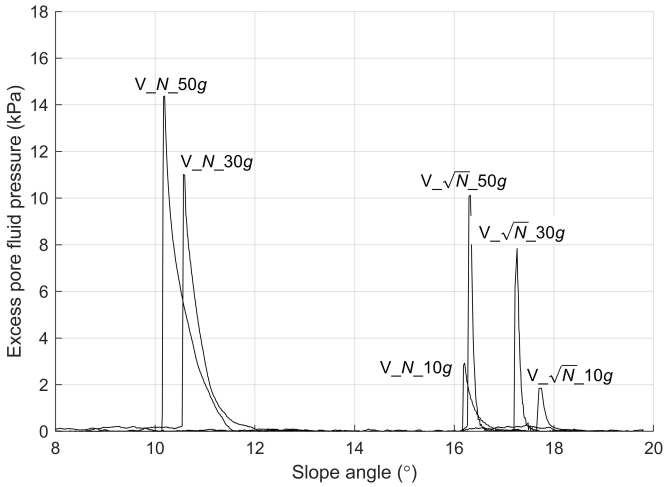

Figure 5.7: Excess pore fluid pressure development at position of PPT3 during increase of slope angle

where, Δu is the peak of measured EPP, H is the normal distance between the slope surface and the soil element.

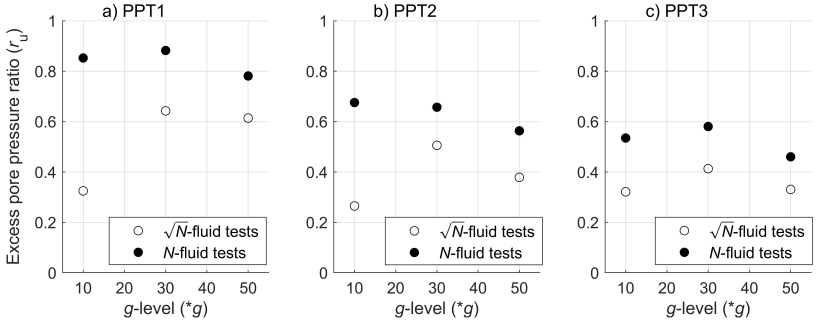

Figure 5.8: Excess pore pressure ratios at three PPT positions

During liquefaction, the sand mass flows towards slope toe. Hence, the EPP ratios were influenced by the dynamic behaviour of the flow slides as well as the rigid boundaries. EPP ratios are similar in N-fluid tests, but not in $\sqrt{N}$-fluid tests. This behaviour infers that N-fluid tests represent a similar prototype behaviour in terms of the generation of EPP during seabed liquefaction. Accordingly, it can be concluded that N-fluid should be used in centrifuge models for studying the post-liquefaction behaviour of saturated sand.

For the tests with $\sqrt{N}$-fluid, only the EPP ratios of PPT3 are close, which might be explained by the fact that the slope crest side was affected less by the energy of flow slides than the slope middle and slope toe. The EPP ratios are less than 1, though

liquefaction happened in all samples. It should be noted that EPP ratio can be less than unity when failure occurs with a non-zero deviatoric stress. Sadrekarimi (2019) proposed that the static liquefaction of a submerged slope could occur with $r_u < 1$ and the magnitude of r_u is related to soil shear modes, such as triaxial compression and triaxial extension. Moreover, the following four postulations might be also the reasons that EPP ratio < 1: i. due to the base boundary effect, the bottom sand layer did not fully liquefy during slope failure; ii. during flow slides, generation and dissipation of EPP coexist; iii. dilation might happen during failure since bottom sand layer might be in dense state; iv. due to the low data logging rate which is 2 HZ and the fact that EPP generates so quickly (Figure 5.7) that real peaks might have not been captured as explained in Chapter 4.

5.6. Conclusions

The scaling factors of the pore fluid viscosity for simulating the onset of static liquefaction and post-liquefaction behaviour, in the modelling of fully saturated sand layers in a centrifuge, have been investigated. A hypothesis of the triggering mechanism of a monotonic-load induced saturated sand liquefaction has been explained. The scaling law for the pore fluid viscosity has been derived based on the grain scale analysis. Static liquefaction has been observed at various g-levels. The onset and development of liquefaction, the excess pore pressures and the excess pore pressure ratios have been investigated. The main conclusions are presented below:

- Static liquefaction of a fully saturated loose sand layer could be triggered locally by fluid-grain interaction at the onset of the change of drainage regime from drained to (partially) undrained conditions.
- The derivation of scaling law for the triggering mechanism of static liquefaction should be based on the hydro-mechanical processes at the grain scale.
- The consistency of failure angles for $\sqrt{N}$-fluid tests conducted at various centrifugal accelerations proves that a $\sqrt{N}$-fluid should be applied for simulating the onset of static liquefaction of underwater slopes triggered by monotonic loads.
- Slope surface of an underwater sandy slope tends to liquefy first while the slope steepening happens.
- A pore fluid with a viscosity N-time that of water is required to simulate the flow slide dynamic behaviour (post-liquefaction behaviour) in a centrifuge.
- The onset of static liquefaction of saturated sandy slope (slope stability) and the slope post-liquefaction behaviour should be studied separately in centrifuge model tests.

List of Symbols

Symbol	Explanation
$10g$, $30g$ and $50g$	tested centrifuge accelerations
CT	computed tomography
$\dot{\mathrm{DPP}}$	dissipation rate of pore pressure
EPP	excess pore pressure
$\dot{\mathrm{GPP}}$	generation rate of pore pressure
HPMC	Hydroxypropyl Methylcellulose
$\sqrt{N}$-fluid	viscous fluid that is $\sqrt{N}$-time more viscous than water
N-fluid	viscous fluid that is N-time more viscous than water
Ng	centrifuge acceleration which is $10g$, $30g$ and $50g$
PPT	pore pressure transducer
TR	tilting rate
fps	frame per second
subscripts m and p	model scale and prototype scale, respectively
superscript *	scaling ratio of prototype to model
A_{grain}	contacting area between the grain and pore fluid
C_{x}	a constant
C_{Dr}	a constant factor related to sand properties including Dr_0, e_{min}, e_{max} and sand stiffness
C_{sand}	a factor of sand grain diameter and shape and tortuosity of channels
D_{10}, D_{30} and D_{60}	grain diameter at 10%, 30% and 60% passing
Dr and Dr_0	relative density and initial relative density at 0 kPa, respectively
$Dr_{1\mathrm{g}}$ and Dr_{Ng}	average relative densities of sample at $1g$ and Ng, respectively
F	force
$F^{\mathrm{impulse}}_{\mathrm{grain\text{-}fluid}}$	force in between the pore fluid and sand grain
G_{s}	specific gravity
H	normal distance between slope surface and the soil element
$H_{\mathrm{s,1g}}$	sample height after sample preparation, at normal gravity condition
H_{s}	sample height
$H_{\mathrm{s,Ng}}$	sample height at Ng condition
L	length
N	geometrical scaling factor which is 10, 30 and 50
Pa	atmospheric pressure
V	velocity
V_{f}	pore fluid velocity
V_{grain}	grain velocity vector under drained condition

Symbol	Definition
$V_{\text{grain,x}}$, $V_{\text{grain,y}}$ and $V_{\text{grain,z}}$	grain velocities in x, y and z directions under drained condition, respectively
$V_{\text{grain}}^{\text{undrained}}$	grain velocity vector under undrained condition
$V_{\text{grain,x}}^{\text{undrained}}$	grain velocity under undrained condition in x direction
a	acceleration
e_{min} and e_{max}	minimum and maximum void ratios
m	mass
m_{grain}	sand grain mass
n	porosity
q	specific discharge
r_{u}	excess pore pressure ratio
t	time
x, y and z	cartesian coordinates
Δh_{h}	hydraulic head difference
Δp	pressure difference
Δu	peak of measured EPP
σ_{v}'	vertical effective stress
γ'	sand buoyancy unit weight
γ_{f}	fluid unit weight
θ	slope angle
θ_{f}	slope angle at the onset of liquefaction
κ	intrinsic permeability
μ	dynamic viscosity
ρ_{f}	fluid density
ρ_{grain}	grain density

References

Arulanandan, K., Thompson, P., Kutter, B., Meegoda, N., Muraleetharan, K., and Yogachandran, C. (1988). Centrifuge modeling of transport processes for pollutants in soils. *Journal of Geotechnical Engineering*, 114(2):185–205.

Askarinejad, A., Beck, A., and Springman, S. M. (2015). Scaling law of static liquefaction mechanism in geocentrifuge and corresponding hydromechanical characterization of an unsaturated silty sand having a viscous pore fluid. *Canadian Geotechnical Journal*, 52(6):708–720.

Askarinejad, A., Zhang, W., de Boorder, M., and van der Zon, J. (2018). Centrifuge and numerical modelling of static liquefaction of fine sandy slopes. *Physical Modelling in Geotechnics*, 2:1119–1124.

Biondi, G., Cascone, E., Maugeri, M., and Motta, E. (2000). Seismic response of saturated cohesionless slopes. *Soil Dynamics and Earthquake Engineering*, 20(1-4):209–215.

Bowman, E. T., Laue, J., Imre, B., and Springman, S. M. (2010). Experimental modelling of debris flow behaviour using a geotechnical centrifuge. *Canadian geotechnical journal*, 47(7):742–762.

Byrne, P. M., Park, S.-S., Beaty, M., Sharp, M., Gonzalez, L., and Abdoun, T. (2004). Numerical modeling of liquefaction and comparison with centrifuge tests. *Canadian Geotechnical Journal*, 41(2):193–211.

Cargill, K. W. and Ko, H.-Y. (1983). Centrifugal modeling of transient water flow. *Journal of Geotechnical Engineering*, 109(4):536–555.

Carman, P. C. (1939). Permeability of saturated sands, soils and clays. *The Journal of Agricultural Science*, 29(2):262–273.

Chapuis, R. P. (2004). Permeability tests in rigid-wall permeameters: Determining the degree of saturation, its evolution, and its influence of test results. *Geotechnical Testing Journal*, 27(3):304–313.

Darcy, H. (1856). Les fontaines publiques de la ville de dijon, dalmont. *Victor Dalmont*.

De Jager, R. R. (2018). *Assessing Liquefaction Flow Slides: Beyond Empiricism*. Doctoral dissertation, Delft University of Technology.

Garnier, J., Gaudin, C., Springman, S. M., Culligan, P., Goodings, D., Konig, D., Kutter, B., Phillips, R., Randolph, M., and Thorel, L. (2007). Catalogue of scaling laws and similitude questions in geotechnical centrifuge modelling. *International Journal of Physical Modelling in Geotechnics*, 7(3):1–23.

Gonzalez, L., Abdoun, T., and Sharp, M. K. (2002). Modelling of seismically induced liquefaction under high confining stress. *International Journal of Physical Modelling in Geotechnics*, 2(3):01–15.

Goren, L., Aharonov, E., Sparks, D., and Toussaint, R. (2010). Pore pressure evolution in deforming granular material: A general formulation and the infinitely stiff approximation. *Journal of Geophysical Research: Solid Earth*, 115(B09216).

Hance, J. J. (2003). *Development of a database and assessment of seafloor slope stability based on published literature*. Doctoral dissertation, University of Texas at Austin.

Krapfenbauer, C. (2016). *Experimental investigation of static liquefaction in submarine slopes*. Master thesis, Delft University of Technology.

Lade, P. V. (1992). Static instability and liquefaction of loose fine sandy slopes. *Journal of Geotechnical Engineering*, 118(1):51–71.

Lade, P. V. and Yamamuro, J. A. (2011). Evaluation of static liquefaction potential of silty sand slopes. *Canadian Geotechnical Journal*, 48(2):247–264.

Locat, J. and Lee, H. J. (2002). Submarine landslides: advances and challenges. *Canadian Geotechnical Journal*, 39(1):193–212.

Maghsoudloo, A., Askarinejad, A., De Jager, R., Molenkamp, F., and Hicks, M. (2018). Experimental investigation of pore pressure and acceleration development in static liquefaction induced failures in submerged slopes. In *9th International Conference of Physical Modelling in Geotechnics, London*, volume 2, pages 987–992. CRC Press.

Ng, C. W. (2014). The state-of-the-art centrifuge modelling of geotechnical problems at hkust. *Journal of Zhejiang University SCIENCE A*, 15(1):1–21.

Phillips, R. and Byrne, P. (1995). Modeling flowslides caused by static loading. *Transportation Research Record*, pages 12–21.

Sadrekarimi, A. (2019). Prediction of static liquefaction landslides. In *Civil and Environmental Engineering Presentations 4 in GEO ST.JOHN's 2019*.

Schofield, A. N. (1980). Cambridge geotechnical centrifuge operations. *Geotechnique*, 30(3):227–268.

Singh, D. N. and Gupta, A. K. (2000). Modelling hydraulic conductivity in a small centrifuge. *Canadian Geotechnical Journal*, 37(5):1150–1155.

Sladen, J., D'hollander, R., and Krahn, J. (1985). The liquefaction of sands, a collapse surface approach. *Canadian Geotechnical Journal*, 22(4):564–578.

Steedman, R. S., Ledbetter, R. H., and Hynes, M. E. (2000). The influence of high confining stress on the cyclic behavior of saturated sand. In *Soil Dynamics and Liquefaction 2000*, pages 35–57.

Stewart, D. P., Chen, Y.-R., and Kutter, B. L. (1998). Experience with the use of methylcellulose as a viscous pore fluid in centrifuge models. *Geotechnical Testing Journal*, 21(4):365–369.

Stronge, W. J. (2018). *Impact mechanics*. Cambridge University Press, Cambridge.

Take, W., Bolton, M., Wong, P., and Yeung, F. (2004). Evaluation of landslide triggering mechanisms in model fill slopes. *Landslides*, 1(3):173–184.

Take, W. A. and Beddoe, R. A. (2014). Base liquefaction: a mechanism for shear-induced failure of loose granular slopes. *Canadian Geotechnical Journal*, 51(5):496–507.

Taylor, R. (1995). *Geotechnical centrifuge technology*. Blackie Academic & Professional, Chapman & Hall, London.

Taylor, R. (2014). *Geotechnical centrifuge technology*. Blackie Academic and Professional.

Verruijt, A. and Van Baars, S. (2007). *Soil mechanics*. VSSD, Delft.

Ye, Y., Lai, X., Pan, G., Li, Q., Zhuang, Z., Liu, D., Chen, X., Wei, Y., Chen, J., Hu, T., Chen, X., Zhan, W., Li, Q., Tian, S., Li, D., and He, X. (2017). *Marine Geo-hazards in China*. Elsevier, Amsterdam.

Zhang, J., Lin, H., and Wang, K. (2015). Centrifuge modeling and analysis of submarine landslides triggered by elevated pore pressure. *Ocean Engineering*, 109:419–429.

Zhang, M. (2006). *Centrifuge modelling of potentially liquefiable loose fill slopes with and without soil nails*. Doctoral dissertation, Hong Kong University of Science and Technology.

Zhang, W. and Askarinejad, A. (2019). Centrifuge modelling of submarine landslides due to static liquefaction. *Landslides*, 16(10):1921–1938.

Zhang, W. and Askarinejad, A. (2020). Centrifuge modelling of static liquefaction in submarine slopes: the scaling law dilemma. *Canadian Geotechnical Journal*.

6

Ultimate lateral pressures exerted on buried pipelines by the initiation of submarine landslides

不积跬步，无以至千里；
不积小流，无以成江海。

《荀子. 劝学篇》

Unless you pile up little steps, you can never journey a thousand miles;
Unless you pile up streams, you can never make a river or a sea.

XUNZI

The content of this chapter has been submitted as a research article to Landslides.

6.1. Abstract

Submarine slope instabilities are one of the major threats for offshore buried pipelines. This paper is intended to present a testing method to evaluate the ultimate pressure acting on a buried pipeline as a result of an inclined seabed liquefaction. Small-scaled model tests with pipes buried at three different embedment ratios have been conducted at 50g in a geotechnical centrifuge. A high speed, high resolution imaging system was developed to quantify the soil displacement field in the soil body and to visualize the development of the liquefied zone. The ultimate pressures were compared with the geotechnical approaches proposed by Audibert and Nyman (1977), Calvetti et al. (2004) and Zhang and Askarinejad (2019a) as well as the fluid dynamics approach suggested by Zakeri et al. (2008). The outcomes of this case study show that the currently available theoretical approaches either under or over-estimate the ultimate stresses acting on the buried pipelines most are not able to predict the trend of the imposed pressure on the pipe with the landslide velocity, i.e. shear strain rate. A new relationship between the shear strain rate and the ultimate pressure acting on the buried pipeline is suggested in this paper based on extensive experimental results.

Key words*: Underwater infrastructure, Submarine landslides, Liquefaction, Soil-pipeline interaction, Image analysis*

6.2. Introduction

Offshore pipelines are often buried in the seabed for protection against hydrodynamic forces caused by strong currents/waves or fishing gear (Fredsøe, 2016). Due to the long transportation distance and complexity of the seafloor environment, these pipelines may go through a variety of geological conditions, thus they are threatened by offshore geo-hazards. One of main reported geo-hazards is marine landslides (Parker et al., 2008, Sahdi et al., 2014, Zakeri et al., 2008). A complete study of the available data on offshore pipeline safety during the period from 1967 to 1990 was commissioned by the Marine Board of the National Research Council (Woodson, 1991), which reported that 12% of pipeline failures on the Gulf of Mexico (U.S. outer continental shelf region) were caused by seabed movement. Failure of offshore pipelines may cause significant environmental pollution due to the leakage of transported materials in addition to the economic loss and social impact (Randolph and Gourvenec, 2011).

If a segment of a buried pipeline is subjected to seabed movement, the pipeline will deform as shown schematically in Figure 6.1. The pipeline displacement and deformation are caused by the landslide-induced pressures (where q_u is the ultimate pressure in the x direction which is referred as the lateral direction hereafter). Meanwhile, the pipeline is restrained by the passive soil resistance, frictional resistance and pipeline fixities outside of the seabed failure zone (Randolph et al., 2010, Summers and Nyman, 1985). During a landslide, a pipeline can bear loads in the vertical, lateral and axial directions. Among them, the magnitude of the load in the lateral direction is normally regarded as the greatest (ASCE, 1984, Zakeri et al., 2008). Therefore, knowing the ultimate lateral pressure acting on a buried pipeline due to a marine landslide is crucial in offshore pipeline design.

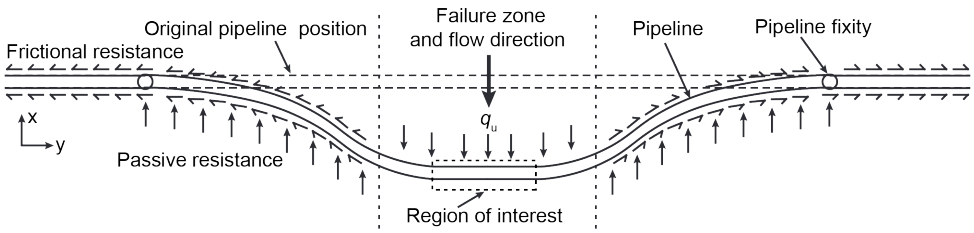

Figure 6.1: Schematic illustration of pipeline deformation due to seabed soil movement (top view)

The duration of submarine slope movements may range from less than one hour to several days. The induced forces acting along the pipeline depend on the landslide velocity, and thus the shear strain rate (Georgiadis, 1991, Zhu and Randolph, 2011). Regarding the velocity of soil movements, the soil-pipeline interaction mechanism of submarine buried pipelines has been commonly investigated from two perspectives, namely the geotechnical approach and the fluid dynamics approach. These two approaches consider two extreme offshore landslides in terms of slide velocity.

The geotechnical approach is suitable for the case when the relative soil velocity

compared to the pipeline is sufficiently low that the soil holds strength and the soil behaviour can be described within the conventional soil mechanics framework. Researchers have proposed formulas in the form of Equation 6.1 (for sand material) and Equation 6.2 (for clay material) for evaluating the ultimate horizontal pressure, q_{u}, acting on a buried pipeline caused by the relative soil-pipe displacement (e.g. Audibert and Nyman, 1977, Bea and Aurora, 1983, Calvetti et al., 2004, Georgiadis, 1991, Guo and Stolle, 2005, Summers and Nyman, 1985, Trautmann et al., 1985, Zhang and Askarinejad, 2019a),

$$\text{sand: } q_{\mathrm{u}} = \gamma'_{\mathrm{soil}} H_{\mathrm{c}} N_{\mathrm{q\text{-}sand}} \tag{6.1}$$

$$\text{clay: } q_{\mathrm{u}} = s_{\mathrm{u}} N_{\mathrm{q\text{-}clay}} \tag{6.2}$$

where, γ'_{soil} is the effective unit weight; H_{c} is the pipe buried depth, from the soil surface to the pipe centre; $N_{\mathrm{q\text{-}sand}}$ is the bearing capacity factor for the sand material, which has a relationship with the pipe embedment ratio (H_{c}/D, D is the pipe diameter) and the soil friction angle (Hansen, 1961, Ovesen, 1964); s_{u} is the undrained shear strength; and $N_{\mathrm{q\text{-}clay}}$ is the bearing capacity factor for the clay material.

It is well accepted that soil shear strength is influenced by shear strain rate (Boukpeti et al., 2012, Schapery and Dunlap, 1978). Georgiadis (1991) argued that the landslide induced pressure on a buried pipeline is affected by the soil sliding velocity and proposed a power law model (Equation 6.3) to describe the strain-rate dependency of soil undrained strength, where V_{shearing} is the shearing velocity, $s_{\mathrm{u,ref}}$ is the soil undrained strength tested at a reference shearing velocity, $V_{\mathrm{shearing,ref}}$, and η is an empirical viscosity coefficient. Boukpeti et al. (2012) investigated the shear strain rate ($\dot{\gamma}$) effect on s_{u} for clay material and adopted the power law model as well (Equation 6.3), where $\dot{\gamma}_{\mathrm{ref}}$ is the reference shear strain rate ($\dot{\gamma}_{\mathrm{ref}} = V_{\mathrm{shearing,ref}}/D$).

$$s_{\mathrm{u}} = s_{\mathrm{u,ref}} \left(\frac{V_{\mathrm{shearing}}}{V_{\mathrm{shearing,ref}}} \right)^{\eta} \text{ or } s_{\mathrm{u}} = s_{\mathrm{u,ref}} \left(\frac{\dot{\gamma}}{\dot{\gamma}_{\mathrm{ref}}} \right)^{\eta} \tag{6.3}$$

The fluid dynamics approach has been used to study submarine landslides when the sliding soil is regarded as a low strength debris flow or turbidity currents (Locat and Lee, 2002, Niedoroda et al., 2003, Sahdi et al., 2014, Zakeri, 2009). Randolph et al. (2011) reported that the pressure acting on a pipeline is related to the density (ρ_{slide}) and velocity (V_{slide}) of the sliding soil, as well as to the drag coefficient (C_{D}). Based on the fluid dynamics and rheology principles (Pazwash and Robertson, 1975), the ultimate lateral pressure can be estimated from Equation 6.4.

$$q_{\mathrm{u}} = \frac{1}{2} C_{\mathrm{D}} \rho_{\mathrm{slide}} V_{\mathrm{slide}}^2 \tag{6.4}$$

The two methods outlined above have been proposed and verified based on laboratory tests and have been frequently used in practice. However, the available methods provide a wide range of prediction on the landslides induced loads (Bea

and Aurora, 1983, Georgiadis, 1991, Zakeri, 2009). Accordingly, it is necessary to bear in mind that both approaches have their own strengths and limitations which originate from the corresponding experiments from which the two approaches were developed.

In the recent decades, for studying soil pipeline interaction, many physical models were designed with either a "pulled-pipe" method or a "released-gate" method. In the "pulled-pipe" method the buried pipe is artificially pulled by a mechanical system in a single direction (e.g. Almahakeri et al., 2013, Ansari et al., 2019, Audibert and Nyman, 1977, Calvetti et al., 2004, Liu et al., 2015, Oliveira et al., 2009, Ono et al., 2017, Paulin, 1998, Robert et al., 2016, Roy and Hawlader, 2012, Sahdi et al., 2014, Tian and Cassidy, 2011, Trautmann et al., 1985, Zhang et al., 2002). In the "released-gate" method, a soil flow is triggered by releasing a rotatable/releasable gate which is designed to keep the soil material in its original position (e.g. Acosta et al., 2017, Gue et al., 2010, Yin et al., 2017, Zakeri et al., 2012, 2008).

The testing condition of the "pulled-pipe" method represents the case when a pipe moves actively, as illustrated in Figure 6.2a (Case 1). In reality, the pipes may be pulled by fishing gear or anchors. The soil pressures acting on a buried pipe caused by the pipe movement (i.e. the pipe moves actively) is different than the case when the soil pressures are determined by the soil movement (i.e. the soil mass moves actively). It is because that the soil failure mechanisms around the pipe for these two cases are different as explained in Chapter 3. The "released-gate" method can be employed for the case that a debris flow passes around a pipeline that is either laid on the seabed or suspended above the seabed as demonstrated in Figure 6.2b (Case 2).

Figure 6.2c (Case 3) demonstrates the early stage of seabed slope liquefaction, which can be triggered by either dynamic loads (such as earthquakes, tsunamis, and waves) or static loads (such as rapid accumulation of sediments, seabed erosion and dredging) as discussed by Locat and Lee (2002), Hance (2003) and Ye et al. (2017). The soil/fluid flow behaviour in the post-liquefaction stage of seabed liquefaction triggered by various mechanisms are similar, as the soil-fluid flow is mainly driven by the gravitational forces (Iverson, 1997). It is important to note that the soil failure mechanism in Case 1 is different than that in Case 3, owing to the differences in a) seabed inclination (Case 1 has a flat surface, while Case 3 has a certain slope angle); b) excess pore pressure (EPP, which exists in Case 3 but not in Case 1); c) soil resistance mobilisation mechanism (soil moves passively in Case 1 and actively in Case 3). Moreover, comparing Case 2 to Case 3, the reduction in soil-fluid mixture strength in Case 2 is much more dramatic than in Case 3, owing to a higher moving velocity and a more sufficient mixture in the former. Therefore, it can be concluded that the soil failure mechanisms and soil (or soil-fluid mixture) properties in the three conditions illustrated in Figure 6.2 are all different. Considering the fact that the geotechnical approach is developed for Case 1 and the fluid dynamic approach is developed for Case 2, neither of them could be applied for Case 3.

Currently, the available literatures fall short in providing a means to investigate the ultimate pressure subjected to a pipeline buried in a liquefied slope (Figure 6.2c). Teh et al. (2006) investigated the pipeline stability on a liquefied seabed.

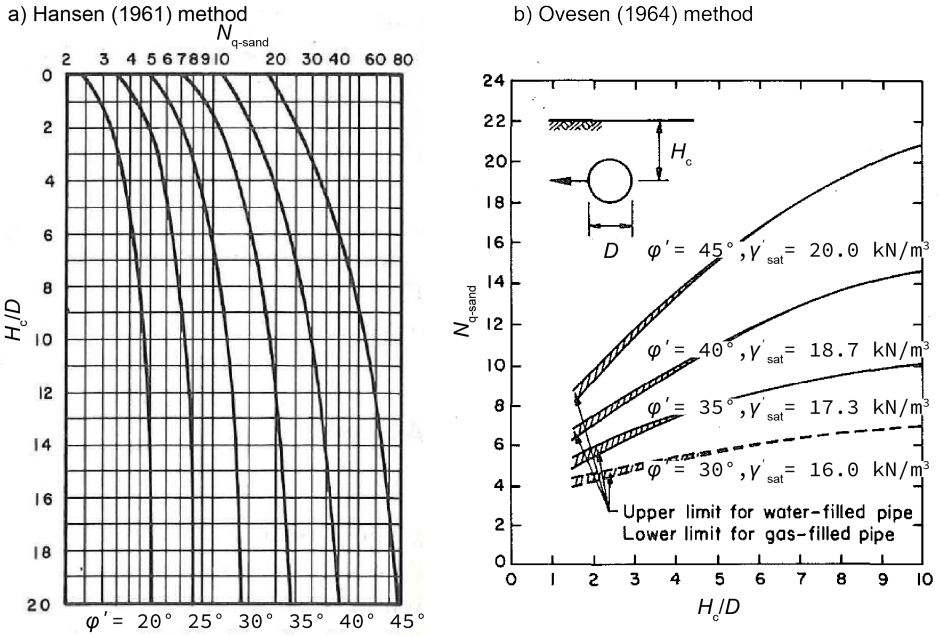

Figure 6.2: Illustration of soil-pipeline interaction at three cases: a) active pipe movement induced soil failure; b) debris flow (θ is slope angle); c) initiation of seabed slope liquefaction

However, only flat seabed condition was applied in their experiments with the main focus on floating/sinking behaviour of a pipeline during seabed liquefaction. Calvetti et al. (2004) built up a $1g$ model which is able to simulate buried pipeline movement (the pulled-pipe method) in a partially liquefied flat seabed by applying a certain hydraulic gradient, i. They proposed Equation 6.5 as a modification of the geotechnical approach, for partially liquefied sand, where γ_w is the water unit weight.

$$q_u = (\gamma'_{soil} - i\gamma_w) H_c N_{q\text{-sand}} \tag{6.5}$$

Chapter 3 shows the influence of slope geometry on q_u by conducting centrifuge tests with pipes buried at various locations in sandy slopes. Equation 6.7 was proposed which further consider the effect of pipe burial position to the slope crest (L_c) and the slope angle (θ), where φ' is the soil friction angle and $N_{q\text{-sand}}$ is from the Ovesen (1964) method.

$$q_u = \gamma'_{soil} D \left(\frac{H_c}{D}\right)^{\omega} \left(\frac{D}{L_c}\right)^{(1-\omega)} N_{q\text{-sand}} \tag{6.6}$$

$$\omega = 1 + \frac{\ln \alpha}{\ln (L_c/D) + \ln (H_c/D)}, \text{ where } \alpha = \frac{\tan(45° - \varphi'/2)}{\tan\theta + \tan(45° - \varphi'/2)} \tag{6.7}$$

Based on the analysis above, the application of the existing methods to Case 3 shown in Figure 6.2c needs to be verified based on model tests that are able to represent the corresponding situation. Thus, a series of centrifuge tests have been conducted in this study with the objective of investigating the ultimate lateral pressure of a buried pipeline during the initiation of a marine landslide. The effects of slope angle, pipeline structural stiffness, pipe embedment ratio and relative soil velocity on the resultant ultimate pressure on the pipe are discussed and analysed using experimental data from centrifuge tests carried out at $50g$, where g is Earth's gravity.

6.3. Testing Methods

The beam centrifuge at TU Delft was used in this study, which has a nominal radius of 1.22 m and is able to generate a maximum centrifugal acceleration of $300g$. All of the tests presented in this paper have been conducted at $50g$. The effective centrifuge radius is taken as the distance from the centre of the centrifuge to 1/3 of the sample height (H_{sample}), so that the maximum error in stress profile is less than 2% of the prototype stress (Schofield, 1980, Taylor, 2014).

6.3.1. Test set-up

Zhang and Askarinejad (2019b) described an experimental set-up designed for triggering liquefaction of a submarine slope by steepening the slope angle in centrifuge. The same device is applied in this study, as shown in Figure 6.3. The device is equipped with a tilting mechanism which increases the inclination of the prepared loose sand layer around the rotating axis in the x-z plane until the sample liquefies or up to a maximum angle of 20°, at $50g$. The slope angle increasing rate is about 0.1°/sec in model scale which is 0.002°/sec in prototype scale. A high-speed camera (DMK 33UP5000) is connected to the strongbox with a holder which enables the observation of soil liquefaction and landslide flow. Figure 6.3b) schematically illustrates an inclined sample and the locations of seven installed pore pressure transducers (PPTi, where, i is the PPT sequence number from 1 to 7, and the sensor series number is MPXH6400A) which are distributed along the middle line in the cross-section through the middle of the sample. The buried pipeline is modelled by a stainless-steel tube with sealed ends, which has an outer diameter (D) of 0.9 m in prototype scale (18 mm in model scale). The pipe embedment depth (H) could be easily adjusted with the system discussed in the following section. Three types of embedment ratios (H/D) were selected in this study, namely 0.83, 1.27 and 1.75.

6.3.2. Pipe external pressure measuring system

Figure 6.4 illustrates the pipe holding system, which has two functions of keeping the pipe in position and measuring the soil resistance during slope failure. The top horizontal beam is fixed to the upper extension of the strongbox. The pipe connection features three threaded rods. The upper threaded rod is fixed to the top beam and is attached with a pair of bending strain gauges (a half Wheatstone bridge) to measure the load acting on the pipe in the x direction (main soil moving direc-

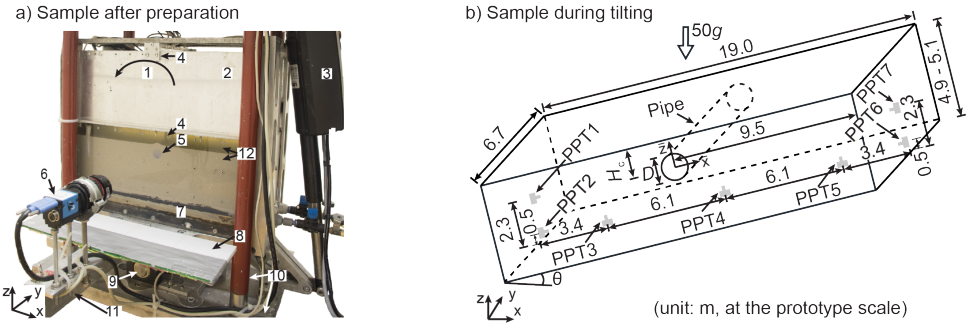

Figure 6.3: Illustration of test set-up in the centrifuge platform and the tilting mechanism. a) Sample after preparation: 1) rotation direction; 2) upper-box; 3) linear motor; 4) pipe connection; 5) pipe; 6) high speed, high resolution camera; 7) fluidization system; 8) lighting board; 9) rotating axis; 10) centrifuge platform; 11) camera holder; 12) viscous fluid and sand. b) Sample during tilting (prototype scale)

tion). The middle rod connecting the upper and lower threaded rods is designed with inner threads. This design permits testing with various pipe embedment ratios. Before each test, the strain-load-displacement relationship for the pipe connection was calibrated. Two types of rod diameter are selected to introduce two different pipe structural stiffness in the x direction. The pipeline is modelled using stainless steel tube with sealed ends, which has an outer diameter of 0.9 m and a length of 6.5 m at prototype scale.

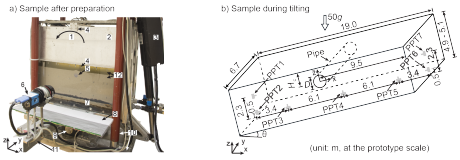

Figure 6.4: Schematic illustration of pipe connection system

This design permits testing with various pipe embedment ratios. Furthermore, two types of rod diameter are selected to introduce two different values of pipe fixity stiffness in the $\overline{x}$ direction in order to study the pipeline lateral structural stiffness effects on the soil-pipeline behaviour due to the soil passive resistance, the frictional resistance and the distance between two pipeline fixities, as demonstrated in Figure 6.1.

6.3.3. Soil and submerging fluid materials

Geba sand is used as the soil material due to its known properties in previous studies (such as: De Jager, 2018, Maghsoudloo et al., 2017). It is fine, sub-angular and sub-rounded sand with a mean particle size (D_{50}) of 0.117 mm, a uniformity coefficient (C_{u}) of an of 1.55, a coefficient of curvature (C_{c}) of 1.24. The particles specific gravity is 2.67, and the soil residual friction angle is 36°.

The viscous fluid made of Hydroxypropyl Methylcellulose (HPMC) powder is ap-

plied in this study as pore fluid. The fluid kinematic viscosity is chosen to be 50 cP, which is 50 times more viscous than the natural pore fluid - water. Each sample was prepared using the fluidization technique which was explained in Chapter 4.

6.4. Scaling laws

A marine landslide originates from an initially static sediment mass. Mobilization requires the development of sufficient excess pore pressure, which reduces the soil strength resulting in slope failure. According to the scaling law for time, a pore fluid with a viscosity of $\mu_{\mathrm{f}} = N\mu_{\mathrm{w}}$ is required (Taylor, 2014), for balancing the difference in the scaling factors of kinematic time and seepage time, where μ_{f} and μ_{w} are the fluid viscosity of the model fluid and the viscosity of the prototype fluid (water), respectively; N is the scaling factor for dimensions which is 50 in this study. The scaling factors of kinematic time ($t_{\mathrm{r}}^{\mathrm{k}}$) and seepage time ($t_{\mathrm{r}}^{\mathrm{s}}$) are shown in Equation 6.8, where the subscription 'r' denotes the scaling ratio of prototype to model.

$$t_{\mathrm{r}}^{\mathrm{k}} = N, \text{ and } t_{\mathrm{r}}^{\mathrm{s}} = N^2 \tag{6.8}$$

A liquefied subaqueous slope is driven by the gravitational forces, as the soil slides the gravitational potential energy transfers to internal kinetic energy (Iverson, 1997). Froude number (Fr, the ratio of the inertial forces to the gravitational forces) is reported as an important dimensionless factor to scale gravity-driven debris flow impacts on structures (Choi et al., 2015, Tobita and Iai, 2014). Fr is defined in Equation 6.9:

$$Fr = V_{\mathrm{slide}}/\sqrt{gH_{\mathrm{slide}}} \tag{6.9}$$

where, V_{slide} is the soil velocity, H_{slide} is the depth of a flow slide. Taylor (2014) argued that the scaling factor for velocity of a dynamic behaviour is 1, i.e. $V_{\mathrm{slide,r}} = V_{\mathrm{slide,p}}/V_{\mathrm{slide,m}}$, where the subscripts 'p' and 'm' stands for 'prototype' and 'model', respectively. Thus, the Froude number in the model is the same as it is in the prototype, as shown in Equation 6.10, since $H_{\mathrm{slide,p}}/H_{\mathrm{slide,m}} = N$.

$$Fr_{\mathrm{r}} = \frac{V_{\mathrm{slide,p}}}{V_{\mathrm{slide,m}}}\frac{\sqrt{NgH_{\mathrm{slide,m}}}}{\sqrt{gH_{\mathrm{slide,p}}}} = 1 \tag{6.10}$$

It can be inferred that at the beginning of slope liquefaction, the soil mass still has strength, although some certain excess pore pressure exists. With further development of slope failure, the soil mass transforms from soil-strength-dominated material to fluid-dynamic-dominated material. The dimensionless factor, Reynold number (Re), is commonly used to describe complex grain-fluid interactions, which is defined in Equation 6.11,

$$Re = \rho_{\mathrm{slide}} V_{\mathrm{slide}} D/\mu_{\mathrm{eff}} \tag{6.11}$$

where, ρ_{slide} is the soil-fluid mixture density; D is the characteristic length scale which is the pipe diameter as suggested by Zakeri et al. (2008); μ_{eff} is the effective

viscosity of the soil-fluid mixture. Though this study focuses on the initial stage of slope liquefaction, it is relevant to study the scaling law for Re, as the transition point from soil-strength-dominated material to fluid-dynamic-dominated material is uncertain.

The effective fluid viscosity (μ_{eff}) of a soil-fluid mixture is influenced by the presence of fine particles (Iverson, 1997). Thomas (1965) proposed Equation 6.12 to predict the effective fluid viscosity of a gravity-driven flow, in which buoyancy and drag forces dominate the grain-fluid interaction,

$$\mu_{\text{eff}} = \left(1 + 2.5C_{\text{fines}} + 10.05C_{\text{fines}}^2 + 0.00273e^{16.6C_{\text{fines}}}\right)\mu_{\text{f}} \tag{6.12}$$

where, C_{fines} is the volume fraction of fine grains in the soil-fluid mixture and μ_{f} is the submerging fluid viscosity. The soil material used in the model tests is assumed to be the same as that in the prototype, hence $C_{\text{fines,r}} = \rho_{\text{slide,r}} = 1$ and $\mu_{\text{eff,r}}$ equals to $\mu_{\text{f,r}}$ (Equation 6.13). In this study $\mu_{\text{f,r}} = 1/N$, thus the scaling factor for Reynold number is N^2 as shown in Equation 6.14.

$$\mu_{\text{eff,r}} = \mu_{\text{f,r}} \tag{6.13}$$

$$Re_{\text{r}} = \rho_{\text{slide,r}} V_{\text{slide,r}} D_{\text{r}} / \mu_{\text{eff,r}} = N^2 \text{ if } \mu_{\text{f,r}} = 1/N \tag{6.14}$$

Zhu and Randolph (2011) suggested that the shear strain rate ($\dot{\gamma}$) can be defined as Equation 6.15,

$$\dot{\gamma} = V_{\text{slide}}^{\text{relative}} / D \tag{6.15}$$

where, $V_{\text{slide,r}}^{\text{relative}}$ is the relative soil movement rate (the difference between the soil velocity and the pipe moving rate). The scaling factor for the relative soil movement rate is 1 as that for V_{slide}, hence the scaling factor for the shear strain rate ($\dot{\gamma}_{\text{r}}$) is $1/N$, see Equation 6.16.

$$\dot{\gamma}_{\text{r}} = V_{\text{slide,r}}^{\text{relative}} / D_{\text{r}} = 1/N \tag{6.16}$$

6.5. Results and Discussion

In total 23 centrifuge tests have been performed (Table 6.1). These tests are characterised into four groups. Three of them are distinguished by the ranges of pipe embedment ratio (H_{c}/D) which are 0.83, 1.27 and 1.75. These tests are designed for studying the burial depth effect on the ultimate pipe external pressure and are labelled with E1, E2 or E3 in the test ID. For each group of embedment ratios, the pipe was fixed with two types of flexibilities (labelled with K1 or K2 in the test ID) aiming to explore the effects of pipeline structural stiffness. The last group of tests are performed only with sand (S01 to S04), i.e. without a buried pipe. The mean height and mean relative density of all samples are around 5.0 m at prototype scale (with a standard deviation of 0.05m) and 63% at $50g$ (with a standard deviation of 2.4%), respectively. In the following sections, all test parameters and results are presented in prototype scale unless stated otherwise.

Table 6.1: Summary of all the centrifuge tests

Test ID	H_c/D (-)	θ (°)	K^a (kPa/(m/m))	Test ID	H_c/D (-)	θ (°)	K^a (kPa/(m/m))
E1K1_1	0.84	14.07	63.0	E2K2_2	1.20	15.05	77.4
E1K1_2	0.87	13.20	63.0	E2K2_3	1.27	15.03	77.4
E1K1_3	0.86	14.57	63.0	E2K2_4	1.27	12.93	77.4
E2K1_1	1.32	13.75	52.2	E3K2_1	1.72	14.03	63.0
E2K1_2	1.34	14.78	52.2	E3K2_2	1.71	12.75	63.0
E2K1_3	1.35	12.81	52.2	E3K2_3	1.78	14.37	63.0
E2K1_4	1.24	14.62	52.2	E3K2_4	1.77	14.47	63.0
E3K1_1	1.76	14.03	43.2	S01	-	15.75	-
E3K1_2	1.75	12.72	43.2	S02	-	15.12	-
E1K2_1	0.79	14.29	97.2	S03	-	16.50	-
E1K2_2	0.79	13.25	97.2	S04	-	16.52	-
E2K2_1	1.17	14.53	77.4				

[a]: K is normalized pipeline structural stiffness in lateral direction which is defined as the ratio of the soil pressure on the pipeline to the normalized pipeline displacement. The normalized pipeline displacement is the pipe displacement divided by the pipe diameter, hence K has a unit of kPa/(m/m).

6.5.1. Slope angles at failure

The slope angles at failure indicate the onset of liquefaction of the samples. The failure angles of all tests with various pipe embedment ratios are illustrated in Figure 6.5. Results show that the average failure angles of the tests with the buried pipe is about 14.0° which is about 2.0° less than that of tests without any pipe. It can be inferred that the existence of the pipe slightly reduced the slope stability due to the non-uniformity in the soil fabric around the pipe. Moreover, it can be observed that the pipe embedment ratios have a negligible effect on the failure angles.

6.5.2. Development of EPP and EPP ratios

Liquefaction of a soil material is essentially linked to the rise in EPP and the corresponding reduction in the soil effective stress and the soil strength (Eckersley, 1990, Take et al., 2015). It this study, the change of pore pressure at 7 locations (see Figure 6.3b) were recorded. EPP ratio (r_u) in Equation 6.17 defined by Biondi et al. (2000) is normally utilized to indicate the onset of liquefaction. Here, Δu is the measured value of EPP, H_{PPT} is the normal distance between the original slope surface and each PPT.

$$r_u = \frac{\Delta u}{\gamma'_{soil} H_{PPT} \cos\theta} \tag{6.17}$$

Figure 6.6 shows the development of r_u at 6 positions from test E2K2_1. Note that PPT7 was only effective in tests from E1K1_1 to E1K1_3. The measurement was stored with a frequency of 1 KHZ. PPT1 detects the change of r_u firstly, then

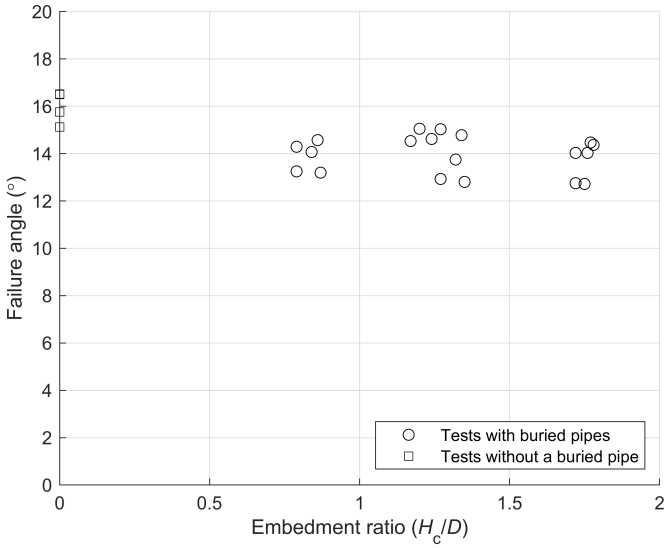

Figure 6.5: Failure angles of all centrifuge tests at various embedment ratios

PPT2. The value of r_u at both PPT1 and PPT2 locations shows a linear increase in about 2 seconds before showing a sudden rise. A possible explanation is that: i. due to the increase of shear stress EPP accumulates; ii. then with further accumulation of EPP, a reduction in the soil strength occurs, which results in a local liquefaction in the vicinity of the PPT1 and PPT2 in about 2 seconds.

The peak values r_u at all 7 locations of all tests are summarized in Figure 6.7. At each measuring position, r_u with various embedment ratios is in good agreement with that of the tests without a buried pipe indicating that the existence of the pipe did not influence the development of pore pressure and the testing system has a good repeatability.

Figure 6.7 indicates a drop in r_u from slope toe to slope crest (i.e. from PPT3 to PPT7). The r_u at the location of PPT1 is the highest amount all PPT positions and is larger than 1 which can be due to the kinetic energy of the flow slide. By evaluating 893 undrained shear tests, including triaxial compression tests, triaxial extension tests and simple shear tests, on cohesionless soils, Sadrekarimi (2019) concluded that static liquefaction could happen with r_u smaller than 1. The value of r_u for triggering a static liquefaction is essentially associated with models of shear as well as the principal stress ratio, $K_c = \sigma'_1/\sigma'_3$, where σ'_1 and σ'_3 are the major and minor principal stresses, respectively. For an infinite slope, K_c equals to $(1-\sin\theta)/(1+\sin\theta)$ which is 0.61 when the slope failure angle θ is 14°. Sadrekarimi (2019) further proposed relationships between the three shear models (triaxial compression, triaxial extension and torsional simple shear) and K_c. He proposed that r_u in the range of 0.136 - 0.35 is able to trigger slope static liquefaction when $K_c = 0.61$. However, all obtained r_u from experiments in this study is beyond this range.

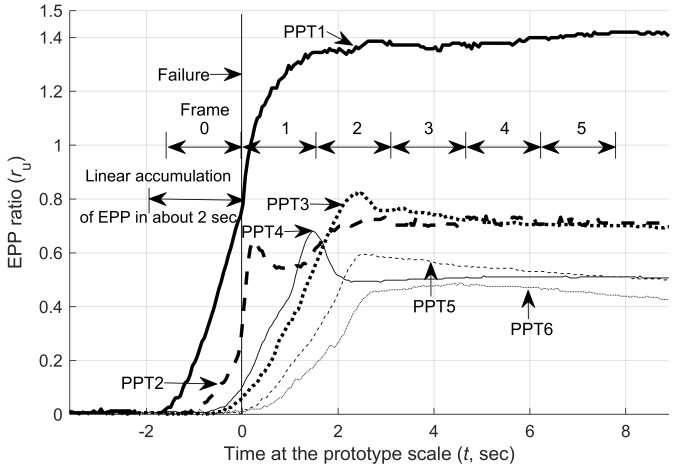

Figure 6.6: Development of EPP ratios of test E2K2_1 (note: the onset of slope failure is defined as t = 0 sec, and the slope angle of this test is 14.53 °)

Sadrekarimi (2019) suggested to employ r_u or EPP as an indicator in the landslide warning system for saturated cohesionless soils suffering monotonic loads. However, it seems to be difficult to apply this in the case of seabed liquefaction considering the quick accumulation of EPP as indicated in Figure 6.6. It is found that r_u rose abruptly only in a course of about 2 seconds before the slope failure took place.

6.5.3. Development of liquefied soil layers and soil displacement

Images were taken from one transparent side of the strongbox at an average rate of 36 frames per second before and during slope failure. The frames showing the soil movements were analysed using the PIV technique, as described by White et al. (2003) and Stanier et al. (2015). Nine frames were analysed for each test; Frame 0 and Frame 1 are the last frame right before the initiation of slope failure and the first frame after, respectively (see Figure 6.6).

Figure 6.8 illustrates the liquefied soil displacement field of a test without the pipe (S04) and a test with the pipe buried with an embedment ratio of 1.78 (E3K2_3). Once the liquefaction was initiated, sand particles moved swiftly in the direction mainly parallel to the slope surface. Results show that the top layer of the slope near the toe liquefied first in both tests, then the liquefaction zone propagated towards to the slope crest and the slope base. This observation indicates the limitation in applying the conventional limit equilibrium approach in catastrophic failure of submerged slopes which assumes that the slip surface appears instantaneously

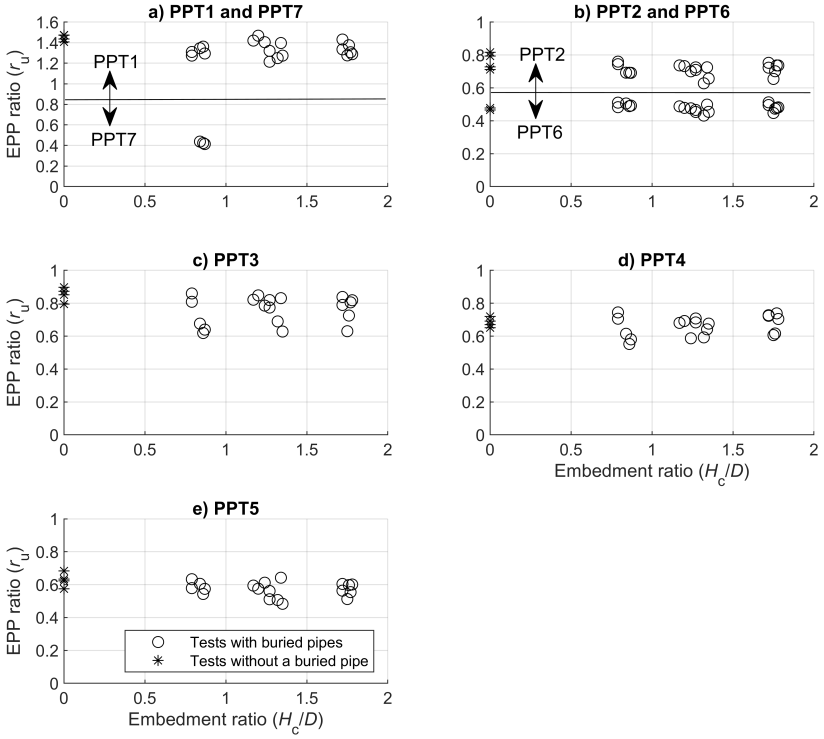

Figure 6.7: Maximum EPP ratios at all PPT positions of all tests

(Puzrin et al., 2004, Tiande et al., 1999). It is observed that the presence of the buried pipe has an influence on the soil movement regime. Figure 6.8d indicates that the lower boundary of the liquefaction zone initiated under the pipe and this phenomenon has been observed in other tests with the pipe as well.

Figure 6.9 illustrates the displacement of the soil around the pipe obtained from PIV analysis as well as the pipe displacement measurements for tests with H_c/D around 0.83 and 1.75. The soil and pipe displacement curves for each test have a similar trend–a linear increase in displacement for approximately 4 seconds after the initiation of liquefaction. However, the decrease in the rate of soil movement at around 4 seconds after the initiation of slope failure could be due to the mechanical boundary effects imposed by the strongbox, which hinders further flow of the soil. Therefore, the results of soil and pipe behaviour in the first 4 seconds are analysed and presented in the following subsections.

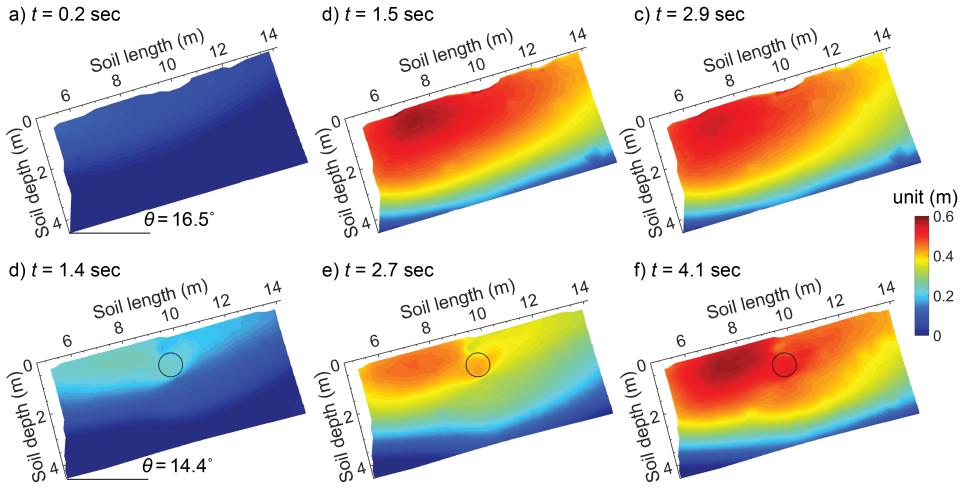

Figure 6.8: Soil displacement field of test S04 (subfigures a), b) and c)) and test E3K2_3 (subfigures d), e) and f)): a) t = 0.2 sec, b) t = 1.5 sec, c) t = 2.9, d) t = 1.4 sec, e) t = 2.7 sec and f) t = 4.1 sec (note: t denotes time and the onset of slope failure is defined as t = 0 sec)

6.5.4. Soil velocity distribution

Understanding the soil velocity profile is important to evaluate the constitutive equations for describing soil flows (Han et al., 2014). Johnson et al. (2012) assumed that, for a debris flow, the slide velocity should be the greatest at the flow surface and drops through the soil/flow depth. Many researchers (such as: Han et al., 2015, 2014, Hotta and Ohta, 2000, Iverson, 2012) adopted Equation 6.18 to match the slide velocity (V_{slide}) profile for a laminar debris flow moving over a rigid bed, where $\overline{V_{\text{slide}}}$ is the mean slide velocity, y is the soil depth from flow surface and H_{slide} is the total flow depth. The parameter β controls the shape of the velocity profile, which is plug-flow when $\beta = 1$ and simple shear when $\beta = 0$.

$$V_{\text{slide}} = (2-\beta)\overline{V_{\text{slide}}}\left(1-\left(1-\frac{y}{H_{\text{slide}}}\right)^{\frac{1}{(1-\beta)}}\right) \tag{6.18}$$

Hotta and Ohta (2000) conducted a series of rolling mill tests with both glass bead mixtures and plastic bead mixtures which are assumed to be similar to natural debris flows. A value of 1/3 for β was used by Hotta and Ohta (2000) for fitting the velocity profiles in the rolling mill. The same value for β was suggested by Han et al. (2014) for describing the vertical debris-flow velocity distribution of Jiasikou debris flow in the high-seismic-intensity zone of the Wenchuan earthquake. The velocity profile with β=0.5 matches the observations well from the large-scale debris flow tests performed by Johnson et al. (2012).

The soil velocity distribution of the tests S03 and S04 are presented in Figure 6.10. It is found that Equation 6.19, with β=0.72 and an amplification factor of 1.06, agrees satisfactorily with the results as shown in Figure 6.10. The profiles of soil velocity for the tests with buried pipes are shown in Figure 6.10 as well. By

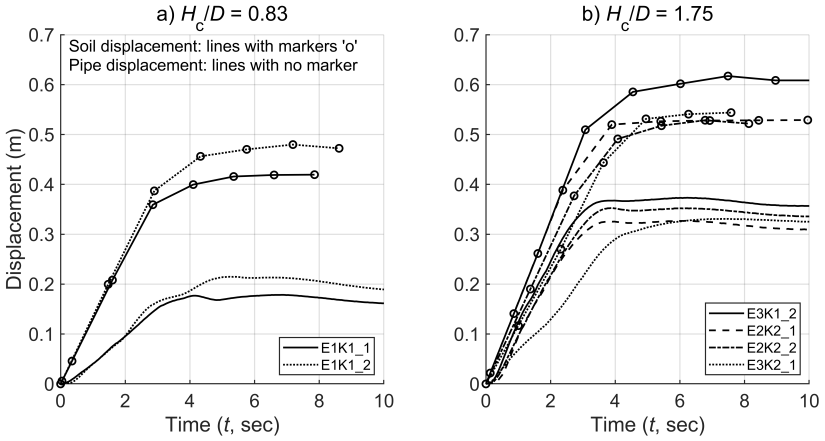

Figure 6.9: Examples of pipe displacement and soil displacement around the pipe (note: the onset of slope failure is defined as t = 0 sec)

comparing them with results of S03 and S04, it can be seen that the pipe reduced the soil velocity above the pipe and exaggerated that below the pipe.

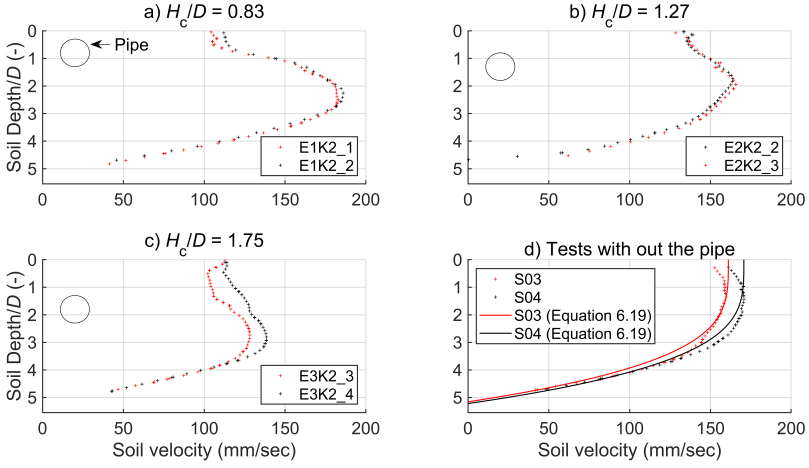

Figure 6.10: Soil velocity distribution along soil depth

$$V_{\text{slide}} = 1.06(2-\beta)\overline{V_{\text{slide}}}\left(1-\left(1-\frac{y}{H_{\text{slide}}}\right)^{\frac{1}{(1-\beta)}}\right) \text{ with } \beta = 0.72 \qquad (6.19)$$

6.5.5. Ultimate lateral pressure

The tests results indicate that the slope angle, pipeline structural stiffness, pipe embedment ratio and relative soil velocity influence the soil-pipeline interaction mechanism. The effects of these factors on the ultimate pressures exerted on pipelines are discussed below.

Slope angle and pipeline structural stiffness effects

The ultimate pressures (q_u) exerted on the pipes of all tests are summarized in Figure 6.11. Results of the tests with H_c/D around 1.27 and 1.75 show that q_u tends to slightly rise with the increasing of the slope angle at failure. This observation can be explained by the fact that a higher slope angle would result in a larger flow energy, hence it causes a higher pressure on the structure.

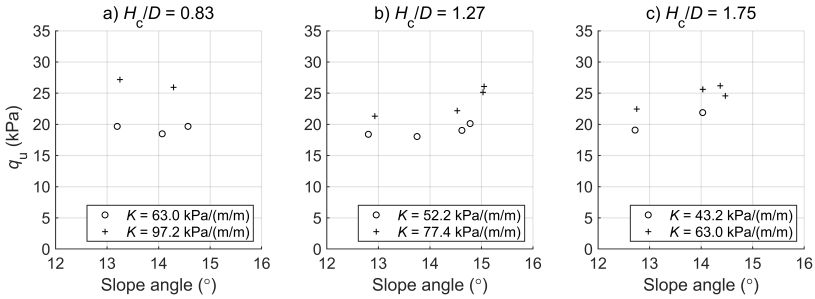

Figure 6.11: Ultimate lateral pressure on the pipe with various embedment ratios

In all cases, a smaller normalized pipeline structural stiffness (K) results in a smaller value of q_u. The normalized pipeline structural stiffness represents the stiffness of the pipeline fixity system in the direction parallel to the main soil flow direction (Figure 6.1). Under the same external lateral load, a flexible pipeline system (with a smaller value of K) could move further than a stiffer pipeline system (with a larger value of K). It can be inferred that reducing the pipeline structural stiffness could increase the pipeline displacement and hence could lessen the relative soil velocity. The effect of relative soil velocity on the development of q_u is discussed in the following section.

Comparison with existing methods and pipe embedment ratio effect

Figure 6.12 illustrates the ultimate lateral pressures applied to the buried pipes by the sliding soil with respect to the soil shear strain rate (Equation 6.15). Additionally, the estimations of q_u from both the geotechnical methods (Equations 6.1 and 6.6) and fluid dynamics method (Equation 6.4) are presented in this figure for comparison.

Estimations based on geotechnical approaches are dependent on pipe embedment depth but independent of the shear strain rate, as illustrated in Figure 6.12. The geotechnical methods (Equations 6.1 and 6.6) tend to overestimate the ultimate lateral pressure when H_c/D > 0.83. Here γ'_{soil}, D, L_c and θ are 9.2 kN/m^3, 0.9 m, 9.5 m and 14°, respectively.

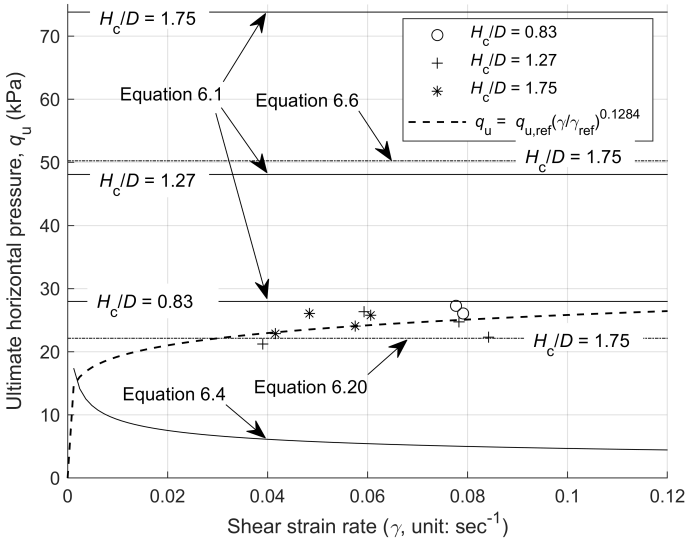

Figure 6.12: Effect of shear strain rate on ultimate lateral pressure pipe buried in sandy seabed (centrifuge tests)

6

Calvetti et al. (2004) followed the geotechnical approach and proposed Equation 6.5 for considering the hydraulic gradient effect (thus EPP effect) on soil strength. The excess pore pressure could reduce soil normal stress condition ($\gamma_{\text{soil}}H_{\text{c}}$) with a factor of ($1-r_{\text{u}}$). In line with Equation 6.5, Equation 6.20 is suggested to take the influence of EPP ratio on soil strength into account.

$$q_{\text{u}} = (1-r_{\text{u}})\gamma'_{\text{soil}}H_{\text{c}}N_{\text{q-sand}} \tag{6.20}$$

The results given by Equation 6.20 are shown in Figure 6.12, with H_{c}/D = 1.75, $N_{\text{q-sand}} = 3.9$ and $r_{\text{u}} = 0.7$. r_{u} is selected to be the average measured excess pore pressure ratios at PPT4 which is the closest sensor to the pipe (see Figures 6.3 and 6.7). Equation 6.20 slightly underestimates the ultimate pressure.

The predictions based on the fluid dynamics method (Equation 6.4) are highly dependent on the shear strain rate as illustrated in Figure 6.12. It can be seen that the fluid dynamics method tends to underestimate the horizontal ultimate pressure when the shear stain rate is less than 0.12 sec^{-1}.

The observations above infer that both the geotechnical and fluid dynamic methods are not applicable to the engineering situation that the offshore pipeline is buried in an unstable marine slope (Figure 6.2c). Considering the fact that both methods were developed and proved based on laboratory tests, each developed method has its own applicable conditions as well as limitations. Following are two explanations which can be the reasons that why neither the geotechnical method nor the fluid dynamics method fit the centrifuge test results.

Firstly, the failure mechanisms of these three cases (Figure 6.2) are different. The geotechnical method was examined by experiments using the artificially 'pulled-pipe' method. This testing situation is believed to be related to the engineering situation when the pipeline is pulled by a trawling gear or ship anchors, or to be related to the problem of pipeline buckling due to the change in thermal condition of the transporting material or internal pressure (Parker et al., 2008, White et al., 2007). However, in this study, the induced pressure is caused by the active movement of soil around the pipe. Furthermore, the fluid dynamics method is mainly derived from the tests with a pipe which is either laid on the seabed or hanging above the seabed and debris passes through as a result of slope failure which has happened at a place with a certain distance to the pipe location.

Secondly, the soil properties for these three cases are different too. The soil behaviour can be described by traditional soil mechanics for the case when a pipe is forced to move in a soil body; whereas the soil-fluid mixture behaves like Bingham-fluid (Sahdi et al., 2014) for the case when a pipe is hit by a debris flow. However, for the case when the soil near the pipe starts moving/flowing as a result of liquefaction, the soil can be partially liquefied, as the EPP ratio is generally less than 1 when a slope liquefies (Sadrekarimi, 2019). Though the liquefied soil moves fast even at the early stage of seabed liquefaction, the soil particles and fluid are not as well mixed as in a debris flow. Additionally, the soil strength may be severely reduced owing to the reduction in the effective stress caused by the EPP (Teh et al., 2006).

Shear strain rate effects

Georgiadis (1991) performed a series of pipe pulling tests in clay samples with various pulling rates and proposed a power-law function, Equation 6.3, to describe the effect of pipe moving rate on the drag force. In order to describe the effect of the shear strain rate on the ultimate pipe horizontal pressure, the power-law approach is utilized in this study, which is expressed in Equation 6.21, where $q_{\mathrm{u,ref}}$ is the ultimate lateral pressure when the soil shear strain rate is $\dot{\gamma}_{\mathrm{ref}}$.

$$q_{\mathrm{u}} = q_{\mathrm{u,ref}} \left(\frac{\dot{\gamma}}{\dot{\gamma}_{\mathrm{ref}}} \right)^{\eta} \tag{6.21}$$

The power-law function fits the results well with a viscosity coefficient, η, of 0.1284. Though Georgiadis (1991) performed the tests in clay material, he got a similar value for η which is 0.125. Zakeri et al. (2008) determined the shear strain rate and shear stress relationship by conducting rheometer tests on slurries which were mixed with clay and water. The percentage of clay mass varied from 10% to 35%, and the percentage of sand varied from 55% to 30% correspondingly. The sand used in their study has a D_{50} of 0.134 mm, a C_{c} of 8.8 and a C_{u} of 1.9. They applied a similar power law function to fit the shear stress-shear strain rate curves and got the value of η ranging between 0.11 and 0.14. Jeong et al. (2009) suggested that for most natural soils η is less than 0.2.

6.6. Conclusions

The ultimate pressure acting on a model pipe due to liquefaction of a sloping seabed was investigated by means of centrifuge model tests, exploring the influences of pipe embedment ratio, pipeline structural stiffness and shear strain rate. The liquefaction of a submerged slope was triggered by increasing shear stress monotonically. Under the assumption that the soil behaviour after the onset of seabed slope liquefaction caused by static loads is similar to that caused by dynamic loads, the following conclusions could be extrapolated to the dynamic-load-induced- (e.g. wave loads, tsunami and earthquake) and other static-load-induced- (e.g. dredging, fast sedimentation) seabed liquefaction. The observations from the tests reveal the following conclusions:

- The onset of liquefaction tends to take place in the slope surface layer close to slope toe and then it propagates towards the crest and deeper locations in the slope.
- It was found that the ultimate pressure applied to the pipe in a liquefied zone is essentially related to the shear strain rate according to the power-law relationship as defined in Equation 6.21 with a power coefficient, η = 0.1284. The magnitude of the shear strain rate is dependent on the slope angle as well as on the pipeline structural stiffness. A higher slope angle would result in a higher shear strain rate. A stiffer pipeline fixity system would reduce pipe displacement; hence it increases the shear strain rate which results in a larger external pressure to the pipe due to the landslide.
- The soil movement profile of a liquefied seabed without a buried structure at early stages of the onset of liquefaction is similar to that in a laminar debris flow. The soil velocity distribution along soil depth can be described by Equation 6.18.
- For a liquefied submerged slope, the maximum value of excess pore pressure ratio (r_u) is generally smaller than 1. It is found to be strongly dependent on the measurement locations due to the difference in shearing modes at various points in the slope. A value of r_u = 0.4 was observed at a location near the slope crest at the onset of liquefaction. Furthermore, the development of excess pore pressure can happen in the course of less than 2 seconds which implies that it is difficult to use excess pore pressure ratios as an indicator for the early warning systems specifically in submerged loose sandy slopes.

List of Symbols

Symbol	Definition
EPP	Excess pore pressure
HPMC	Hydroxypropyl Methylcellulose
PIV	Particle Image Velocimetry
PPT	Pore pressure transducer
Subscripts: 'm', 'p' and 'r'	model, prototype and ratio of prototype to model, respectively
g	gravity
i	hydraulic gradient
q_{u}	the ultimate landslide-induced lateral pressure
q_{ref}	the ultimate lateral pressure measured at $\dot{\gamma}_{\mathrm{ref}}$
r_{u}	EPP ratio
s_{u}	undrained shear strength
$s_{\mathrm{u,ref}}$	undrained strength tested at a reference shearing velocity
t	time
t^{k}	kinematic time
t^{s}	seepage time
y	soil depth from flow surface
C_{c}	coefficient of curvature
C_{D}	drag coefficient
C_{fines}	volume fraction of fine grains
C_{u}	uniformity coefficient
D	pipe diameter
D_{50}	mean particle size
Fr	Froude number
H_{c}	pipe buried depth
H_{c}/D	pipe embedment ratio
H_{PPT}	normal distance between the original slope surface and PPT
H_{sample}	sample height
H_{slide}	total flow depth
K	normalized pipeline structural stiffness in lateral direction
K_{c}	principal stress ratio
L_{c}	pipe burial position to slope crest
L_{slide}	approach flow depth
N	scaling factor for dimensions
$N_{\mathrm{q\text{-}clay}}$	bearing capacity factor for clay
$N_{\mathrm{q\text{-}sand}}$	bearing capacity factor for sand
Re	Reynold number
V_{shearing}	shearing velocity
$V_{\mathrm{shearing,ref}}$	reference shearing velocity
V_{slide}	soil velocity

Symbol	Definition
$\underline{V_{\text{slide}}^{\text{relative}}}$	relative soil velocity
V_{slide}	mean soil velocity
β	shape factor of the velocity profile
γ'_{soil}	soil effective unit weight
γ_{w}	water unit weight
$\dot{\gamma}$	shear strain rate
$\dot{\gamma}_{\text{ref}}$	reference shear strain rate
η	viscosity coefficient
Δu	excess pore pressure
θ	slope angle
μ_{eff}	effective viscosity of soil-fluid mixture
μ_{f}	viscosity of model fluid
μ_{w}	viscosity of porotype fluid (water)
ρ_{slide}	landslide density
σ'_1	major principal stress
σ'_3	minor principal stress
φ'	soil friction angle

References

Acosta, E. A., Tibana, S., de Almeida, M. d. S. S., and Saboya Jr, F. (2017). Centrifuge modeling of hydroplaning in submarine slopes. *Ocean Engineering*, 129:451–458.

Almahakeri, M., Fam, A., and Moore, I. D. (2013). Experimental investigation of longitudinal bending of buried steel pipes pulled through dense sand. *Journal of Pipeline Systems Engineering and Practice*, 5(2):04013014.

Ansari, Y., Kouretzis, G., and Sloan, S. W. (2019). Physical modelling of lateral sand-pipe interaction. *Géotechnique*, pages 1–16.

ASCE (1984). Guidelines for the seismic design of oil and gas pipeline systems. Report.

Audibert, J. M. and Nyman, K. J. (1977). Soil restraint against horizontal motion of pipes. *Journal of the Geotechnical Engineering Division*, 103(10):1119–1142.

Bea, R. G. and Aurora, R. P. (1983). Design of pipelines in mudslide areas. *Journal of petroleum technology*, 35(11):1,985–1,995.

Biondi, G., Cascone, E., Maugeri, M., and Motta, E. (2000). Seismic response of saturated cohesionless slopes. *Soil Dynamics and Earthquake Engineering*, 20(1-4):209–215.

Boukpeti, N., White, D., Randolph, M., and Low, H. (2012). Strength of fine-grained soils at the solid–fluid transition. *Géotechnique*, 62(3):213–226.

Calvetti, F., Di Prisco, C., and Nova, R. (2004). Experimental and numerical analysis of soil–pipe interaction. *Journal of geotechnical and geoenvironmental engineering*, 130(12):1292–1299.

Choi, C., Ng, C., Au-Yeung, S., and Goodwin, G. (2015). Froude characteristics of both dense granular and water flows in flume modelling. *Landslides*, 12(6):1197–1206.

De Jager, R. R. (2018). *Assessing Liquefaction Flow Slides: Beyond Empiricism*. Doctoral dissertation, Delft University of Technology.

Eckersley, D. (1990). Instrumented laboratory flowslides. *Geotechnique*, 40(3):489–502.

Fredsøe, J. (2016). Pipeline–seabed interaction. *Journal of Waterway, Port, Coastal, and Ocean Engineering*.

Georgiadis, M. (1991). Landslide drag forces on pipelines. *Soils and foundations*, 31(1):156–161.

Gue, C., Soga, K., Bolton, M., and Thusyanthan, N. (2010). Centrifuge modelling of submarine landslide flows. In Springman, S. M., Laue, J., and Linda, S., editors, *Physical Modelling in Geotechnics (ICPMG 2010)*, volume 2, pages 1113–1118, Zurich, Switzerland. CRC Press.

Guo, P. and Stolle, D. (2005). Lateral pipe–soil interaction in sand with reference to scale effect. *Journal of geotechnical and geoenvironmental engineering*, 131(3):338–349.

Han, Z., Chen, G., Li, Y., Wang, W., and Zhang, H. (2015). Exploring the velocity distribution of debris flows: an iteration algorithm based approach for complex cross-sections. *Geomorphology*, 241:72–82.

Han, Z., Chen, G., Li, Y., Xu, L., Zheng, L., and Zhang, Y. (2014). A new approach for analyzing the velocity distribution of debris flows at typical cross-sections. *Natural hazards*, 74(3):2053–2070.

Hance, J. J. (2003). *Development of a database and assessment of seafloor slope stability based on published literature*. Doctoral dissertation, University of Texas at Austin.

Hansen, J. B. (1961). The ultimate resistance of rigid piles against transversal forces. *Bulletin 12, Danish Geotech. Institute*, pages 1–9.

Hotta, N. and Ohta, T. (2000). Pore-water pressure of debris flows. *Physics and Chemistry of the Earth, Part B: Hydrology, Oceans and Atmosphere*, 25(4):381–385.

Iverson, R. M. (1997). The physics of debris flows. *Reviews of geophysics*, 35(3):245–296.

Iverson, R. M. (2012). Elementary theory of bed-sediment entrainment by debris flows and avalanches. *Journal of Geophysical Research: Earth Surface*, 117(F3).

Jeong, S. W., Leroueil, S., and Locat, J. (2009). Applicability of power law for describing the rheology of soils of different origins and characteristics. *Canadian Geotechnical Journal*, 46(9):1011–1023.

Johnson, C., Kokelaar, B., Iverson, R. M., Logan, M., LaHusen, R., and Gray, J. (2012). Grain-size segregation and levee formation in geophysical mass flows. *Journal of Geophysical Research: Earth Surface*, 117(F1).

Liu, R., Guo, S., and Yan, S. (2015). Study on the lateral soil resistance acting on the buried pipeline. *Journal of Coastal Research*, 73(sp1):391–398.

Locat, J. and Lee, H. J. (2002). Submarine landslides: advances and challenges. *Canadian Geotechnical Journal*, 39(1):193–212.

Maghsoudloo, A., Galavi, V., Hicks, M. A., and Askarinejad, A. (2017). Finite element simulation of static liquefaction of submerged sand slopes using a multilaminate model. In *19th International Conference on Soil Mechanics and Geotechnical Engineering*, volume 2, pages 801–804.

Niedoroda, A. W., Reed, C. W., Hatchett, L., Young, A., Lanier, D., Kasch, V., Jeanjean, P., Orange, D., Bryant, W., et al. (2003). Analysis of past and future debris flows and turbidity currents generated by slope failures along the sigsbee escarpment in the deep gulf of mexico. In *Offshore Technology Conference*. Offshore Technology Conference.

Oliveira, J. R., Almeida, M. S., Almeida, M. C., and Borges, R. G. (2009). Physical modeling of lateral clay-pipe interaction. *Journal of geotechnical and geoenvironmental engineering*, 136(7):950–956.

Ono, K., Yokota, Y., Sawada, Y., and Kawabata, T. (2017). Lateral force–displacement prediction for buried pipe under different effective stress condition. *International Journal of Geotechnical Engineering*, pages 1–9.

Ovesen, N. K. (1964). Anchor slabs, calculation methods and model tests. *Bulletin*, 16:39.

Parker, E. J., Traverso, C. M., Moore, R., Evans, T., Usher, N., et al. (2008). Evaluation of landslide impact on deepwater submarine pipelines. In *Offshore technology conference*. Offshore Technology Conference.

Paulin, M. J. (1998). *An investigation into pipelines subjected to lateral soil loading*. Doctoral dissertation, Memorial University of Newfoundland.

Pazwash, H. and Robertson, J. (1975). Forces on bodies in bingham fluids. *Journal of Hydraulic Research*, 13(1):35–55.

Puzrin, A. M., Germanovich, L., and Kim, S. (2004). Catastrophic failure of submerged slopes in normally consolidated sediments. *Géotechnique*, 54(10):631–643.

Randolph, M. and Gourvenec, S. (2011). *Offshore geotechnical engineering*. CRC Press.

Randolph, M. F., Gaudin, C., Gourvenec, S. M., White, D. J., Boylan, N., and Cassidy, M. J. (2011). Recent advances in offshore geotechnics for deep water oil and gas developments. *Ocean Engineering*, 38(7):818–834.

Randolph, M. F., Seo, D., and White, D. J. (2010). Parametric solutions for slide impact on pipelines. *Journal of geotechnical and geoenvironmental engineering*, 136(7):940–949.

Robert, D., Soga, K., O'Rourke, T., and Sakanoue, T. (2016). Lateral load-displacement behavior of pipelines in unsaturated sands. *Journal of Geotechnical and Geoenvironmental Engineering*, 142(11):04016060.

Roy, K. S. and Hawlader, B. (2012). Soil restraint against lateral and oblique motion of pipes buried in dense sand. In *International Pipeline Conference*, volume 45158, pages 7–12. American Society of Mechanical Engineers.

Sadrekarimi, A. (2019). Prediction of static liquefaction landslides. In *Civil and Environmental Engineering Presentations 4 in GEO ST.JOHN's 2019*.

Sahdi, F., Gaudin, C., White, D., Boylan, N., and Randolph, M. (2014). Centrifuge modelling of active slide-pipeline loading in soft clay. *Géotechnique*, 64(1):16–27.

Schapery, R. A. and Dunlap, W. A. (1978). Prediction of storm-induced sea bottom movement and platform forces.

Schofield, A. N. (1980). Cambridge geotechnical centrifuge operations. *Geotechnique*, 30(3):227–268.

Stanier, S. A., Blaber, J., Take, W. A., and White, D. (2015). Improved image-based deformation measurement for geotechnical applications. *Canadian Geotechnical Journal*, 53(5):727–739.

Summers, P. B. and Nyman, D. J. (1985). An approximate procedure for assessing the effects of mudslides on offshore pipelines. *Journal of Energy Resources Technology*, 107(4):426–432.

Take, W. A., Beddoe, R. A., Davoodi-Bilesavar, R., and Phillips, R. (2015). Effect of antecedent groundwater conditions on the triggering of static liquefaction landslides. *Landslides*, 12(3):469–479.

Taylor, R. (2014). *Geotechnical centrifuge technology*. Blackie Academic and Professional.

Teh, T., Palmer, A., Bolton, M., and Damgaard, J. (2006). Stability of submarine pipelines on liquefied seabeds. *Journal of waterway, port, coastal, and ocean engineering*, 132(4):244–251.

Thomas, D. G. (1965). Transport characteristics of suspension: Viii. a note on the viscosity of newtonian suspensions of uniform spherical particles. *Journal of Colloid Science*, 20(3):267–277.

Tian, Y. and Cassidy, M. J. (2011). Pipe-soil interaction model incorporating large lateral displacements in calcareous sand. *Journal of Geotechnical and Geoenvironmental Engineering*, 137(3):279–287.

Tiande, M., Chongwu, M., and Shengzhi, W. (1999). Evolution model of progressive failure of landslides. *Journal of Geotechnical and Geoenvironmental Engineering*, 125(10):827–831.

Tobita, T. and Iai, S. (2014). Combined failure mechanisms of geotechnical structures. In *Physical Modelling in Geotechnics*, volume 1, pages 99–112. CRC Press, Boca Raton, FL, USA.

Trautmann, C. H., O'Rourfce, T. D., and Kulhawy, F. H. (1985). Uplift force-displacement response of buried pipe. *Journal of Geotechnical Engineering*, 111(9):1061–1076.

White, D., Take, W., and Bolton, M. (2003). Soil deformation measurement using particle image velocimetry (piv) and photogrammetry. *Geotechnique*, 53(7):619–631.

White, D. J., Randolph, M. F., et al. (2007). Seabed characterisation and models for pipeline-soil interaction. In *The Seventeenth International Offshore and Polar Engineering Conference*. International Society of Offshore and Polar Engineers.

Woodson, R. (1991). A critical review of offshore pipeline failures. *prepared for the Marine Board, National Research Council*.

Ye, Y., Lai, X., Pan, G., Li, Q., Zhuang, Z., Liu, D., Chen, X., Wei, Y., Chen, J., Hu, T., Chen, X., Zhan, W., Li, Q., Tian, S., Li, D., and He, X. (2017). *Marine Geo-hazards in China*. Elsevier, Amsterdam.

Yin, M., Rui, Y., and Xue, Y. (2017). Centrifuge study on the runout distance of submarine debris flows. *Marine Georesources & Geotechnology*, pages 1–11.

Zakeri, A. (2009). Review of state-of-the-art: Drag forces on submarine pipelines and piles caused by landslide or debris flow impact. *Journal of offshore mechanics and Arctic engineering*, 131(1):014001.

Zakeri, A., Hawlader, B., and Chi, K. (2012). Drag forces caused by submarine glide block or out-runner block impact on suspended (free-span) pipelines. *Ocean Engineering*, 47:50–57.

Zakeri, A., Høeg, K., and Nadim, F. (2008). Submarine debris flow impact on pipelines—part i: Experimental investigation. *Coastal engineering*, 55(12):1209–1218.

Zhang, J., Stewart, D. P., and Randolph, M. F. (2002). Modeling of shallowly embedded offshore pipelines in calcareous sand. *Journal of geotechnical and geoenvironmental engineering*, 128(5):363–371.

Zhang, W. and Askarinejad, A. (2019a). Behaviour of buried pipes in unstable sandy slopes. *Landslides*, 16(2):283–293.

Zhang, W. and Askarinejad, A. (2019b). Centrifuge modelling of submarine landslides due to static liquefaction. *Landslides*, 16(10):1921–1938.

Zhu, H. and Randolph, M. F. (2011). Numerical analysis of a cylinder moving through rate-dependent undrained soil. *Ocean Engineering*, 38(7):943–953.

7

Conclusion

The more I learn, the more I realize how much I don't know.

Albert Einstein

The main goal of this doctoral research was to investigate soil-pipeline interaction mechanisms for pipelines buried in subaqueous slopes, which were triggered to fail by monotonic loads. Two situations of fully drained and (partially) undrained conditions, were considered. In total, one series of centrifuge tests was carried out under a fully drained condition and three series of centrifuge tests were performed under a (partially) undrained condition. These four series of tests and the corresponding results have been explained in Chapters 3 to 6, respectively.

Chapter 3 presented an investigation of the soil-pipeline interaction mechanisms for pipes buried in slopes which failed under drained conditions. The effects of the slope angle and the pipe burial position with respect to the slope crest on the ultimate induced pressure on the pipe were studied.

The goal of investigating soil-pipeline interaction mechanisms for pipelines buried in submarine slopes which failed under a (partially) undrained condition was achieved in three steps. Firstly, for simulating the monotonic-load induced liquefaction of subaqueous slopes in the geotechnical centrifuge, a test set-up was designed. The test set-up enabled the simulation of the controlled slope steepening process as presented in Chapter 4. Thereafter, for justifying the proper pore fluid viscosity, a detailed study on the triggering mechanism of monotonic-load induced liquefaction in saturated sandy layers was conducted, which is reported in Chapter 5. The scaling law of proper pore fluid viscosity was proposed based on the grain scale analysis which was supported by the centrifuge tests results. Lastly, the pipe behaviour under statically liquefied subaqueous slope failures using the newly developed test set-up is described in Chapter 6. The relationship between the ultimate induced pressure and factors such as the pipe burial depth, pipeline structural stiffness, slope angle and shear strain rate was studied. The main conclusions of the above-mentioned studies and some recommendations for further investigation are summarized in this chapter.

7.1. Conclusions

7.1.1. Simulation under drained condition (Chapter 3)

The first series of tests were conducted with the main focus on the effects of the slope angle and the pipe burial position with respect to the slope crest on the loads exerted on the pipe and on the slope failure mechanism. All the slopes were made of dry sand, thus it can be assumed that the slope failure mechanisms of these tests are analogous to that of soil movement under drained conditions. The slope instabilities were triggered by the monotonic loads applied to the slope crest. The loads acting on the pipes embedded at five different positions in the slopes were measured. Furthermore, the positions of slope failure mechanisms were obtained using the PIV technique.

It was found that the failure surfaces tended to pass below the pipe when the pipe was placed no more than $0.5D$ below the potential slip surface for 'greenfield' conditions. Results also showed that the pipes located within the potential failure zones of the slopes moved more than those buried outside the potential failure surfaces.

The effects of slope angle and the pipe distance to slope crest on the ultimate induced loads were found to be prominent. A new geotechnical method was proposed to estimate the ultimate load acting on the pipe when it is buried under sloping ground. Compared with the method proposed by Audibert and Nyman (1977), which includes factors of soil properties, pipe diameter and burial depth, the newly proposed geotechnical method further takes into account the effects of the slope angle and the pipe distance to the slope crest. Moreover, a hyperbolic relationship between the normalized force and pipe displacement was found.

7.1.2. Simulation of static liquefaction (undrained condition) –a) development of the test set-up (Chapter 4)

A new test set-up was designed as one of the prerequisites for studying the interaction between a buried pipe and a subaqueous static-load-induced landslide. This test set-up was integrated with a tilting mechanism for simulating the slope steepening process. During a test, the shear stresses could increase monotonically until the liquefaction is triggered. Moreover, a series of centrifuge tests with three different tilting rates were performed to evaluate the slope steepening rate effect on seabed stability.

It was concluded that the tilting technique was able to trigger static liquefaction in sandy slopes modelled in a geotechnical centrifuge. A slope liquefaction can occur in a very short time with no visible precursors before the failure. Slope liquefaction originated from the surface layer close to the slope toe and then developed towards to the slope crest and deeper locations within the slope. It was observed that a higher tiling/shearing rate would result in a faster accumulation of pore pressure and an earlier slope instability. The instability line was found to be dependent on the increasing rate of the slope angle or shearing rate.

After comparing the fluidization method with other methods traditionally used for making saturated sandy samples, such as moist tamping, drizzle and wet pluviation methods, the former was selected as the sample preparation method. A loose and saturated sandy sample might be sensitive to a minor anthropogenic disturbance. To avoid this, the fluidization system was integrated into the base of the testing strongbox. This design enabled the possibility of preparing samples right in the testing position without sample transportation and any other possible disturbance to the samples. Furthermore, this design provided three other advantages:

- Samples could represent the seabed/riverbed soil material in coastal areas in terms of soil structures, as the formation process of sand in the strongbox was similar to that in the field;
- Samples with similar properties could be prepared, as the same sand batch was used for all the tests and a fully saturated condition could be ensured. By conducting X-ray CT scan on a sample, it was found that the sample was uniform with similar relative densities along all three directions, i.e. height, width and length. The magnitude of the relative densities was about 31%.
- Sample preparation time could be reduced to 2 hours. This was significantly more efficient than what is required for other sample preparation methods.

For example, it took Askarinejad et al. (2018) about 8 hours to prepare a loose and saturated sandy sample with a volume of 5 x 10^{-3} m^3 by using the wet pluviation method.

7.1.3. Simulation of static liquefaction –b) investigation of scaling laws for pore fluid viscosity (Chapter 5)

A hypothesis for the triggering mechanism of monotonic-load induced liquefaction in saturated sandy layers was proposed. This was followed by the derivation of the scaling factor for fluid viscosity based on the grain scale analysis. It was determined that $\sqrt{N}$-fluid (a fluid that is $\sqrt{N}$-times more viscous water) should be used to simulate the onset of monotonic-load-induced liquefaction at *Ng*. This, however, differs from the standard practice of using *N*-fluid (a fluid that is *N*-times more viscous water) as the pore fluid for simulating dynamic events in the centrifuge. Therefore, a series of centrifuge tests simulating the sandy slope static liquefaction were designed to examine the proposed postulation on the scaling factor of pore fluid. These tests were conducted at various *g*-levels (i.e. 10*g*, 30*g* and 50*g*) with both *N*-fluid and $\sqrt{N}$-fluid as the pore fluid. The main conclusions are:

- Static liquefaction of a fully saturated loose sand layer could be triggered locally by fluid-grain interaction at the onset of the change of drainage regime from drained to (partially) undrained conditions. Hence, the derivation of scaling law for the triggering mechanism of static liquefaction should be based on the hydro-mechanical processes at the grain scale.

- The failure angles for $\sqrt{N}$-fluid tests at various g-levels were consistent which indicated similar onset of static liquefaction. According to the theory of "modelling of models", it was concluded that $\sqrt{N}$-fluid should be used as the pore fluid to simulate the onset of static liquefaction of underwater slopes triggered by monotonic loads.

- The excess pore pressure ratios for *N*-fluid tests at various g-levels were consistent, which were affected by the dynamic behaviour of slope failures. This observation was in consistence with the standard practice of using *N*-fluid for simulating dynamic events in the centrifuge.

7.1.4. Simulation of static liquefaction –c) behaviour of buried pipelines in statically-liquefied slopes (Chapter 6)

A set of centrifuge tests were carried out to study the behaviour of buried pipelines in statically-liquefied slopes utilizing the newly developed test set-up. A pipe system was designed with the functions of adjusting pipe embedded depth and pipeline structural stiffness, and monitoring the pipe external pressure/load and pipe displacement. A series of pictures during each test was captured and the PIV analysis was conducted to obtain the soil flow rate. The soil shear strain rate was defined as the ratio of the difference between the soil flow rate and the pipe moving rate to the pipe diameter. Moreover, the development of excess pore pressure was monitored

at seven locations with a sampling rate of 1 kHz. The influences of the pipe embedment ratio (pipe embedded depth/pipe diameter), pipeline structural stiffness, slope angle and shear strain rate on the ultimate pressures acting on the buried pipe during the slope liquefaction were investigated. In addition, the results were compared to the estimation of the geotechnical approaches proposed by Audibert and Nyman (1977), Calvetti et al. (2004) and the modified geotechnical approach proposed in Chapter 3 as well as the fluid dynamics approach proposed by Zakeri et al. (2008). The main conclusions are presented below:

- A duration of about 2 seconds (in prototype scale) of the accumulation of excess pore pressure was detected before the onset of slope liquefaction. This observation inferred that there is difficulty in applying the method of monitoring the change of excess pore pressure as an indicator for early warning systems in submerged loose sandy slopes.
- The magnitudes of the excess pore pressure ratios showed that static liquefaction could happen with an excess pore pressure ratio lower than 1. The excess pore pressure ratios measured at seven locations were generally smaller than 1 with an exception of the one which was nearest to the slope toe. However, the pore pressure measurement at this location was strongly influenced by the dynamic behaviour of flow slides. The smallest excess pore pressure ratio was 0.4 and was measured at a position close to the slope crest.
- No clear relationship was found between the ultimate induced pressure and the pipe embedment ratio which is one of the main factors in all the geotechnical approaches.
- The fluid dynamic approach tended to underestimate the ultimate induced pressure. However, it should be noted that the measured shear strain rates were less than 0.1 sec^{-1}.
- It was found that the ultimate induced pressure was related to the soil shear strain rate with a power law relationship (see Equation 6.21). The pipeline structural stiffness and slope angle affected the ultimate induced pressure as well. A higher value of pipeline structural stiffness or slope angle would lead to a higher soil shear strain rate, and hence a larger magnitude of the ultimate induced pressure.
- The soil moving velocity distribution along soil depth of a liquefied seabed without a buried structure was found to be similar to that of a laminar debris flow and can be described by Equation 6.18 .

7.2. Recommendations for future work

The results of the drained slope failure tests have revealed the effects of pipe position and slope angle on the slope failure mechanism. In this study, the pipe embedment ratio was less than or equal to 4.1 and the slope angle was determined to be constant with a value of 18.7°. Further centrifuge tests on the pipe behaviour

in drained slope failure with various pipe locations, slope angles and soil materials are suggested to validate the proposed method (Equation 3.10). Numerical simulation on this topic is also suggested.

The results of the centrifuge tests with the slope steepening mechanism has indicated that the ultimate pressure acting on a buried pipe was a function of the soil shear strain rate. Accordingly, further fundamental studies regarding the influence of the soil shear strain rate on the induced pipeline external pressure are necessary. Moreover, further study on the dependency of soil-fluid properties on the shear strain rate and the flow rate is recommended in order to understand the pipe-soil behaviour during marine slope liquefaction from the initial stage to post-liquefaction stage. In this study, the soil-pipeline interaction during the initiation of slope liquefaction has been investigated. A further step can be to investigate the soil-pipeline interaction during the development of a subaqueous landslide. A new design of a testing system with sufficient space for the landslide run-out might be needed. Numerical modelling of the subaqueous slope liquefaction and pipeline-liquefied soil interaction are recommended, as both methods are suitable for simulating large deformation cases.

As presented in Chapter 4, the design of the fluidization system has been proven to be a useful method to prepare loose, saturated, uniform and disturbance sensitive sandy samples, and the tilting system has shown the advantage of making subaqueous sandy slopes. Both testing methods have the potential to be used for other offshore geotechnical studies based on centrifuge modelling such as the examples below:

- To investigate the non-K_0 loading history effects on the subaqueous slope stability. This can be done by tilting the sample to a certain slope angle at the normal gravity condition, then run the centrifuge to the target centrifugal acceleration level.
- To study the cyclic performance and bearing capacity of suction caisson foundations/anchors in sandy (either flat or inclined) seabed. However, this goal requires the design of a suction caisson/anchor loading system which can be used in combination with the fluidization system.
- To evaluate the wave loading effects on the inclined sandy seabed stability. With the aid of the existing test set-up, subaqueous sandy slopes with various inclinations can be simulated. If a wave generator and a corresponding wave energy absorber can be designed and installed on the top of the strongbox at the fluid table level, the wave loading effects on the subaqueous slope stability can be investigated.

References

Askarinejad, A., Zhang, W., de Boorder, M., and van der Zon, J. (2018). *Centrifuge and numerical modelling of static liquefaction of fine sandy slopes*, volume 2, pages 1119–1124. CRC Press.

Audibert, J. M. and Nyman, K. J. (1977). Soil restraint against horizontal motion of pipes. *Journal of the Geotechnical Engineering Division*, 103(10):1119–1142.

Calvetti, F., Di Prisco, C., and Nova, R. (2004). Experimental and numerical analysis of soil–pipe interaction. *Journal of geotechnical and geoenvironmental engineering*, 130(12):1292–1299.

Zakeri, A., Høeg, K., and Nadim, F. (2008). Submarine debris flow impact on pipelines—part i: Experimental investigation. *Coastal engineering*, 55(12):1209–1218.

Acknowledgements

During a period of around four years (Oct. 2015 - Nov. 2019) as a PhD researcher at the Department of Civil Engineering and Geoscience in TU Delft, I tried to make some contributions in the field of centrifuge modelling on marine landslide-pipeline interaction. I hope my research work has provided some improved insights in this area. During this unforgettable journey, it is my great honour to have so many families, friends, colleagues and not the least, supervisors to help and guide me. Without their support, it would have been impossible for me to finish this journey. I have gained not only precious research experience but also invaluable friendship which I will carry with for a lifetime. I want to apologize for not being able to list all the names of friends I am grateful for. This doctoral dissertation is dedicated to them. And the following is not necessarily in the sequence of significance.

I would like to thank my promotor, Prof. Cristina Jommi, for the patient guidance, support and freedom she has provided throughout this wonderful journey. I really appreciate the valuable inspiration and deep insight she gave me during the meetings. Her rigorous attitude towards research impresses me a lot.

I must express my gratitude to my daily supervisor, Dr. Amin Askarinejad, who has not only inspired me when I felt lost by asking insightful questions and offering invaluable advice but also encouraged me during the tough times. I have been extremely lucky to have a daily supervisor who is also a sincere friend. I still miss the joyful vacation and laughers we shared together. It's my great honour to continue our cooperation in research as a postdoc researcher, hope that I deserve the opportunity given.

I would like to acknowledge all my committee members who devoted priceless time and effort to reviewing my thesis and giving precious comments, which helps me improve the quality of my PhD research and thesis.

I would like to thank all my Ph.D colleagues and staff members of the Geo-Engineering section and colleagues from other sections, in particular: Anne-Catherine, Arash, Dirk, Divya, Haoyuan, Hongfen, Leon, Kang, Michael, Shuhong, Stefano, Weihai, Yajun, Yutian, Xiangcou, Xuehui and Yuen. Their sincerity and humour make me feel warm. I am grateful to spend this time with them. Thanks to Haoyuan for being my "Kappa" during the whole Ph.D period.

Special thank-yous to Han de Visser, Kees van Beek and Ronald van Leeuwen. Without their wise counsel and support on centrifuge testing, the experimental work would not have been possible. Many thanks to Leon Roessen, Bert Bakker, P.M. Meijvogel-de Koning, Tom Philips and Jens van den Berg, Marc Friebel, Karel Heller and Armand Middeldorp for their technical input to this study.

Sincere thanks to Dr. Sam Stanier from Cambridge University and Dr. Xiaohui Cheng from Tsinghua University for their wise advice for the results analysis in Chapter 6.

In addition to the above, I also feel grateful for my brothers and sisters from Chinese Christelijke Gemeente in Netherlands (CCGN) and International Christian Fellowship Delft (ICF). You guys have made me feel Delft my second home-town. And all your love and prayer gave me such a comfort, which helps me to grow firmly in faith.

Likewise, I owe thanks to my friends and former colleagues who encouraged me to conduct the doctoral research abroad, in particular, Zhao Lu, Tao Xu, Hong Zheng, Deliang Liu and Jiahong Chen. Your encouragement ensured that my PhD journey has a good start.

Last but not least, the unconditional love from my parents, grandma and uncle Ping Zhang has encouraged me to move forward. I feel so happy to be born and live in such a warm family. My deep and sincere thanks go to my lovely wife, Chengcheng, for her endless patience and devotion throughout the last eight years.

A short acknowledgement cannot hold the names of so many lovely people, nor can it carry my full gratitude. Thank you for walking with me on this journey. I am grateful that this journey has allowed my life to undergo construction and renewal! Hope that in the future I can listen to my inner voice in the hustle and bustle of the world, sticking to my belief. May what I say and do is worthy of the trust of the society.

Curriculum Vitæ

Weiyuan ZHANG (张巍元)

1989.9.10	Born in Jilin, China.

Education

2007.8–2011.6	BSc in Civil Engineering PLA University of Science and Technology Nanjing, China
2011.8–2014.1	MSc in Geotechnical Engineering Harbin Institute of Technology Shenzhen, China *Thesis:* 3D modeling of low-dilution drawing in sublevel caving *Supervisor:* Assoc. Prof. dr. W. D. Lei
2015.10–2019.11	PhD in Geotechnical Engineering Geo-Engineering Section Department of Geoscience and Engineering Faculty of Civil Engineering and Geoscience Delft University of Technology Delft, the Netherlands *Thesis:* Centrifuge modelling of the behaviour of buried pipelines subjected to submarine landslides *Promotor:* Prof. dr. ir. C. (Cristina) Jommi *Copromotor:* Dr. A.(Amin) Askarinejad

Professional Experience

2014.2–2015.9
Geotechnical engineer
Shenzhen Investigation & Research Institute CO., LTD
Shenzhen, China

2019.12–now
Geotechnical engineer
SPT Offshore B.V.
Woerden, the Netherlands

2020.9–now
PostDoc researcher
Geo-Engineering Section
Department of Geoscience and Engineering
Faculty of Civil Engineering and Geoscience
Delft University of Technology
Delft, the Netherlands
Project: Blue Piling
Supervisor: Dr. A.(Amin) Askarinejad

Awards

2013
Team championship of the First University Boat Race
Shenzhen University Town
Shenzhen, China

2018
Best Paper Award
Departments of Geoscience & Engineering and
Geoscience & Remote Sensing
Delft University of Technology
Delft, the Netherlands

List of Publications

Journal publications

5. **Zhang W.**, Askarinejad A. (2020) *Centrifuge modelling of static liquefaction in submarine slopes: the scaling law dilemma*. Canadian Geotechnical Journal (Accepted).

4. **Zhang W.**, Askarinejad A. (2019) *Centrifuge modelling of submarine landslides due to static liquefaction*. Landslides, **16(10)**, 1921-1938.

3. Arnold A., Krähenbühl M., **Zhang W.**, Askarinejad A. (2019) *Bearing capacity under increasing undrained shear strength*. International Journal of Physical Modelling in Geotechnics, 1-13.

2. **Zhang W.**, Askarinejad A. (2018) *Behaviour of buried pipes in unstable sandy slopes*. Landslides, **15(11)**, 1-11.

1. **Zhang W.**, Askarinejad A. *Ultimate lateral pressures exerted on buried pipelines by the initiation of submarine landslides*. Landslides (Positive feedback).

Conference publications

5. **Zhang W.**, Askarinejad A. (2019) *A novel technique for simulating submarine landslides in geo-centrifuge*. Proceedings of the 17th European Conference on Soil Mechanics and Geotechnical Engineering (XVII ECSMGE), Reykjavik.

4. **Zhang W.**, Askarinejad A. (2019) *Physical modelling of static liquefaction of seabed due to scouring*. Proceedings of the 17th European Conference on Soil Mechanics and Geotechnical Engineering (XVII ECSMGE), Reykjavik.

3. Askarinejad A., **Zhang W**., de Boorder M. and van der Zon J. (2018) *Centrifuge and numerical modelling of static liquefaction of fine sandy slopes*. In Physical Modelling in Geotechnics, Volume 2: Proceedings of the 9th International Conference on Physical Modelling in Geotechnics (ICPMG 2018), London, United Kingdom (pp. 1119-1124). CRC Press.

2. **Zhang W.**, Gng Z. and Askarinejad A. (2018) *An experimental and numerical study of pipe behaviour in triggered sandy slope failures*. In Physical Modelling in Geotechnics, Volume 2: Proceedings of the 9th International Conference on Physical Modelling in Geotechnics (ICPMG 2018), London, United Kingdom (pp. 1149-1154). CRC Press.

1. Arnold A., **Zhang W**. and Askarinejad A. (2018) *Undrained shear strength profile of normally and overconsolidated kaolin clay*. In Physical Modelling in Geotechnics, Volume 1: Proceedings of the 9th International Conference on Physical Modelling in Geotechnics (ICPMG 2018), London, United Kingdom (pp. 119-124). CRC Press.